2014

Electrical and optical properties of the bulk states in HgTe/CdTe quantum wells topological insulator

Qinjun Chen
University of Wollongong

UNIVERSITY OF WOLLONGONG

School of Physics

Electrical and optical properties of the bulk states in HgTe/CdTe quantum wells topological insulator

Qinjun Chen

Supervisors: **Prof. Chao Zhang**

Prof. Roger A. Lewis

Prof. Xiaolin Wang

This thesis is presented as part of the requirement for the

Award of the Degree of

Doctor of Philosophy

of the

University of Wollongong

December 2014

Declaration

I, Qinjun Chen, declare that this thesis, submitted in fulfilment of the requirements for the award of Doctor of Philosophy, of the School of Physics, University of Wollongong, is wholly my own work unless otherwise referenced or acknowledged. The document has not been submitted for qualifications at any other academic institution.

Qinjun Chen, December 1, 2014

ABSTRACT

HgTe/CdTe quantum wells (QWs) are the first known topological insulator material, which requires strong intrinsic spin orbit coupling (SOC). In HgTe/CdTe QW, a phase transition happens when the thickness of the HgTe "well" exceeds the critical value (6.3 nm), which results in band inversion. The band inverted HgTe/CdTe QWs form topological edge states that support currents with opposite spins transporting in opposite directions, while the bulk state remains insulating. On the edge, the gap closed with linear energy dispersion at the low energy regime, creating a pair of Dirac cones. Such edge states have attracted great attention and have been extensively studied. However, the bulk insulating state should not be forgotten, especially, when the Fermi energy is out of the bulk gap.

We first study the dielectric function of *n*-type HgTe/CdTe QWs. We present the dielectric response contributed from intraband and interband excitations, respectively. The thermal effects have significant effect on the intraband contributed polarization function, of which the peaks shift toward high frequency with increasing temperature. The plasmons in the two-dimensional (2D) electron gas (2DEG) in the HgTe "well" decays rapidly.

We then investigated the energy loss rate (ELR) of a charged particle in an *n*-type HgTe/CdTe QW. It is found that the ELR characteristics due to the intraband excitation have linear energy dependence while those due to interband excitation depends on the energy exponentially. An interesting quantitative result is that for a large range of the incident energy, the mean inelastic scattering rate is around a few terahertzs.

We also studied the frequency-dependent current response of the bulk state of topological insulator HgTe/CdTe QW. Our formalism is based on the quantum transport equation, considering the second order electron-impurity scattering under a weak external field. The optical conductivity is attributed to the intra-band process under a weak excitation. We found out that the conductivity decreases with temperature at low temperature and increases with temperature at high temperature. The transport scattering rate has an opposite frequency dependence in the low temperature regime and in the high temperature regime. The different frequency dependence is due to the interplay of (i) impurity scattering probability of a single electron decreases frequency at any temperature and (ii) number of electrons satisfying scattering condition at high temperature increases with the frequency.

We reveal that the *n*-type HgTe/CdTe quantum well have a strong nonlinear optical property in the three-photon mixing. While the gapless surface state in TI can exhibit strong nonlinear effect due to the linear energy dispersion, the nonparabolic energy dispersion of the bulk state is responsible for the photo mixing effect reported here. To produce response at terahertz frequency regime from femtosecond electrical field, the mixing efficiency is around 10^{-4} comparable to that of nonlinear semiconductor crystals. The optimal temperature for this nonlinear effect is around 50-100K. The results suggest a potential application of TI in terahertz photonics.

We present strong nonlinear optical responses in terahertz regime in the bulk state of an *n*-type HgTe/CdTe QW. The third-order nonlinear optical conductance can be observed under a moderate electric field. There are sign changes of third order conductance happen in the low chemical potential μ for two types of band structures at low energy regime. The thermal influences on nonlinear optical

responses of HgTe/CdTe QWs are also studied, especially when μ lies between 6 meV and 10 meV. The sign changes are observed when temperature increases up to 300 K. These results suggest that HgTe/CdTe QWs are promising candidates for nonlinear photonics and optoelectronics devices applications.

We finally investigated the nonlinear response of 2D surface states of a 3D strong topological insulator (e.g. Bi_2Se_3). We report that for such surface states on Bi_2Se_3, there exist strong nonlinear optical responses in terahertz regime. The third-order nonlinear optical conductance can be observed under a moderate electric field. The thermal influence on nonlinear optical responses of the surface states of Bi_2Se_3 are also studied in different temperature and frequency ranges. The results suggest that the 3D TIs such as Bi_2Se_3 are promising candidates for nonlinear photonics and optoelectronics devices.

ACKNOWLEDGEMENTS

How time flies! When I finished the last word of my doctoral thesis, many individuals came to mind. They are the people who, in the past three and a half years, have constantly supported me in completing my PhD study and research.

First of all, I would like to express my deepest appreciation to my thesis supervisor Prof. Chao Zhang for his patient guidance and enthusiastic inspiration. His immense knowledge and profound comments have always inspired me in doing my research program. Starting from zero, Prof. Chao Zhang guarded me all the way from my thesis proposal up to the thesis manuscript. It would not have been possible to complete my thesis without his constant help and unfailing advice.

I sincerely thank my co-supervisors Prof. Roger A. Lewis and Prof. Xiaolin Wang, both of whom have always been friendly and willingly to share their viewpoints with on cutting-edge topics and to encourage me in maintaining the progress in my research. I am outstandingly lucky to join their group, in which I have had the chances to learn many interesting experimental ideas and results, especially, at every Friday group meeting with Prof. Roger.

I am deeply in debt to Assoc/Prof. Jianmin Ma from Hunan University for his generosity in sharing his interesting research results. I must also acknowledge Dr. Dongqi Shi for training me on the PLD equipment. I thank Prof. Shixue Dou, Prof. Huakun Liu, Assoc/Prof. Josip Horvat, Dr. Enbang Li and Duncan Fisher for their support throughout my PhD years. I really appreciate Dr. Tania Silver for taking time out of her busy schedule to correct my thesis. I would like to thank all my fellow group members: Zengji Yue, Evan Constable, Julian Steele, Krunal Radhanpura Lucia Malebogo Lepodise, Yee Sin Ang and Matthew Sandson for

many inspiring discussions and willingness to repeat their explanations on their research topics untill I understand.

I thank Dr. Zidong Zhang, Yuanlong Fan, Dr. Chengbo Zhu, Frank Yun, Dr. Jiantie Xu and Feng Xiao and all my best friends for all the happy hours in my PhD life.

Last and most important, I would like to thank my parents, my grandparents, and my sisters and brothers. It would have been impossible for me to even start a PhD career without their selfless support, both spiritually and materially.

Publication list

Journal papers:

1. **Qinjun Chen**, Yee Sin Ang, Roger A. Lewis, Xiaolin Wang and Chao Zhang, Photonmixing in topological insulator HgTe/CdTe quantum wells in terahertz regime, Applied Physics Letters **101**, 211109 (2012). (**Chapter 5**)
2. **Qinjun Chen**, Yee Sin Ang, Roger A. Lewis, Xiaolin Wang and Chao Zhang, Energy loss rate of a charged particle in HgTe/(HgTe,CdTe) quantum wells, Applied Physics Letters **103**, 192107 (2013). (**Chapters 2 & 3**).
3. **Qinjun Chen**, Matthew Sanderson, J. C. Cao and Chao Zhang, Dynamic conductivity of *n*-type HgTe/CdTe quantum well topological insulator. Applied Physics Letters **105**, 202110 (2014). (**Chapters 2 & 4**).
4. Yee Sin Ang, **Qinjun Chen** and Chao Zhang, Nonlinear optical response of graphene in terahertz and near-infrared frequency regime, Front. Optoelectron. (2014). (**Chapter 7**).
5. Zidong Zhang, Runhua Fan, Min Chen, Yi Du, Xiaolin Wang, **Qinjun Chen**, Lucia Lepodise, Lei Qian, Feng Dang, Shibing Pan and Mingxun Yu, Large-area, low-cost infrared metamaterials' fabrication via metallic mesh-involved pulsed laser deposition. (Under review).
6. **Qinjun Chen**, Matthew Sandson and Chao Zhang, Nonlinear optical response of HgTe/CdTe quantum well in the terahertz regime. (Under preparation). (**Chapter 6**).

Conference papers:

1. **Qinjun Chen**, Roger A. Lewis, Xiaolin Wang and Chao Zhang, Nonlinear response of topological insulators in the terahertz regime, 37th International Conference on Infrared, Millimeter and Terahertz Waves (IRMMW-THz 2012), Wollongong, 23-28 September 2012 .
2. **Qinjun Chen**, Dongqi Shi, Xiaolin Wang, Roger A. Lewis and Chao Zhang, Dielectric properties of Bi doped Sb_2Te_3 thin films studied by terahertz time-domain spectroscopy, 38th International Conference on Infrared, Millimeter and Terahertz Waves (IRMMW-THz 2013), Mainz, 1-6 September 2013.

CONTENTS

LIST OF FIGURES

LIST OF TABLES

LIST OF SYMBOLS AND NOTATIONS

e: electron charge, 1.602×10^{-19} C.

eV: electron volt, 1.602×10^{-19} J.

$\hbar$: The deduced Planck's constant, $\hbar = \frac{h}{2\pi} = 6.583 \times 10^{-16}$ eV · s.

k_B: Boltzmann's constant, 8.614×10^{-5} eV/K.

κ_0: The dielectric constant of vacuum, 8.85×10^{-12} F/m. (Chapter 2-4).

κ_s: The static dielectric constant of material. (Chapter 2-4).

k, **p**, **q**: momentum vector in band structure, particle momentum vector and momentum transfer vector, respectively.

k, p, q: The corresponded scalar value of **k**, **p**, **q**.

$a^{\dagger}_{\mathbf{k},s}, a_{\mathbf{k},s}$: The creation and annihilation operators, respectively. (Chapter 1-7)

$E_{\mathbf{p}}$: The energy of a particle with momentum$\hbar\mathbf{p}$. (Chapter 3)

$\varepsilon_s(\mathbf{k})$: The energy of an electron at state **k**. (Chapter 1-7)

A, B, C, D, M: The material parameters of HgTe/CdTe quantums. (Chapter 2-7).

$R_{\mathbf{k},s}$: A notation of $R_{\mathbf{k},s} = \frac{A^2 - 2BM + 2B^2k^2}{s\sqrt{(M - Bk^2)^2 + A^2k^2}}$. (Chapter 4, 5).

$C_s(\mathbf{k})$: A notation of $C_s(\mathbf{k}) = \varepsilon_s(\mathbf{k}) - M + B_+k^2$. (Chapter 2, 4).

$F^{ss'}(\mathbf{k}+\mathbf{q}, \mathbf{k})$: The overlap factor of two band states **k**+**q** and **k**. (Chapter 2-4).

$F_{\alpha'\alpha}(\mathbf{k}+\mathbf{q}, \mathbf{k}, t)$: Density matrix element. (Chapter 4).

$\mathbf{A}_e, \mathbf{A}(\mathbf{r}, t)$: The vector potential. (Chapter 1-7).

$V, V(\mathbf{r}, t)$: The scalar potential.

E, **E**(**r**,t): the electric field.

V_q: The Fourier transform of the coulomb potential. $V_q = \frac{e^2}{2\kappa_0 k_s |\mathbf{q}|}$ in two dimensional.

$\rho(\mathbf{r}, t)$: The charge density.

$n(\mathbf{r}, t)$: The particle or carrier density.

$U(\mathbf{r}, t)$: The potential energy.

κ_r or $\kappa(q, \omega)$: The dielectric constant as a function of q and ω. (Chapter 2-4).

$\Pi(q, \omega)$: The polarization function. (Chapter 2-3).

The notations or symbols above will be used throughout the whole thesis unless specified.

INTRODUCTION

Topological insulator (TI) is a new state of material that in the bulk is an insulator with large band gap, but the edge (of two-dimensional, 2D TI) or surface (of three-dimensional, 3D TI) forms gapless metallic states.[1, 2] These gapless surface states are benefit from the strong intrinsic spin-orbit coupling (SOC) of the material, and are topologically protected by time-reversal symmetry (TRS). In the presence of TRS, the Kramers theorem requires that these gapless states are at least doubly degeneracy, which constructs a pair of Dirac cones.[2] There are also a new set of topological invariants, Z_2 topological invariants, counting the number of these "cones" on the edge or surface.[3-6] Z_2 topological invariants are developed to characterize the topological non-trivial surface states. Simply put, the surface of a TI contains odd number pairs of Dirac cones.[7, 8] Moreover, electrons on the TI surface are spin-momentum locking, which means the electrons with opposite spins transport in the two opposite directions.[9, 10] As a result, the spin currents are observable on the surface, and due to the TRS, these spin currents are robust against any non-magnetic impurities. However, the net charge transport is zero, since two charge currents in opposite direction cancel each other. So far, TI materials have become a hot topic in condense matter physics and material engineering.[2, 11, 12] The topological edge or surface states exhibit many peculiar properties such as: quantum spin Hall effect (in 2D TIs),[9, 10, 13, 14] disspationless transport,[9, 15] inverse spin Hall effect,[16] giant magneto-optical effect,[17] room temperature giant magnetoresistance,[18] ambipolar electric field effect,[19] observation of Dirac plasmon,[20] Josephson super current,[21] Majorana Fermion,[22] helical Dirac fermions,[23, 24] etc. Therefore, TIs have potential

application in quantum computing, optoelectics, magnetoelectrics, spintronics, and so on.

HgTe/CdTe quantum wells (QWs) are confirmed 2D TI materials, on which the quantum spin Hall effect has been observed when the thickness of the HgTe layer is larger than the critical value of d_c = 6.3 nm. It has long been known that HgTe has an inverted band structure with a negative gap of -1.3 eV due to the strong SOC, and CdTe has a positive gap of 1.6 eV. In the thin HgTe/CdTe QWs, the states in the HgTe "well" has a "normal" band structure, where E1 acts as the lowest conduction band and H1 constructs the highest valence band, owing to the confinement of the CdTe barrier layers. As the thickness of the HgTe layer increases, the SOC is getting significance and finally dominates the confinement effects, and the band inversion between E1 and H1 occurs. Therefore, there is a phase transition in the critical well thickness (d_c = 6.3 nm), where the QWs change from a semiconductor into a semimetal. Keep increasing the well thickness, a gap will be open again in the bulk HgTe/CdTe QWs, but on the edge, the gapless states are reserved thinks to the protection of TRS, giving rise to TIs.

Our interest will be focusing on 2D HgTe/CdTe QW TIs, on which the edge state is 1D. It has been reported that the carrier density of a HgTe/CdTe QW can be reduced to the magnitude of ~10^{11} cm^{-2} in a highly pure sample[13, 14]. Even in such a low carrier density system, we noticed that in the case of d = 7.0 nm, where d is the thickness of the well layer, the Fermi energy, E_F = 0.012 eV, still lies in the conduction band. The edge response could be overwhelmed by the bulk state in the electron transport measurements, as it is estimated that only approximately one in 10^8 electrons resides near the edge rather than the bulk[25]. Thus, it is of equal

importance to investigate the transport properties of the bulk in order to interpret the HgTe/CdTe QW TI overall. In addition, HgTe/CdTe QWs are also found to be interesting in the studies such as large Rashba spin-obit splitting,[26] quantum Andreev effect[27], weak anti-localization effect[28], infrared to far infrared optoelectrics,[29, 30] and so on.

In my thesis, the contents will be organized as follow. Chapter 1 presents the literature review. In Chapter 2, we study the fundamental dielectric properties of HgTe/GdTe QWs; in Chapters 3 and 4, we investigate the dynamic conductivity considering the impurity scattering and the energy loss rate of a charged particle in HgTe/GdTe QWs, respectively, including the screening effects. Chapter 5 sets up a model for four-wave mixing in THz generation based on HgTe/GdTe QWs. In Chapters 6 and 7, we calculate the nonlinear effects of HgTe/GdTe QWs and the 2D surface of Bi_2Se_3, respectively.

CHAPTER 1 LITERATURE REVIEW

1.1 Historical review on topological insulators (TIs)

Topological insulators (TIs) were discovered in the course of exploring the quantum spin Hall effect (QSHE).[1, 2, 12]

In 1879, Edwin Hall[31] discovered in an experiment that a voltage difference was generated transverse to the electric current (say, in the *x*-*y* plane) when a magnetic field was applied perpendicular to the sample (in the *z* direction). This voltage difference is the Hall voltage, name after Edwin Hall, and the effect is called the Hall effect. About a century later, in 1980, Klaus von Klitzing et al.[32] set up a transport experiment at low temperature with a strong magnetic field. They observed two significant phenomena: there was electric current transport along the edge of the sample, and the Hall conductance was quantized taking only integer numbers of the unit value e^2/h, which was independent of material details.[33, 34] This effect is known as the quantum Hall (QH) effect or integer quantum Hall (IQH) effect. Before long, Laughlin[35], Stormer and Tsui[36] discovered the fractional quantum Hall effect using particular magnetic fields and extremely low temperatures in low carrier density semiconductors. It is notable that magnetic field plays an important role in these Hall effects.

The theoretical study of the spin-Hall effect (SHE) dates back to 1974 to work conducted by the Russian physicists Dyakonov and Perel,[37] who considered the extrinsic effect arising from interaction of the spin-orbit coupling (SOC) with impurities, although such an extrinsic SHE was later proved to be less important, as it might be cancelled by the vertex correction.[38, 39] Thus, more attention is being paid to the intrinsic SHE which is fundamentally derived from the SOC of the host band

structure.[40] In 2003, Murakami et al.[41] claimed that the dissipationless quantum spin current could be induced by an electric field at room temperature in doped semiconductors such as Si, Ge, and GaAs. Later on, they predicted[42] a type of "spin-Hall insulator (SHI)", in which this SHE could appear even without any magnetic field, although the authors also pointed out in the prediction that the spin-Hall conductance in such a SHI is not quantized.[42] The first experimental observation of the SHE was reported independently by Kato et al[43] and by Wunderlich et al.[44] in 2004. Kato et al.[43] used a Kerr rotation microscopy system to study GaAs and strained InGaAs in the absence of any magnetic field. Two opposite spin currents transported along the edge of the sample were fitted well with the theoretical predictions. For the strained sample, they ascribed the SHE to be extrinsic. Wunderlich et al.[44] considered a 2D hole system with strong SOC that splits heavy-hole states in the plane of the 2D layer. The two opposite spin signals were detected for the two edges. The authors suggested that the SHE observed should be intrinsic, which was in good agreement with other theoretical proposals.[40, 42, 45]

Many efforts were made to establish models for the quantum spin-Hall effect (QSHE), in which the spin degeneracy is necessarily lifted intrinsically.[9, 10, 46, 47] In 2005, one profound model was proposed by Kane and Mele[6, 9]. They introduced an SOC term to create gaps with opposite spin around the K′ and K point in graphene and showed how gapless states survive at the edge with respect to the time reversal symmetry (TRS) at the low temperature limit.[6, 9] The SOC effect in graphene, however, is so weak that it opens a gap merely on the order of 10^{-3} meV.[48-50] In 2006, Bernevig, Hughes and Zhang predicted[10] that mercury telluride–cadmium telluride (HgTe/CdTe) QWs have potential for observation of the quantum spin Hall effect

(QSHE), as a HgTe/GdTe QW could experience a phase transition by tuning the thickness of the HgTe layer. This idea was experimentally confirmed by Krönig et al.,[13] and the quantized Hall conductance was $2e^2/h$, convincingly matching the prediction.

Meanwhile, an important theoretical breakthrough for 3D TIs was made by three independent groups[3, 4, 51, 52], in which they developed a new set of topological invariants to distinct trivial and non-trivial insulators. A category of weak 3D TIs, such as bismuth, can be viewed as a stack of 2D TI layers, so that the overall effect of one–dimensional (1D) edges leads to a 2D topological surface.[2, 3] Such 2D surface states are easily destroyed by impurities, however.[2] On the other hand, there is a category of strong 3D TIs, which are based on the heavy element solid compounds that feautre strong SOC. In the theoretical prediction, they could be Bi_2Te_3, Bi_2Sb_3, Bi_2Se_3, Sb_2Te_3, α-Sn, strained HgTe, etc.[51, 53] The first 3D TI was experimentally identified on $Bi_{0.9}Sb_{0.1}$ using angle-resolved photoemission spectroscopy (ARPES) performed by Hasan's group at Princeton University[54]. Subsequent research efforts, both experimental and theoretical, have been carried out by many groups by using ARPES, scanning tunnelling microscopy or spectroscopy (STM or STS), and other techniques.[7, 19, 20, 23-25, 55-68]

1.2 Theory on topological nature

The core properties of the TIs can be summarized as strong intrinsic SOC,[10, 53, 54] Z_2 topological invariants,[3-6, 51, 52, 69] and dissipationless transport protected by time-reversal symmetry (TRS).[10, 41, 70]

1.2.1 Strong SOC in TIs

Generally, in a bulk insulator, electrons are confined to the atoms. When the boundary is taken into account, however, electrons at the boundary can be non-localized under certain circumstances, such as on applying a magnetic field or imposing a pressure, leading to the flow of charge currents on the surface. Analogously, the topological surface states of TI materials account for their strong intrinsic SOC.

Kane-Mele (KM) model[6, 9] (in graphene)

Graphene is the simplest 2D system ever discovered. The band structures at six corners in the first Brillouin zone (FBZ) are described by the Dirac equation and displayed as gapless, linear dispersion, and pseudo-spin texture.[71] In the KM model, SOC is necessarily introduced to open up a gap in the bulk of graphene, yet the QSHE could be realized along the sample edges, which remain gapless under the protection of time reversal symmetry or Z_2 topological invariants. The SOC in graphene brings about a term that is theoretically equal to the Haldane model, which shows a periodic magnetic field with no net flux, but does not break TRS. This SOC generates gaps with opposite signs for opposite spins at the two inequivalent Dirac points in the FBZ, and an electric field subsequently induces two opposite currents for the two opposite spins. These two currents are transported along the gapless state only, which is explained by Laughlin's argument. This phenomenon is fundamentally different from other SHI and zero-gap SHE phenomena.

Neverthleless, the KM model is based on the assumption "sufficiently low energy", and unfortunately, the SOC in graphene is very weak, of the order of 4 meV,

corresponding to a gap on the order of 10^{-3} meV.[48-50] Experimentally, this is extremely small for realizing the topological phase order. Even so, this model has paved the way for the development of the QSHE, or 2D TIs, and materials with strong SOC should be considered.

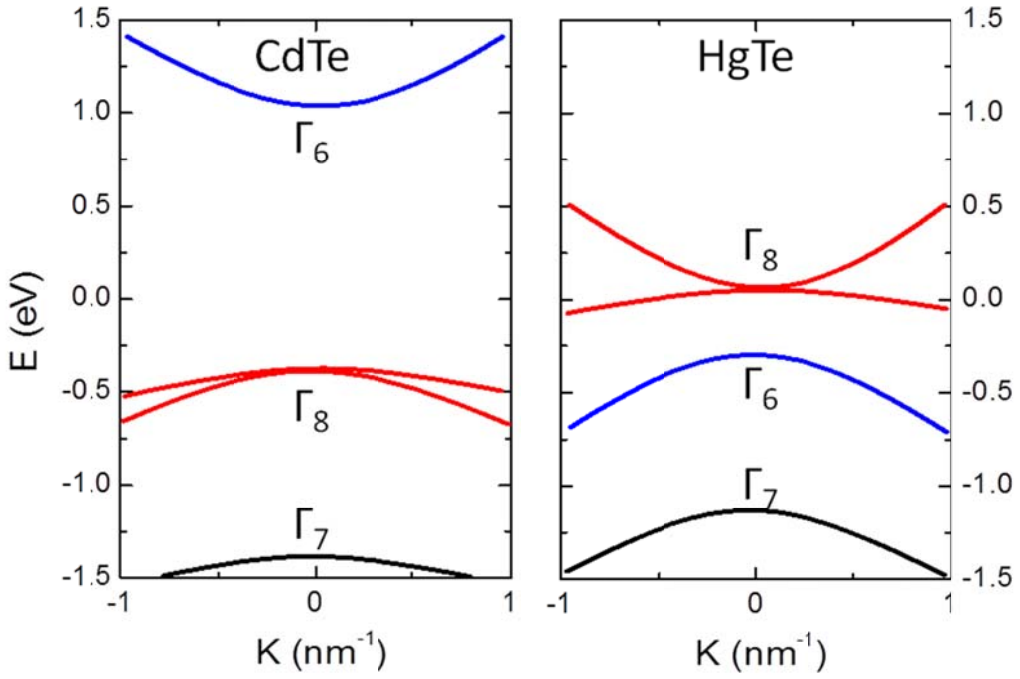

Figure 1-1. band structure of HgTe and CdTe.[10]

Bernevig-Hughes-Zhang (BHZ) model[10] (on type III HgTe/GdTe quantum wells)

Both HgTe and CdTe have the zinc-blende lattice structure, which is simply constructed by shifting two face-centred-cubic (FCC) lattices with different atoms along their body diagonal.[14] They also share the T_d (tetrahedral) point group symmetry due to their broken inversion symmetry.[14, 72] Focusing on the Γ point in the Brillouin zone centre, the six-fold degenerate *p*-like states and double degenerate *s*-like states (Γ_6) give an 8 band $k \cdot p$ Hamiltonian of the Kane model.[14, 73-75] In particular, the *p*-like states split into a Γ_7 doublet (J=1/2) and Γ_8 quartet (J=3/2)

under the SOC effect.[26, 73-76] As shown in Figure 1-1, one important quantity is the energy gap between Γ_6 and Γ_8 ($E_{\Gamma_6} - E_{\Gamma_8}$), which is +1.6 eV for bulk CdTe and -0.3 eV for bulk HgTe.[72] The negative gap suggests that the HgTe has the inverted band structure, corresponding to the large intrinsic SOC in the heavy element Hg.[72]

As for the HgTe/CdTe QWs, it is well known that the SOC effect is a function of the thickness of the HgTe layer. When the HgTe layer is sandwiched by two CdTe barrier layers, the electrons are confined in the 2D HgTe "well". This 2D electron gas (2DEG) system has the peculiar behaviour of band inversion with respect to the confinement effect of the CdTe layers and the SOC intensity, and therefore is susceptible to the well thickness. For example[14, 26, 72-76], in thin QWs, the confinement effect from the barrier layers takes over the SOC of HgTe, and the conduction bands are constructed with a set of QW states derived from the Γ_6 band (denoted as E_n). The valence bands originating from the Γ_8 band are divided into two different sets (H_n and L_n) of QW states corresponding to the degeneracy between the heavy hole and light hole bands. The subscript n refers to the number of nodes of well states in the z direction. When the thickness of the well increases to a critical point (d_c) where the SOC dominates the confinement effect, there is a band inversion between H_1 and E_1, which is schematically described in Figure 1-2.[10] Consequently, the energy gap of the HgTe/GdTe QW is tuneable by varying the thickness of the HgTe "well". The computed critical thickness resulting in band inversion in HgTe/GdTe QWs is about 6.3 nm.[10, 14] During the process of increasing the HgTe thickness, the SOC in the HgTe/CdTe QW system is enhanced, and the band inversion occurs. The inverted band structure probably opens a gap in the bulk, but

gapless states remain at the edge, which provides an opportunity for observing the QSHE.

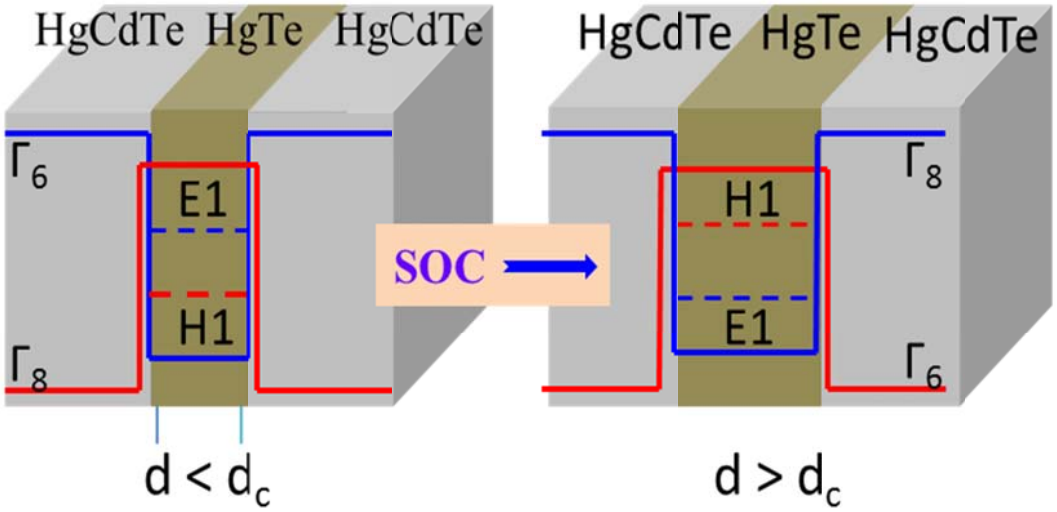

Figure 1-2. Band inversion scheme of HgTe/CdTe QWs with respect to the well thickness.

The 8-band Kane model is reduced to a 6-band model by neglecting the spin-obit split-off band (Γ_7), since the splitting is as large as about 1 eV.[10, 74, 77] Meanwhile, in the QW states,[78] the L_1 band is also discarded because it is too far in energy from E_1 and H_1 to have an impact on the band inversion. Finally, the basis for constructing the 4 band BHZ model is two pairs of Kramers partners ($|E_1 \pm\rangle$ and $|H_1 \pm\rangle$) under the protection of the time reversal symmetry.[10] The effective Hamiltonian of the 4-band BHZ model is[10]:

$$\mathcal{H} = \begin{pmatrix} H(\mathbf{k}) & 0 \\ 0 & H^*(-\mathbf{k}) \end{pmatrix} \tag{1-1}$$

$$H(\mathbf{k}) = \epsilon(\mathbf{k})\mathbf{I}_{2\times 2} + \mathbf{d}(\mathbf{k}) \cdot \boldsymbol{\sigma}$$

$$\epsilon(\mathbf{k}) = C - D(k_x^2 + k_y^2)$$

$$d_x(\mathbf{k}) = Ak_x$$

$$d_y(\mathbf{k}) = -Ak_y$$

$$d_z(\mathbf{k}) = M(\mathbf{k})$$

$$M(\mathbf{k}) = M - B(k_x^2 + k_y^2)$$

where $\mathbf{I}_{2\times2}$ is the 2 × 2 identity matrix, σ^a is the Pauli spin matrix. *A*, *B*, *C*, *D*, and *M* are parameters determined by the material geometry. The parameter *C* is usually neglected, because it is just a constant that shifts the total energy, and can always be renormalized to zero without changing any details of the wave function.[14] The Hamiltonian in Eq. (1-1) is a block diagonal, where the lower block $h^*(-\mathbf{k})$ is the time reversal of the upper block.[10, 79] As a result, the two blocks can be solved separately. We can first solve the eigenvalue for the upper block. Let:

$$\Psi_\uparrow(\mathbf{k}) = \begin{pmatrix}\varphi_1\\ \varphi_2\end{pmatrix} e^{i\mathbf{k}\cdot\mathbf{r}}, \tag{1-2}$$

and the solution for the lower block:

$$\Psi_\downarrow(\mathbf{k}) = \Theta\Psi_\uparrow(\mathbf{k}), \tag{1-3}$$

where $\Theta = -i\sigma_y K$ is the time reversal operator where K is the complex conjugation. The eigenstates of the upper block fulfil the Schrödinger equation, the energy dispersion for the bulk states are:

$$\varepsilon_s(k) = -Dk^2 + s\sqrt{(M - Bk^2)^2 + A^2k^2}. \tag{1-4}$$

Here $s = \pm1$ represents the conduction and valence bands. To investigate the helical edge states in the QSH system, the HgTe/CdTe QW is treated in a finite size, e.g. an

infinite strip in the x direction and a finite length in the y direction.[14, 79] Thus, k_y is not a good quantum number anymore, and is replaced by $-i\partial_y$ following the Peierls substitution. The $G(k)$ term is also neglected since it doesn't affect the wave function. Then, we have:

$$\left[M - B\left(k_x^2 + \partial_y^2\right)\right]\varphi_1 + A\left(k_x + i\partial_y\right)\varphi_2 = \varepsilon_s(k)\varphi_1; \tag{1-5}$$

$$A\left(k_x - \partial_y\right)\varphi_1 - \left[M - B\left(k_x^2 + \partial_y^2\right)\right]\varphi_2 = \varepsilon_s(k)\varphi_2; \tag{1-6}$$

The gapless edge states exist with $E = 0$. Using the wave function ansatz $\varphi = e^{\lambda y}$ at $k_x = 0$, Eq. (1-5) and (1-6) become:

$$(M - B\lambda^2)\,\varphi_1 + iA\lambda\varphi_2 = 0; \tag{1-7}$$

$$iA\lambda\varphi_1 + (M - B\lambda^2)\varphi_2 = 0; \tag{1-8}$$

λ is solved:

$$\lambda_{1,2} = \frac{1}{2B}\left(A \pm \sqrt{A^2 - 4MB}\right). \tag{1-9}$$

Accordingly, the edge states survive only when λ is real and $M/B > 0$. From Eqs. (1-7) and (1-8), the wave function of the upper block has the form:

$$\Psi_\uparrow(k_x, y) = \left[\left(ae^{\lambda_1 y} + be^{\lambda_2 y}\right)\begin{pmatrix}1\\ i\end{pmatrix} + \left(ce^{-\lambda_1 y} + de^{-\lambda_2 y}\right)\begin{pmatrix}1\\ -i\end{pmatrix}\right] e^{ik_x \cdot x}. \tag{1-10}$$

The coefficient a, b, c, d can be determined from the boundary conditions. The wave function for the lower block has the form:

$$\Psi_\uparrow(k_x, y) = \left[\left(ae^{\lambda_1 y} + be^{\lambda_2 y}\right)\begin{pmatrix}i\\ 1\end{pmatrix} - \left(ce^{-\lambda_1 y} + de^{-\lambda_2 y}\right)\begin{pmatrix}i\\ -1\end{pmatrix}\right] e^{ik_x \cdot x}. \tag{1-11}$$

Using Eq. (1-10), and (1-11) as the basis, the effective edge model can be obtained:

$$H_{ij}^{ed} = \langle \Psi_i | \mathcal{H} | \Psi_j \rangle, \tag{1-12}$$

where the effective Hamiltonian to the first order in k_x for the helical edge states is:

$$H^{ed} = Ak_x\sigma^z. \quad (1\text{-}13)$$

The edge Hamiltonian has a similar form to that of graphene, except that the Pauli matrix represents the real spin in TI, but the psuedospin in graphene. The energy dispersion for the edge states is:

$$\varepsilon_s^{ed}(k_x) = sAk_x, \quad (1\text{-}14)$$

where $s = \pm 1$. The velocity of electrons along the *x* direction at the edge state can be calculated from $A = \hbar v_F$. In HgTe/CdTe QWs, A = 3.654 eV·nm, $v_F \cong 5.5 \times 10^5\ m/s$,[10, 14] which is comparable to the parameters for graphene.

3D topological model[53, 80]

SOC can play an important role in the band structure of Bi-based compounds. In the research on $Bi_{1-x}Sb_x$ of Hsieh et al.[54], the Sb is treated as substituting for the Bi and plays the role of manipulating the SOC. Since Bi is a semimetal with strong SOC, while Sb has weaker SOC, the Sb concentration has a negative effect on the intrinsic SOC of the compound. The inversion of the L_a and L_s bands occurs when x = 0.04, leading to a massless, Dirac cone band structure. As the concentration of Sb falls into $0.07 < x < 0.08$, the band T crosses band L_a and still lies above band L_s, so a gap opens in the inverted band structure. In the regime $x \geq 0.08$, band T finally drops below L_s, so that a SOC dependent direct gap insulator is formed. Therefore, with increasing concentration of Sb, the band structure of Bi changes into that of a semimetal, and then an inverted band insulator, so that the material finally becomes a direct-gap insulator with nontrivial gapless surface states, see Figure 1-3(d).[54]

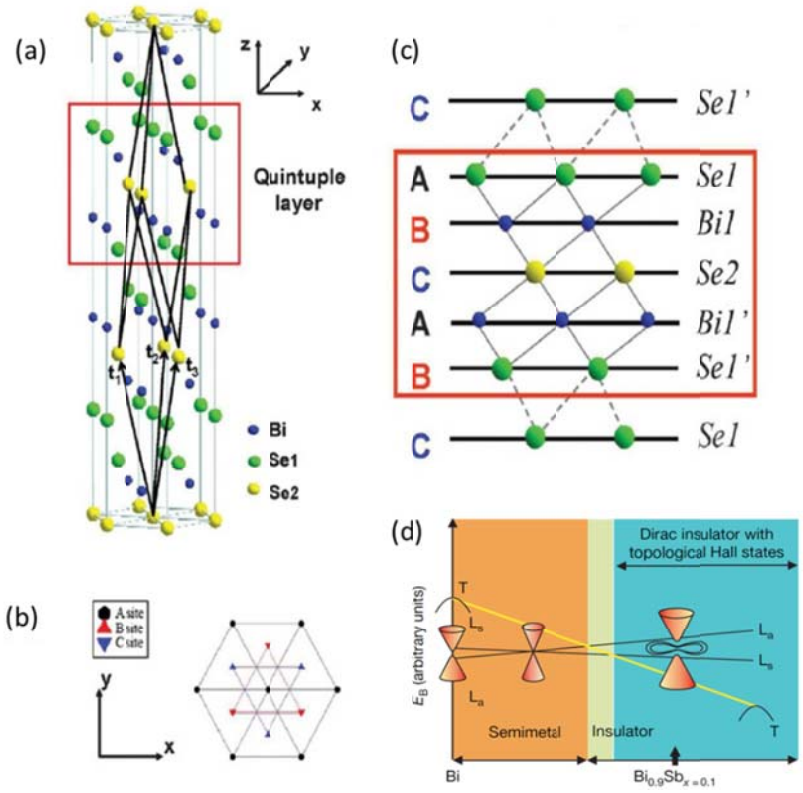

Figure 1-3. (a) Crystal structure of Bi_2Se_3 with five atoms as one quintuple layer, as indicated by the red box. (b) Triangular lattice in one quintuple layer has three different positions, denoted by A, B, and C. (c) The Se and Bi atomic layers are stacked in the order of ABCAB.[53] (d) Band inversion scheme of $Bi_{0.9}Sb_{x\text{-}0.1}$.[54]

Bi-based compounds such as Bi_2Se_3, Bi_2Te_3, Bi_2Sb_3 and Sb_2Te_3 have been extensively studied in theoretical models.[3, 4, 51-53, 80-84] These compounds share the same rhombohedra crystal structure with space group $R\bar{3}m$, as shown in Figure 1-3(a).[53] Figure 1-3(b) shows the ABC hexagonal stacking structure from the top perspective. Along the z direction, five atoms make up a unit cell in the sequence Se1-Bi-Se2-Bi-Se1 (Figure 1-3(c)). The five-atom layer in the layer structure is usually called a quintuple layer (QL) with the thickness of about 1 nm, which is

highlighted in the red frames in Figure 1-3(a) and (c). The interaction between quintuple layers is much weaker than the atom-atom interaction in each quintuple layer. The weak interaction between quintuple layers is ascribed to the van der Waals force.

An effective Hamiltonian for the 3D TIs was proposed by Zhang et al[53], who considered the four bases: $|P1_z^+,\uparrow\rangle$, $|P2_z^-,\uparrow\rangle$, $|P1_z^+,\downarrow\rangle$ and $|P2_z^-,\downarrow\rangle$, and three symmetries: TRS, inversion symmetry and three-fold rotation symmetry. The 4×4 effective Hamiltonian up to the order of $O(\mathbf{k}^2)$:

$$\mathcal{H} = \epsilon(\mathbf{k})I_{4\times4} + \begin{pmatrix} M(\mathbf{k}) & A_1k_z & 0 & A_2k_- \\ A_1k_z & -M(\mathbf{k}) & A_2k_- & 0 \\ 0 & A_2k_+ & M(\mathbf{k}) & -A_1k_z \\ A_2k_+ & 0 & -A_1k_z & -M(\mathbf{k}) \end{pmatrix} + O(\mathbf{k}^2) \tag{1-15}$$

where:

$$k_\pm = k_x \pm ik_y$$

$$M(\mathbf{k}) = M - B_1k_z^2 - B_2k_\perp^2$$

$$\epsilon(\mathbf{k}) = C + D_1k_z^2 + D_2k_\perp^2$$

The effective surface Hamiltonian is the projection of Eq. (1-15) onto the surface states:

$$H^{surf}(k) = \begin{pmatrix} 0 & A_2k_- \\ A_2k_+ & 0 \end{pmatrix} \tag{1-16}$$

This is very similar to the Hamiltionian of graphene except that here the spin representation is describing the real spin. The Fermi velocity of the surface states is $v_F = \frac{A_2}{\hbar} = 6.2 \times 10^5\ m/s$.

1.2.2 Topological invariants of TIs: Z_2 invariants[3-6, 51, 52, 69, 85]

The word 'topological' in 'topological insulator', originates from a branch of geometry, topology, which studies the properties of the shapes and spaces of an object under continuous deformation or "smooth deformation".[1] One oft-used example is the discussion of the deformation between a sphere and a doughnut.[2] In this case, the topological invariant, or genus g, of a physical object is described by the number of holes in the object. A sphere has no hole giving $g = 0$, while a doughnut has one hole with $g = 1$, as illustrated in Figure 1-4. Topologically speaking, by applying a pressure to a sphere, e.g. squeezing or stamping, the sphere could be deformed into an ellipsoid via a "smooth" or "continuous" process so that the genus g remains unchanged. It is impossible, however, for a sphere to be deformed into a doughnut (with $g = 1$) without any violent actions such as ripping and tearing, which could break open a hole.

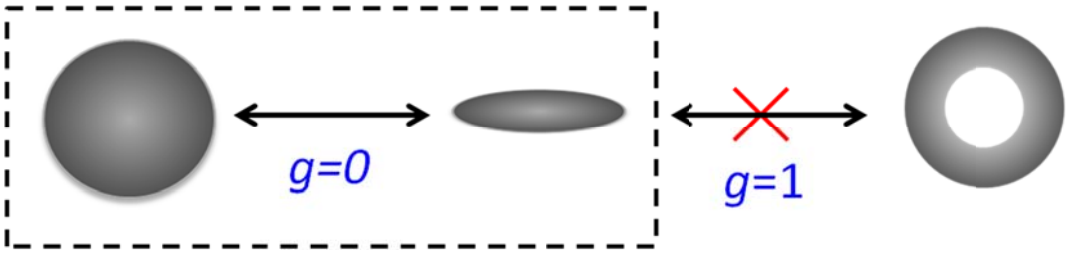

Figure 1-4. Schematic illustration showing the concept of topology. A sphere is topologically equal to an ellipsoid with the same genus $g = 0$, but they are a different genus from a torus as a hole can't be created without violent action, such as splitting.

Analogously, the topological invariants are described by Z_2 invariants, which are determined by counting the number of Kramers-degenerate Dirac points on the edge (in 2D) or surface (in 3D) band structure.[3, 6] In 2D TIs, the Z_2 topological invariants

of value $v = 0$ or $v = 1$ correspond, respectively, to an ordinary insulator or a topological insulator, where topological states are protected by time reversal symmetry (TRS) from any non-magnetic impurities.[6] In 3D TIs, there are four Z_2 invariants, $v_0;(v_1, v_2, v_3)$. These four Z_2 invariants describe 16 phases that not only distinguish the trivial and non-trivial surfaces states, but also divide the TIs into two categories regarding to the value of v_0: the strong topological insulator (STI) with $v_0 = 1$, and the weak topological insulator (WTI) with $v_0 = 0$.[3-5, 51, 52] A WTI can be understood as a stack of layers of 2D TIs, whose surface consists of even numbers of Dirac cones that only survive in the absence of disorder.[51] A STI, however, possesses an odd number of Dirac cones, where the electrons are spin-momentum locking and immune to any time reversal invariant (TRI) impurity.[51]

There are several mathematical formalisms to establish the Z_2 classification. TRS is the core factor resulting in Z_2 topological invariants. The TRS operator is an antiunitary operator:

$$\Theta = e^{i\pi S_y/\hbar}K \tag{1-17}$$

Where S_y is the spin operator, and K is the complex conjugation. When the TRS operator acts on a Bloch Hamiltonian, a constraint will be imposed that guarantees that the Z_2 invariant Hamiltonian will be smoothly deformed without closing a gap.

$$\Theta H(\mathbf{k})\Theta^{-1} = H(-\mathbf{k}) \tag{1-18}$$

For electrons with half spin,

$$\Theta^2 = -1 \tag{1-19}$$

This property immediately corresponds to the Kramers theorem that the eigenstates in the TRS system are at least doubly degenerate. Thus the edge states at

the Brillouin zone boundary $k_x = \pi/a$ or $k_x = 0$ form a Kramers pairs that cannot be lifted by any TRS perturbation.

In the KM model,[6] the matrix of overlaps $\langle u_i(\mathbf{k})|\Theta|u_j(\mathbf{k})\rangle$ needs to be considered to identify the 2D Z_2 invariant. $u_{i,j}(\mathbf{k})$ is the Bloch wave function corresponding to the Bloch Hamiltonian$H(\mathbf{k})$. Under the TRI, the determinant of the overlap matrix is the related to its Pfaffian $P(\mathbf{k})$:

$$P(\mathbf{k}) = Pf\left[\langle u_i(\mathbf{k})|\Theta|u_j(\mathbf{k})\rangle\right] \tag{1-20}$$

Finding the Z_2 invariants is now become the problem of finding the zeros of $P(\mathbf{k})$. Without the constraint of any spatial symmetry, the Z_2 index can be determined by the following integral:

$$I = \frac{1}{2\pi i}\oint_C d\mathbf{k}\cdot\nabla_{\mathbf{k}}\log[P(\mathbf{k}) + i\delta] \tag{1-21}$$

where C is the path enclosing half the Brillouin zone. This integral evaluate the winding of the phase of $P(\mathbf{k})$ around path C. It is important to point out that the Z_2 invariants are robust against any TRI perturbation. For example, in the presence of S_z symmetry, the opposite spins propagate in opposite directions, and each spin has independent Chern integers $n_\uparrow$, $n_\downarrow$. TRS requires $n_\uparrow + n_\downarrow = 0$, and the difference $n_\uparrow - n_\downarrow$ defines the quantized spin Hall conductivity. Z_2 invariants in the graphene system can be extended to other many-body system and 3D TI systems.[11]

1.2.3 Dissipationless transport on the edge or surface of TIs

The Kramers degeneracy at the Dirac cone of the surface is protected by the TRS, which means that elastic backscattering from any TRI impurities is forbidden. Since charge current is odd under TRS, when the opposite spin currents flow in two

opposite directions, the net charge current is zero. The electric field and the spin current are TRI, however, so the transport of two opposite spin-currents on the edge or surface is dissipationless as long as there is no spin dependent perturbation.

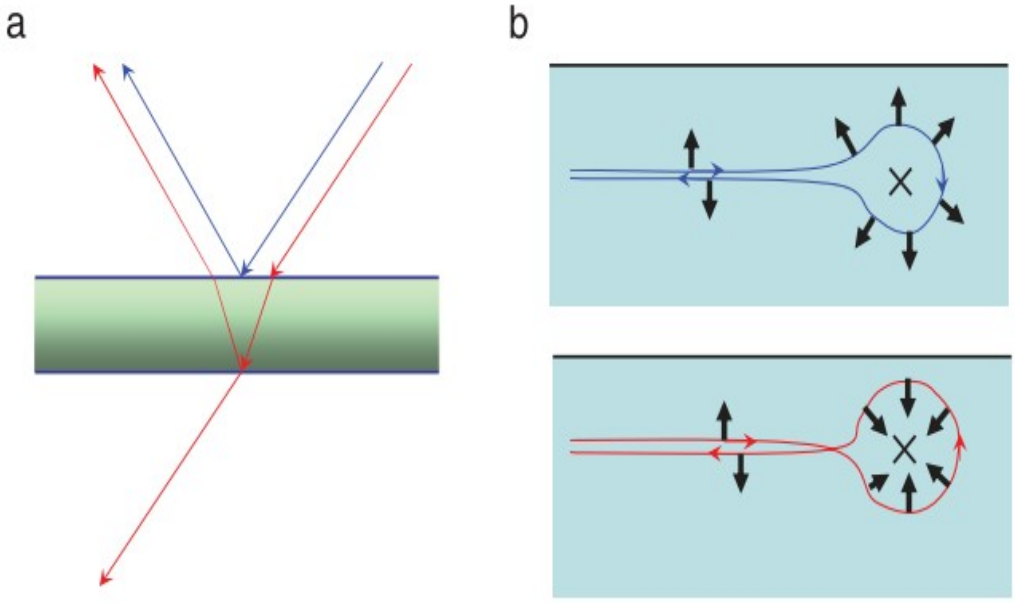

Figure 1-5. (a) Model to describe the mechanism of light interference on a lens with an anti-reflective coating. (b) Two backscattering paths of the electrons rotating around an impurity related to time reversal will always interfere destructively.[1, 86]

To better understand the dissipationless transport, Zhang et al[1, 86] proposed a model that analogous to the mechanism for the reflection of a lens with an anti-reflection coating, as depicted in Figure 1-5. Consider that in a lens with an anti-reflection coating, the reflected light from the top and bottom can interfere destructively, resulting in high transmission. Similarly, electrons can rotate around impurities by an angle π in the clockwise direction or $-\pi$ in the counter-clockwise direction. Hence, the phase difference between the two paths is 2π. It is well known

that the wave function of a spin-1/2 particle will pick up a negative sign by a full 2π rotation. Therefore, two backscattering paths always interfere destructively due to the time reversal. It is worth mentioning, however, that if the impurity is a magnetic particle, TRS can be broken; the robustness of the topological surface states will not be preserved.

1.3 Experimental realization

The TI has become a hot topic that draws much attention from the fundamental research to the potential applications in quantum computing and spintronic devices. The experimental realization is a big challenge, however. First of all, to obtain TIs, the materials should be of high quality, e.g. low bulk carrier density so that the Fermi energy lies in the bulk gap.[13, 23] Second, 1D edge states on 2D TIs have so far not been directly confirmed, unlike those in 3D TIs, which were observed using angle resolved photo-emission spectroscopy (ARPES) and scanning tunnelling microscopy (STM). In the 3D TIs, the transport measurements are always accompanied by the bulk response.

1.3.1 Experimental realization of 2-dimentional TIs

Molenkamp's group, in the University of Würzburg, has been working on HgTe/CdTe QWs since 2001. They fabricated high quality HgTe/CdTe QWs with high electron mobility and low bulk carrier density using the molecular beam epitaxy (MBE) technique.[75, 87-91] The HgTe/CdTe QW has the structure sketched in Figure 1-6(a)[14], where the doping layers can effectively separate the 2DEG in the well from

the ionized donors in the undoped spacer layer, and therefore significantly increase the electron mobility. At zero gate voltage, the carrier density in *n*-type HgTe/CdTe QWs is between 1.3×10^{11} and 1.5×10^{11} cm^{-2}. Applying a gate voltage between top layer and well layer can modulate the carrier density of the well. The Hall bar structure of the HgTe well for measurement is shown in Figure 1-6(b). Such measurements demonstrated that, in the absence of a magnetic field, quantum Hall edge channels could be observed in the inverted-band samples, transporting two opposite spin current in opposite directions, which did not suffer energy-dissipation. The measurement of Figure 1-6(c) is based on a sample with a Hall bar that is about 20.0 μm × 13.3 μm. The well thickness varies from 4.5 nm to 12 nm, which crosses the critical value (d_c = 6.3 nm) of the phase transition. The measured plateau of residual conductance for the sample 8.0 nm thick was very close to the predicted value of $2e^2/h$, where e is the electron charge, and h is Plank's constant.

They also performed non-local measurements that could distinguish the ballistic and edge channel transport of HgTe/CdTe QW TIs in a more convincing way.[92, 93] The samples were designed with H-shaped structures on HgTe/CdTe QWs using electron beam lithography. The authors argued that the spin current transport along the helical edge channels encountered the quantized nonlocal resistance of $h/4e^2$, so the helical edge states can be understood as two copies of chiral edge states protected by the time reversal symmetry and are immune to the backscattering. In another work[94], they also declared that their HgTe/CdTe QWs established that topological edge states consist of a single, spin-degenerate Dirac valley. In contrast to graphene, which contains two valleys and two Dirac cones, the "half-graphene" features in the

HgTe/CdTe QW TIs with single pairs of Dirac cones provide a suitable way to study the physics of the Dirac fermions.

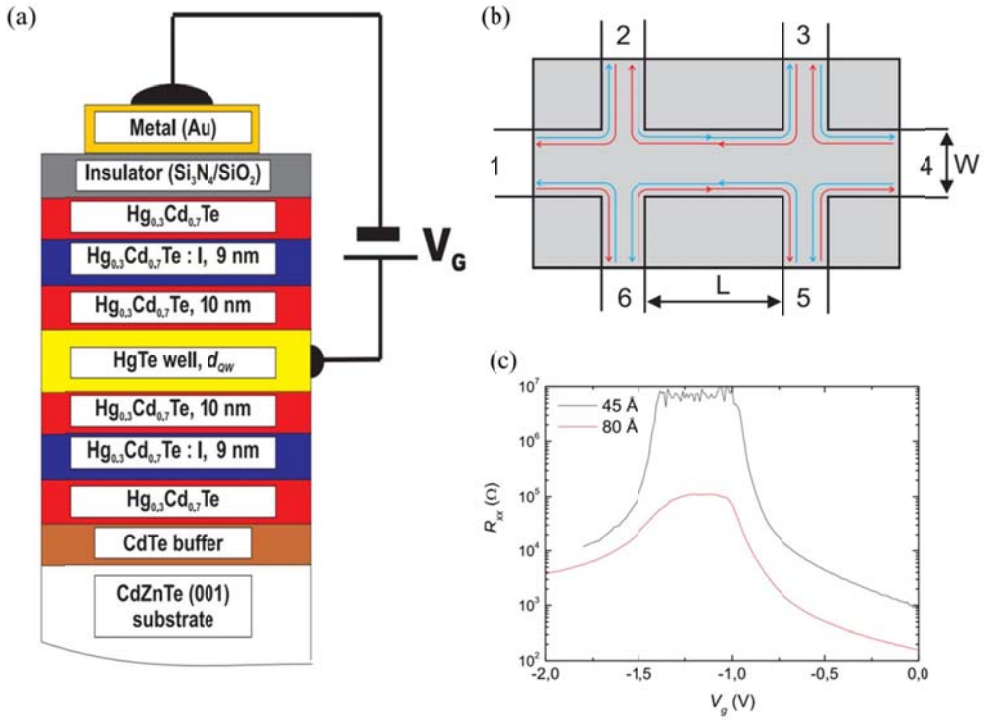

Figure 1-6. (a) Schematic structure of HgTe/CdTe QWs; (b) the Hall bar structure of HgTe/CdTe QWs for measurements; (c) the longitudinal four-terminal resistance of a 4.5 nm QW and an 8.0 nm QW as a function of gate voltage.[14]

1.3.2 Experimental realization of 3-dimentional TIs

Most 3D TI materials are conventional thermoelectric materials with new properties based on TI theory that were discovered with the help of advance techniques such as ARPES, STM and STS, as well as optical techniques and transport measurements.

Angle-resolved photo-emission spectroscopy (ARPES)

ARPES is one of the most direct methods for studying the electronic structure of the surfaces of solids. $Bi_{1-x}Sb_x$ was the first experimentally confirmed family of 3D TIs. To identify the non-trivial surface states, Hsieh et al.[54] employed ARPES to monitor the band dispersion around the L point of the bulk Brillouin Zone with varying incident photon energy. The second-derivative image is shown in Figure 1-7(a). The odd numbers of crossings along the $\bar{\Gamma} - \bar{M}$ direction correspond to the five components of the Fermi surface for the topological surface states (in Figure 1-7(b)), which suggests their non-trivial nature.

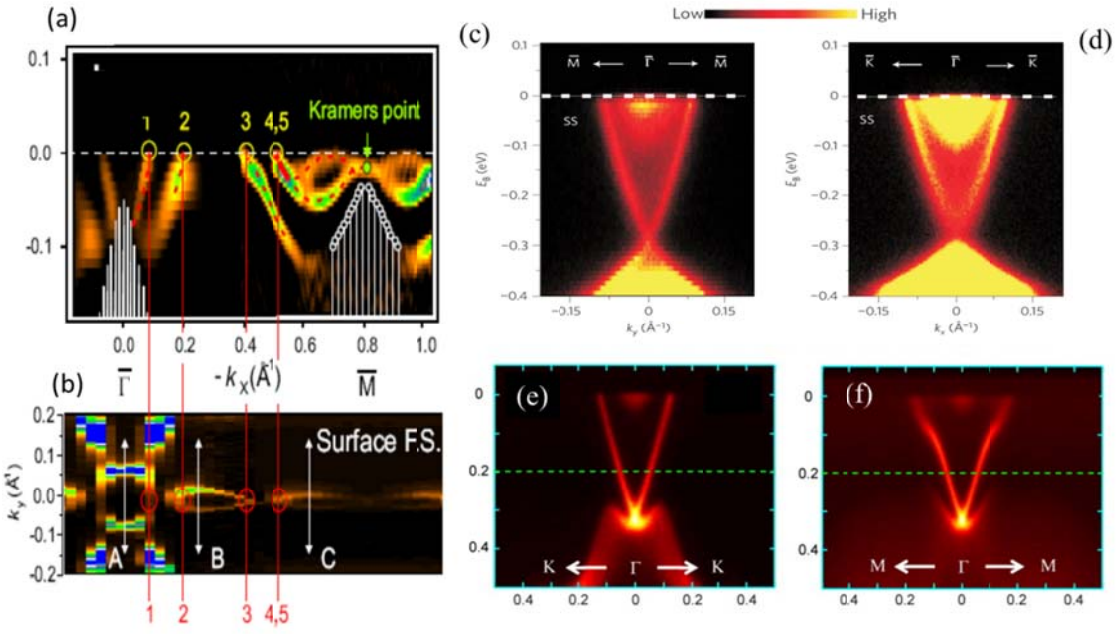

Figure 1-7. (a) Second derivative image from ARPES data. Along the $\bar{\Gamma} - \bar{M}$ cut of $Bi_{0.9}Sb_{0.1}$, there are five crossings forming the Fermi surface for the topological surface states (b).[54] (c), (d) are ARPES images of Bi_2Se_3[7] and (e), (f) are ARPES images of Bi_2Te_3[62]. The mapping cuts were along the $\bar{M} - \bar{\Gamma} - \bar{M}$ and $\bar{K} - \bar{\Gamma} - \bar{K}$ directions respectively.

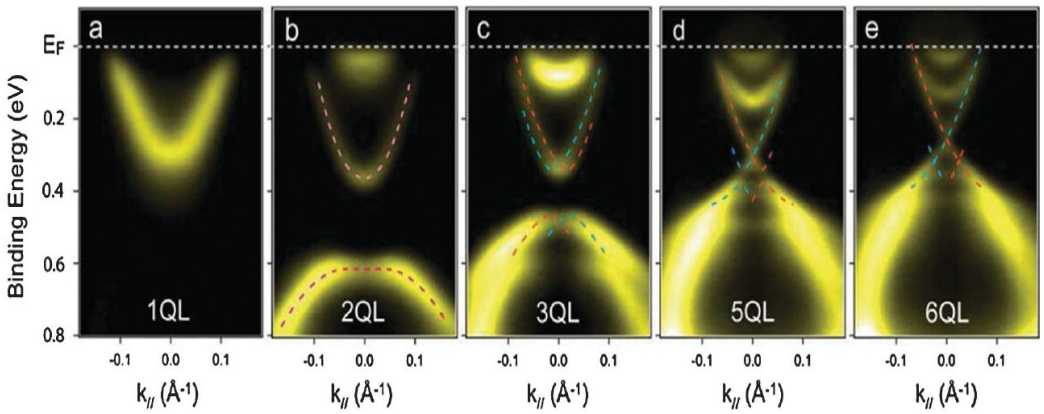

Figure 1-8. Surface band structures of Bi_2Se_3 thin films with different thicknesses from ARPES.[59]

Following the theoretical predictions,[51, 53, 95] massive experimental observations were reported based on APRES on TI materials surch as Bi_2Te_3 and Bi_2Se_3, Sb_2Te_3, strained HgTe, etc.[7, 8, 23, 24, 59, 61-63, 96] Figure 1-7(c-f) shows the observation of a single Dirac cone on the surface of Bi_2Se_3 and Bi_2Te_3 TIs, respectively, which proves the existence of the topological non-trivial surface states in the theoretical predictions.[7, 53, 62] Doping-dependent band structures near the Dirac points were also studied by ARPES.[23, 62] By monintoring the band evolution, they were able to locate the Fermi energy, E_F, on surface or edge Dirac points within the bulk gap for the observation of topological surface states. For example, Chen et al.[62] reported the experimental realization of Bi_2Te_3 with Sn doping. The band structure evolution with doping concentration suggested that the bulk states disappear completely at the Fermi surface with Sn doping of 0.67%, and the shapes change from a hexagram to a hexagon. Another interesting study by Zhang et al.[59] investigated the surface states evolution of Bi_2Se_3 with varying numbers of layers. A series of ARPES band maps are shown in Figure 1-8, where the overlapping of wave functions from the two

opposite surfaces plays an important role when the thickness of the film is reduced to below 6 QLs with the opening up of a gap. They also claimed that the Rashba-split resulting from the substrate induced a potential between the two opposite surfaces.

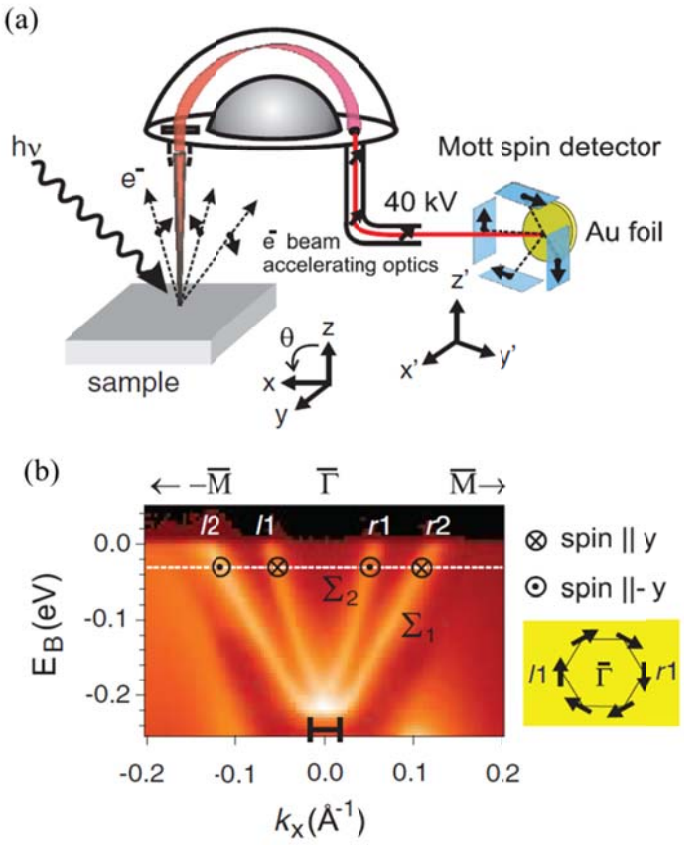

Figure 1-9. (a) Schematic illustration of spin-integrated ARPES (b) Spin integrated ARPES spectrum of Sb(111) in the $\bar{M} - \bar{\Gamma} - \bar{M}$ direction, with the spin texture scheme sketched in the inset.[63]

In order to study the spin texture on the Fermi surface, Hsieh et al.[63] designed a spin-integrated ARPES technique, as displayed in Figure 1-9(a), where a Mott polarimeter was equipped to measure the two spin components of a photoemitted electron along the y′ and z′ directions. The gold (Au) foil can create an asymmetry

for the scattering of the photoelectron, resulting in asymmetry scattering intensity on the right and left. Figure 1-9(b) shows the momentum splitting that enabled the spin resolved study. The authors discovered a new type of topological quantum number, n_M, which describes the spin-handedness of the Fermi surface that supports the nontrivial Berry's phase.

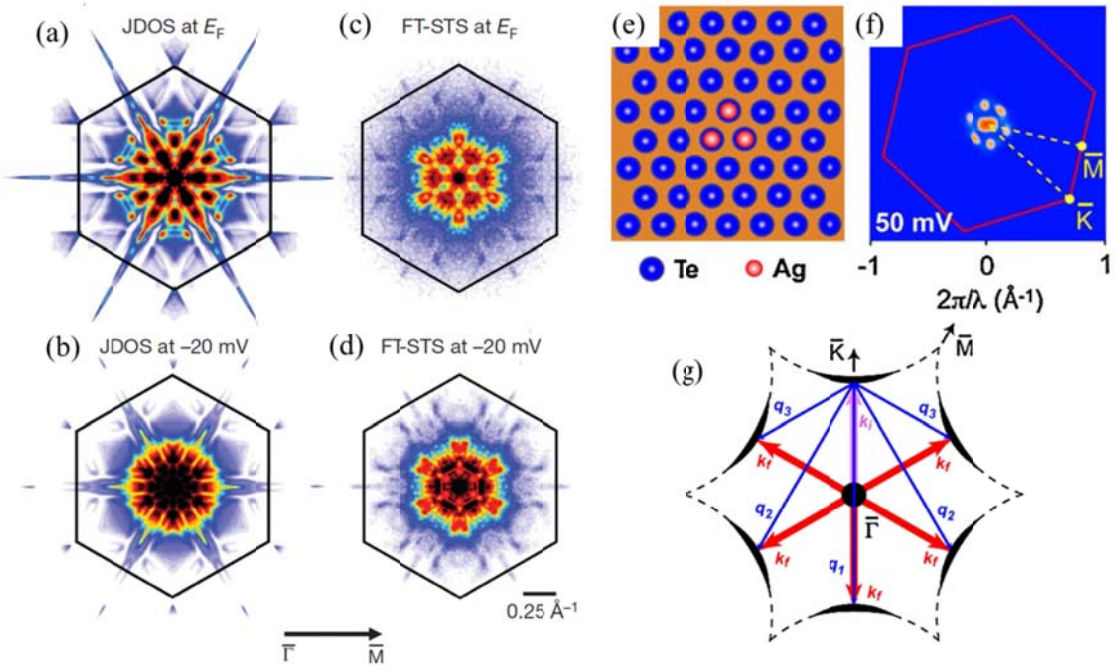

Figure 1-10. (a), (b) Calculated joint density of states from ARPES data; (c), (d) quasi-particle interference pattern from FT-STS.[55] The data was collected from random alloying Bi_xSb_{1-x} at Fermi level (a, c) and 20 meV below (b, d), respectively, from random alloying Bi_xSb_{1-x} along the $\bar{\Gamma} - \bar{M}$ direction. (e) Ag trimer on the Bi_2Te_3 surface, (f) Fourier transform of the *dI*/*dV* maps from STM data; (g) the scattering scheme.[15]

STM and STS

STM is a powerful technique for imaging surfaces at the atomic level by moving the tip across the sample, while STS measures the tunnelling current at a specific point by sweeping the voltage, which gives information on the local density of states. Therefore, STM and STS enable analysis of the scattering process resulting from non-magnetic impurities on the TI surface.[15, 25, 55, 57, 67, 97-100]

As shown In Figure 1-10, Roushan et al.[55] conducted the energy-resolved Fourier transform scanning tunnelling spectroscopy (FT-STS) and determined the joint density of state (JDOS) from ARPES of random alloying Bi_xSb_{1-x}. The quantum interference between different momentum states at the same contour of constant energy was compared to the JDOS. Due to the spin scattering rules, scattering caused by random alloying was suppressed along the high-symmetry directions (e.g. $\bar{\Gamma} - \bar{M}$ direction) at the chiral electronic states, while the scattering between states with opposite spin orientations was suppressed completely. Zhang et al[15] performed a similar experiment on Bi_2Te_3, demonstrating that the topological states are protected by the TRS in the presence of non-magnetic impurities (here Ag). From the FT-STS spectrum, they argued that the scattering along $\bar{\Gamma} - \bar{K}$ direction was forbidden, because the initial states $|\vec{k}\uparrow\rangle$ and final states $|-\vec{k}\downarrow\rangle$ are TRI, and thus the scattering density vanishes. The results offered direct proof that backscattering is forbidden between states that are TRI. Alpichshev et al[25] have reported a combined study of ARPES and STM. The local occupied density of states obtained by integrating the ARPES intensity over the Brillouin zone (BZ) matches very well with that directly measured from STM, which makes it possible to distinguish scattering in different energy regimes, as shown in Figure 1-11.

STM techniques were extensively used to investigate other aspects of TI materials such as: the transmission and reflection probabilities across the terrace surface states on a TI system[67], the surface-state Landau levels in the presence of magnetic field[57], and the response to magnetic and non-magnetic impurities of the topological surface states[97].

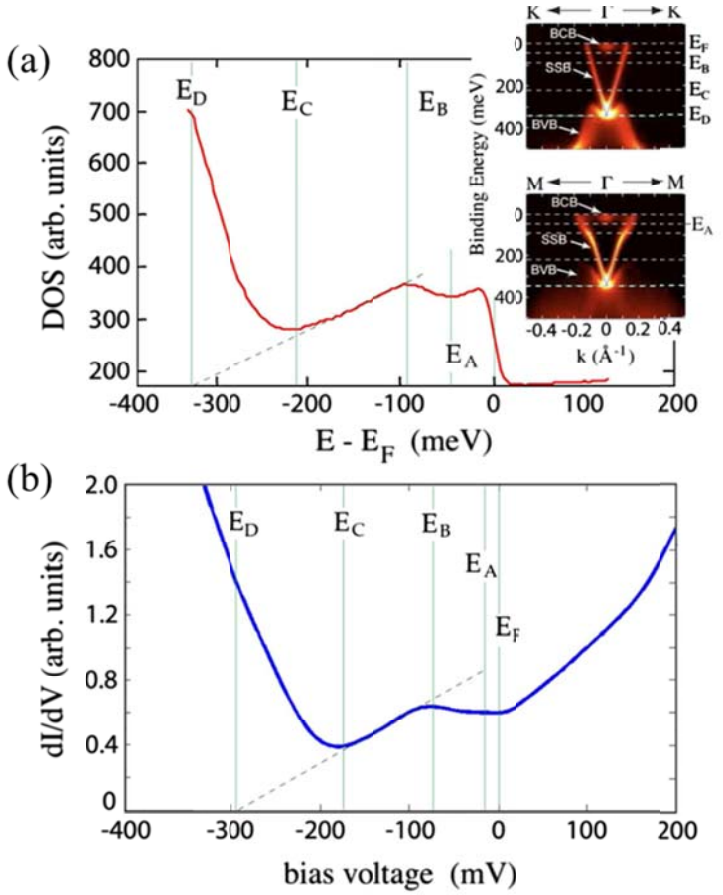

Figure 1-11. Density of states calculated from ARPES data (a) and STM (b). The insets are the ARPES spectra in two different cuts.[25]

Since ARPES provides information on the surface states band structure, for example that an odd number of Dirac points with Kramers degeneracy crosses the Fermi level, and STM and STS give scattering information on the topological

surface states, the application of the two techniques has brought the TI from a theoretical concept to experimental realization, which paves the way for possible device applications in quantum computing and spintronics.

Optical techniques and transport measurement

In addition to ARPES and STM, other experimental measurements face many difficulties when they are used to study the gapless surface state of TIs, such as the residual carrier density and the fact that the sample surface easily becomes *n* doped when exposed to the air, which would introduce a noise background or even change the intrinsic properties of the materials.[59, 62]

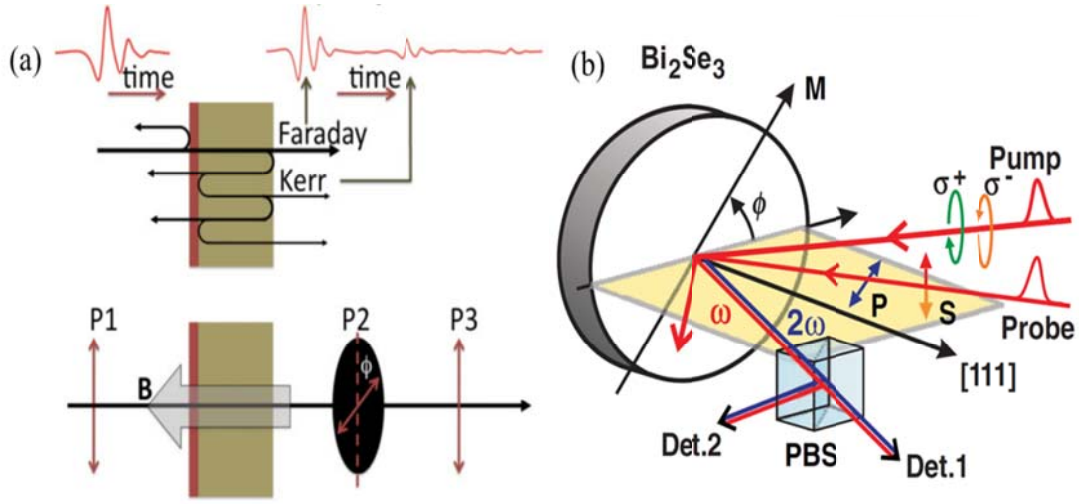

Figure 1-12. (a) Schematic illustration of optical measurement of a thin film with pulsed terahertz light.[101] (b) Experimental geometry of for SHG measurement.[102]

Optical techniques are useful tools for studying electronic properties of solids, for they have the advantages of no contact and no damage to the samples, especially

in the low energy regime. Both theoretical models and experimental optical measurements have been reported on reflection[103-108], transmission[104, 109], Kerr[101, 105, 110, 111] and Faraday rotations[17, 109-111], second-harmonic generation[66, 102], etc., covering the electromagnetic spectrum from the visible[102], to the infrared[103, 104, 106, 109, 112] and terahertz regime[64, 105, 113]. One obstacle to the optical measurements is the problem of how to identify the surface states from the bulk, as the electromagnetic field can interact with the whole sample, including both the surface and the bulk. Some groups have proposed delicate schemes for surface states characterization.[17, 20, 66, 102, 114]

B. V. Aguilar et al[101] devised an interesting measurement scheme using time-domain terahertz spectroscopy (TDTS) on Bi_2Se_3 thin film. TDTS is a time resolved setup that can record a set of responses following the light trace. Figure 1-12(a) shows the mechanism of the measurement, the sapphire substrate acts as an optical resonator. As a terahertz pulse travels through the Bi_2Se_3 thin film, each reflection by the film surface and substrate results in a Faraday rotation and a Kerr rotation, respectively. The rotation angles of the Kerr and Faraday rotation can be resolved in the time domain by using three polarizers as light polarization filters. By analysing the distinct rotation angles, one expects to obtain the optical response from the surface states. Another idea proposed by Hsieh et al[102] is based on the second harmonic generation (SHG) model, which is expressed as: $P_i(2\omega) = \chi^{(2)}_{ijk} E_j(\omega) E_k(\omega) + \chi^{(3)}_{ijkl} \varepsilon_j(0) E_k(\omega) E_l(\omega)$, which is only non-zero on the surface. The measurement scheme is displayed in Figure 1-12(b), where the *s* and *p* polarized photons are collected separately. This method allows selective probing of the in-plane and out-of-plane polarization responses of surface states.

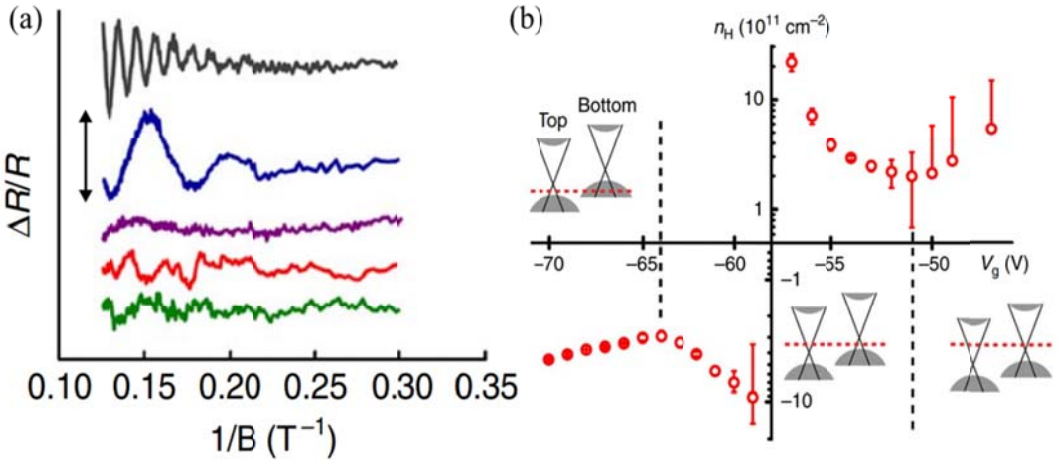

Figure 1-13. (a) SdH oscilations of Bi2Se3 with various Sb doping. (b) Band diagrams of top and bottom surfaces for samples with pure *p*-type conduction (left), mixed conduction (middle), and pure *n*-type conduction (right).[115]

Transport measurements

Transport measurements of the topological surface require high quality materials with high mobility and low bulk carrier density.[116-119] To obtain the surface response, the Fermi energy of the materials should be confined within the bulk gap and right on the Dirac point.[1] Butch et al.[116] have pointed out, however, that even in very high quality material, the electrical transport in undoped Bi_2Se_3 single crystals could be attributed solely to the bulk electrons. The gate-voltage control technique can be used to tune the chemical potential in the low carrier density materials.[60, 120, 121] Kim et al.[121] demonstrated a gate electrode to control the bulk carrier density of Bi_2Se_3, where surface transport was strongly electrostatically coupled when the bulk carriers were removed completely. Nevertheless, the electrostatic gating techniques

are not suitable for bulk crystals and nano-crystals, which have large remnant electron density that cannot be removed completely.[60]

Another efficient way to tune the Fermi level into the bulk gap is by doping. Successful examples have been reported on Ca, Sb, and Mg doped Bi_2Se_3 and Sn doped Bi_2Se_3.[23, 60, 115, 122] Hong et al[115] reported transport measurements of ultra-low carrier concentration Bi_2Se_3 nano-ribbons with varying Sb doping concentration. In high magnetic field, the Shubnikov-de Haas (SdH) oscillations (in Figure 1-13(a) from the bulk) fade with increasing Sb concentration, and vanish at high doping level, suggesting the suppression of bulk carrier density. The Fermi energy level of the Bi_2Se_3 nano-ribbons varied up and down between the valence and conduction bands, as shown in Figure 1-13(b).

Although various theoretical transport models have been established to investigate the surface transport response,[123-131] the transport measurements still remain challenge in the real experiments. One obstacle is the response of the surface states could be always accompanied by that of the bulk in the transport measurements.[18, 119, 120, 132, 133] Thus, the surface transport properties remain elusive if there is no way to distinguish the response from the bulk and surface states. Some outstanding improvements have been made, however, to prove that the surface states may exist, based on phenomena such as weak antilocalization[133-135], the ambipolar gating effect[19, 121, 136], observation of surface channels[137, 138], metallic resistance-temperature profiles[60], ballistic Josephson supercurrents[21], the Hall anomaly of surface states[139], etc.

1.4 Outlook

In recent years, there have been a myriad of research reports on TIs, especially the 3D TIs. 2D metallic surface of the 3D TIs share most of the common properties of graphene, yet they are different from graphene at least in the following aspects: i) the Hamiltonian of a TI surface state represents the real spin; ii) only odd numbered pairs of Dirac cones exist.[53, 140-142] Comparing to the single layer graphene, the 2D surface is easier to fabricate and more stable for application, since it based on the bulk material of itself. The modern techniques, in particular the molecular beam epitaxy (MBE), offer the opportunity to produce high quality materials with ultrahigh mobility, low carrier density, and thickness controlled.

The Bi-based compounds, e. g. Ca-doped Bi2Se single crystal,[143] with bulk insulating gap of 0.3 eV, are suitable for the transport measurement at ~100 K, where the electrical resistance saturates, and the bulk currents dominate the surface currents.[2] Therefore, in the future, new TI materials with larger bulk gap (more than 0.6 eV) are desired for the room temperature measurement and applications.[12]

On the other hand, to distinguish the surface signal from the bulk remain great challenge for more detailed study of the surface states transport. There have been some successful examples that proved the existence of the surface states, such as the case using TTDS to investigate the Kerr and Faraday rotation[101] and the quantum Shubnikov-de Haas oscillation[139]. Nevertheless, future techniques on manipulating or extract the surface spin currents are required for spintronics applications.

Another direction is the study of the hybrid structures based on TIs. Heterostructures such as TI-superconductor, TI-Ferromagnet and superconductor-

magnet-TI are of interesting, as they have been proposed for realizing Majorana fermions, whose antiparticles are their own.[22, 144-147]

With the development of materials fabrication in the atomic level, simultaneously equipped with probing techniques ranging from optical to tunnelling spectroscopy, the subject of TIs is developing in a fascinating pace. Like the birth of graphene, TI has attracted more and more attention. For example, in the field of quantum computer, TI is expected for a new revolution of extending Moore's law. To conclude, the subject of TI has become a "Nobel prize topic", since it stands for a new mile stone in the condense matter physics.

CHAPTER 2 DIELECTRIC FUNCTION OF HGTE/CDTE QUANTUM WELLS

When applying an external field to a dielectric medium, there would be an induced electric field which drives the hole- carriers along the field and the electrons in the opposite direction, namely the self-consistent field. A dielectric function is derived to describe how the electric field is induced in this system by an external electric field. Thus, the dielectric function is the gate way to the study of electron transport properties. By taking the limit of $\omega \rightarrow 0$, the dielectric function gives the static screening function, which describes the electrostatic screening of the electron-electron, electron-lattice, and electron-impurity interactions. Another important result is that when the dielectric function is set to equal to zero, it leads to the solution for the plasmon dispersion relation describing the fundamental elementary excitation and collective density oscillation modes.

In this Chapter, we will first derive the dielectric function using the random phase approximation (RPA), and then apply it to the HgTe/CdTe QWs system.

2.1 Dielectric function in RPA for an interacting system.[148-150]

In the RPA, electrons are assumed to flow in a self-consistent field arising from an external field and the internal field that it induces. In a QW system, electrons are confined in the 2D "well" with a discrete energy distributions giving rise to a band structure. Electrons in a specific energy band (s) are distinguished by their momentum vector $\mathbf{k}$ and spin degree of freedom (σ), which are denoted by (s, $\mathbf{k}$, σ).

An external electric field $\boldsymbol{E}_{ext}\,(\mathbf{A}_{ext}(\mathbf{r},t),V_{ext}(\mathbf{r},t))$ can be interpreted as inserting extra charges into the system. The RPA method assumes that the total response of electrons comes from only two charge density contributions:

$$\rho(\mathbf{r},t)=\rho_{ext}(\mathbf{r},t)+\rho_{ind}(\mathbf{r},t), \tag{2-1}$$

where $\rho_{ext}(\mathbf{r},t)$ is the equilibrium charge density, and $\rho_{ind}(\mathbf{r},t)$ is the induced charge density due to the presence of the external field. The total electric potential is defined by:

$$V(\mathbf{r},t)=\frac{1}{\kappa_r}V_{ext}(\mathbf{r},t), \tag{2-2}$$

with ϵ_r the dielectric constant, and V_{ext} the external potential. If the Coulomb gauge $\nabla\cdot\mathbf{A}=0$ is chosen, from the Maxwell equation:

$$\nabla^2V=-4\pi\rho. \tag{2-3}$$

A solution to Eq. (2-3) is of the form

$$V(\mathbf{q},t)=\frac{2\pi}{|\mathbf{q}|}\rho(\mathbf{q},t). \tag{2-4}$$

where $V(\mathbf{q},t)$ and $\rho(\mathbf{q},t)$ are the Fourier transforms of $V(\mathbf{r},t)$ and $\rho(\mathbf{r},t)$, respectively, which are defined by:

$$f(\mathbf{r})=\frac{1}{2\pi}\int d\mathbf{q}f(\mathbf{q})e^{-i\mathbf{q}\cdot\mathbf{r}}; \tag{2-5}$$

$$f(\mathbf{q})=\frac{1}{2\pi}\int d\mathbf{r}f(\mathbf{r})e^{i\mathbf{q}\cdot\mathbf{r}}, \tag{2-6}$$

with Ω the volume of the first Brillouin zone. Eq. (2-2) implies the relation below:

$$\rho(\mathbf{q},t)=\frac{1}{\epsilon_r}\rho_{ext}(\mathbf{q},t). \tag{2-7}$$

In the absence of an external electric field, the expectation value of the density operator $\rho(\mathbf{q},t)$ should vanish everywhere except for the wave vector $\mathbf{q}$ = 0. When

an external potential is introduced, however, the average density will have a nonzero value due to the screening effect by the induced charges. The average induced charge density is proportional to the impurities:

$$\langle \rho_{ind}(\mathbf{q}, t) \rangle = -e \langle \rho(\mathbf{q}, t) \rangle. \tag{2-8}$$

We should point out that the charge density operator $\rho(\mathbf{r})$ discussed above is directly related to the particle density operator $n(\mathbf{r})$ by a factor of unit charge, *e*. *g*. – *e* in the case of electrons.

$$\rho(\mathbf{q}, t) = -en(\mathbf{q}, t). \tag{2-9}$$

The particle density operator $n(\mathbf{r})$ is defined by:

$$n(\mathbf{r}) = \sum_j \delta(\mathbf{r} - \mathbf{r}_j) = \psi^*(\mathbf{r})\psi(\mathbf{r}); \tag{2-10}$$

$$\psi(\mathbf{r}) = \sum_{\mathbf{k},\sigma,s} \varphi_{\mathbf{k},\sigma,s}(\mathbf{r}) c_{\mathbf{k},\sigma,s} e^{i\mathbf{k}\cdot\mathbf{r}}. \tag{2-11}$$

In the second quantization presentation:

$$n(\mathbf{q}) = \sum_{\mathbf{k},\sigma,s} (\varphi^{\dagger}_{\mathbf{k}+\mathbf{q},\sigma,s} \varphi_{\mathbf{k},\sigma,s}) c^{\dagger}_{\mathbf{k}+\mathbf{q},\sigma,s} c_{\mathbf{k},\sigma,s}. \tag{2-12}$$

The overlap is preserved since the states are distributed in distinct bands of the electronic structure in a solid. The potential energy of an electron in position **r** with potential $V(\mathbf{r})$ is defined by $U(\mathbf{r}) = -eV(\mathbf{r})$, in the momentum space:

$$U(\mathbf{q}) = -eV(\mathbf{q}). \tag{2-13}$$

Making use of all the equations presented above, the expression for dielectric constant comes to:

$$\frac{1}{\kappa_r(\mathbf{q}, t)} = 1 + V_q \frac{n_{ind}(\mathbf{q}, t)}{U_{ext}(\mathbf{q}, t)}. \tag{2-14}$$

Here $V_q = \frac{e^2}{2\kappa_s|q|}$is the Fourier transform of the Coulomb interaction for a 2D system. It is obvious that the inverse dielectric constant $\frac{1}{\kappa_r}$ describes the response to an external potential. The RPA polarization function is defined in Eq. (2-14) as:

$$P_{RPA}^{(1)}(\mathbf{q},t) = \frac{n_{ind}(\mathbf{q},t)}{U_{ext}(\mathbf{q},t)}. \tag{2-15}$$

If we replace $U_{ext}(\mathbf{q},t)$ with $\frac{1}{\kappa_r}U(\mathbf{q},t)$, we will reach an expression for the dielectric constant using a self-consistent process:

$$\kappa_r(\mathbf{q},t) = 1 - V_q\frac{n_{ind}(\mathbf{q},t)}{U(\mathbf{q},t)}. \tag{2-16}$$

κ_r describes the response to the total potential. The polarization function in this fashion is defined as:

$$P^{(1)}(\mathbf{q},t) = \frac{n_{ind}(\mathbf{q},t)}{U(\mathbf{q},t)}. \tag{2-17}$$

In order to calculate the dielectric function, we first use the Liouville–von-Neumann equation to calculate the particle density n_{ind}.

In the Born-Oppenheimer approximation, the Hamiltonian of the system is expressed as:

$$H = H_0 + U. \tag{2-18}$$

H_0 is the time independent unperturbed Hamiltonian with a solvable eigen-energy $\varepsilon_{\mathbf{k}}$, which, in the second quantization presentation, is:

$$H_0 = \sum_{\mathbf{k},\sigma,s}\varepsilon_{\mathbf{k},\sigma,s}c^{\dagger}_{\mathbf{k},\sigma,s}c_{\mathbf{k},\sigma,s}, \tag{2-19}$$

where U is the sum of the electron potential energy (Eq. (2-13)) over all the electrons, which is defined by

$$U = \frac{1}{v}\sum_{\mathbf{q}} U(\mathbf{q},t)\,\rho(\mathbf{q},t) = -\frac{e}{v}\sum_{\mathbf{q}} V(\mathbf{q},t)n(\mathbf{q},t). \tag{2-20}$$

The density operator $\rho(\mathbf{q},t)$ is a time dependent operator assuming to oscillate at a single frequency, which gives the time derivative a factor $-i\omega$. The equation of motion for single electron is:

$$\frac{i\hbar\partial\rho(\mathbf{q},t)}{\partial t} = [H,\rho(\mathbf{q},t)],$$

$$\frac{i\hbar\partial\rho(\mathbf{q},t)}{\partial t} = [H_0,\rho(\mathbf{q},t)] + [U,\rho(\mathbf{q},t)]. \tag{2-21}$$

Insert Eqs. (2-9), (2-19) and (2-20) into Eq. (2-21), and let $\hbar = 1$:

$$\omega n(\mathbf{q},t) = -\sum_{\mathbf{k},\mathbf{k}',\sigma,\sigma',s,s'}\left[\varepsilon_{\mathbf{k},\sigma,s}c^{\dagger}_{\mathbf{k},\sigma,s}\,c_{\mathbf{k},\sigma,s}\left(\varphi^{\dagger}_{\mathbf{k}'+\mathbf{q},\sigma',s'}\varphi_{\mathbf{k}',\sigma',s'}\right)c^{\dagger}_{\mathbf{k}'+\mathbf{q},\sigma',s'}c_{\mathbf{k}',\sigma',s'}\right]$$

$$-\frac{1}{v}U(\mathbf{q},t)\sum_{\mathbf{k},\mathbf{k}',\mathbf{q}',\sigma,\sigma',s,s'}[n(\mathbf{q}',t),n(\mathbf{q},t)\,].$$

After simplification:

$$\sum_{\mathbf{k},\sigma,s}\left(\varepsilon_{\mathbf{k},\sigma,s}-\varepsilon_{+\mathbf{q},\sigma,s}+\omega\right)\left(\varphi^{\dagger}_{\mathbf{k}+\mathbf{q},\sigma,s}\varphi_{\mathbf{k},\sigma,s}\right)c^{\dagger}_{\mathbf{k}+\mathbf{q},\sigma,s}c_{\mathbf{k},\sigma,s}$$

$$=\frac{1}{v}U(\mathbf{q},t)\sum_{\mathbf{k},\mathbf{q}',\sigma,\sigma',s,s'}\left|\left\langle\varphi_{\mathbf{k}+\mathbf{q},\sigma',s'}\middle|\varphi_{\mathbf{k},\sigma,s}\right\rangle\right|^2\left(c^{\dagger}_{\mathbf{k}+\mathbf{q}+\mathbf{q}',\sigma,s}c_{\mathbf{k},\sigma,s}\right.$$

$$\left.-\,c^{\dagger}_{\mathbf{k}-\mathbf{q}',\sigma',s'}c_{\mathbf{k}+\mathbf{q},\sigma',s'}\right).$$

In the RPA, another assumption is that the total electric potential averages out, so that only the term q' =-q contributes. Thus:

$$\sum_{\mathbf{k},\sigma,s}\left(\varepsilon_{\mathbf{k},\sigma,s}-\varepsilon_{+\mathbf{q},\sigma,s}+\omega\right)\left(\varphi^{\dagger}_{\mathbf{k}+\mathbf{q},\sigma,s}\varphi_{\mathbf{k},\sigma,s}\right)c^{\dagger}_{\mathbf{k}+\mathbf{q},\sigma,s}c_{\mathbf{k},\sigma,s}$$

$$\approx \frac{U(\mathbf{q},t)}{v}\sum_{\mathbf{k},\mathbf{q}',\sigma,\sigma',s,s'} F_{\sigma'\sigma,ss'}(\mathbf{k}+\mathbf{q},\mathbf{k})\left(c^{\dagger}_{\mathbf{k},\sigma,s}c_{\mathbf{k},\sigma,s}\right.$$

$$\left.-\,c^{\dagger}_{\mathbf{k}+\mathbf{q},\sigma',s'}c_{\mathbf{k}+\mathbf{q},\sigma',s'}\right),$$

with $F_{\sigma'\sigma,ss'}(\mathbf{k}+\mathbf{q},\mathbf{k})$ the overlap factor:

$$F_{\sigma'\sigma,ss'}(\mathbf{k}+\mathbf{q},\mathbf{k}) = \left|\left\langle\varphi_{\mathbf{k}+\mathbf{q},\sigma',s'}\middle|\varphi_{\mathbf{k},\sigma,s}\right\rangle\right|^2. \tag{2-22}$$

Now we arrive at:

$$\rho(\mathbf{q},t) = \frac{U(\mathbf{q},t)}{v}\sum_{\mathbf{k},\sigma,\sigma',s,s'} F_{\sigma'\sigma,ss'}(\mathbf{k}$$

$$+\mathbf{q},\mathbf{k})\frac{\left(c^{\dagger}_{\mathbf{k},\sigma,s}c_{\mathbf{k},\sigma,s}-c^{\dagger}_{\mathbf{k}+\mathbf{q},\sigma',s'}c_{\mathbf{k}+\mathbf{q},\sigma',s'}\right)}{\varepsilon_{\mathbf{k},\sigma,s}-\varepsilon_{\mathbf{k}+\mathbf{q},\sigma',s'}+\omega}. \tag{2-23}$$

Take the average on each side. Here, we should introduce the third assumption of the RPA that the external potential oscillates at a single frequency. Therefore, the time-dependent charge density operator and electron potential energy are determined by frequency only. The expectation values of $\langle\rho(\mathbf{q},t)\rangle$ and $\langle U(\mathbf{q},t)\rangle$ are replaced by $\rho(\mathbf{q},\omega)e^{-i\omega t}$ and $U(\mathbf{q},\omega)e^{-i\omega t}$, respectively. The number operator gives rise to the Fermi-Dirac distribution function:

$$f_{\mathbf{k},\sigma,s} = c^{\dagger}_{\mathbf{k},\sigma,s}c_{\mathbf{k},\sigma,s}. \tag{2-24}$$

Thus the final result as a function of momentum $\mathbf{q}$ and ω is:

$$\rho(\mathbf{q},\omega) = \frac{U(\mathbf{q},\omega)}{v}\sum_{\mathbf{k},\sigma,\sigma',s,s'} F_{\sigma'\sigma,ss'}(\mathbf{k}$$

$$+\mathbf{q},\mathbf{k})\frac{\left(f_{\mathbf{k},\sigma,s}-f_{\mathbf{k}+\mathbf{q},\sigma',s'}\right)}{\varepsilon_{\mathbf{k},\sigma,s}-\varepsilon_{\mathbf{k}+\mathbf{q},\sigma',s'}+\omega}. \tag{2-25}$$

Using Eq. (2-8), and moving the $U(\mathbf{q},t)$ to the left side:

$$P^{(1)}(\mathbf{q},\omega)=\frac{\rho(\mathbf{q},\omega)}{U(\mathbf{q},\omega)}$$

$$=\frac{1}{v}\sum_{\mathbf{k},\sigma,\sigma',s,s'}F_{\sigma'\sigma,ss'}(\mathbf{k}+\mathbf{q},\mathbf{k})\frac{\left(f_{\mathbf{k},\sigma,s}-f_{\mathbf{k}+\mathbf{q},\sigma',s'}\right)}{\varepsilon_{\mathbf{k},\sigma,s}-\varepsilon_{\mathbf{k}+\mathbf{q},\sigma',s'}+\omega}, \tag{2-26}$$

which relate to the RPA polarization function:

$$P^{(1)}_{RPA}(\mathbf{q},t)=\frac{P^{(1)}(\mathbf{q},t)}{1-V_qP^{(1)}(\mathbf{q},t)}. \tag{2-27}$$

Thus the dielectric function in the frequency domain is:

$$\epsilon(q,t)=1-V_qP^{(1)}(\mathbf{q},t). \tag{2-28}$$

The effective screening potential is no longer the Coulomb potential as describe above and is given by:

$$V_{eff}=\frac{V_q}{1-V_qP^{(1)}(\mathbf{q},\omega)}. \tag{2-29}$$

2.2 Dielectric function for HgTe/CdTe quantum wells

2.2.1 Bernevig-Hughes-Zhang (BHZ) model

The Hamiltonian of an HgTe/CdTe QW is given by Eq. (1-1), and the bulk state energy spectrum is given by Eq. (1-4):

$$\varepsilon_s(\mathbf{k})=-Dk^2+s\sqrt{(M-Bk^2)^2+A^2k^2},$$

with $s=\pm1$ representing the conduction and valence band, respectively. The band structure is plotted in Figure 2-1, where the bulk gap is 20 meV as labelled, and the Fermi level is shown as lying at 50 meV as an example.

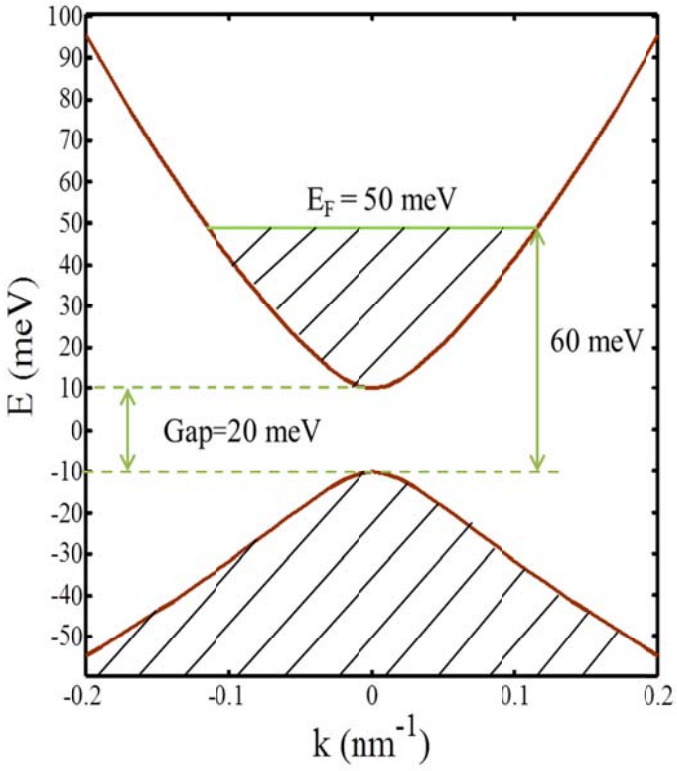

Figure 2-1. Band structure of HgTe/CdTe QWs with the **F**ermi energy level lying at 50 meV.

The wave function for the bulk state has the form of:

$$\psi_s(\mathbf{r}) = \varphi(\mathbf{k})e^{i\mathbf{k}\cdot\mathbf{r}} = \frac{1}{\sqrt{C_s^2(\mathbf{k})+1}}\begin{pmatrix}1\\ C_s(\mathbf{k})e^{-i\theta_{\mathbf{k}}}\end{pmatrix}e^{i\mathbf{k}\cdot\mathbf{r}}, \qquad (2\text{-}30)$$

$$C_s(\mathbf{k}) = \varepsilon_s(\mathbf{k}) - M + B_+k^2;$$

$$\theta_{\mathbf{k}} = \arctan\frac{k_y}{k_x};$$

$$B_+ = B + D.$$

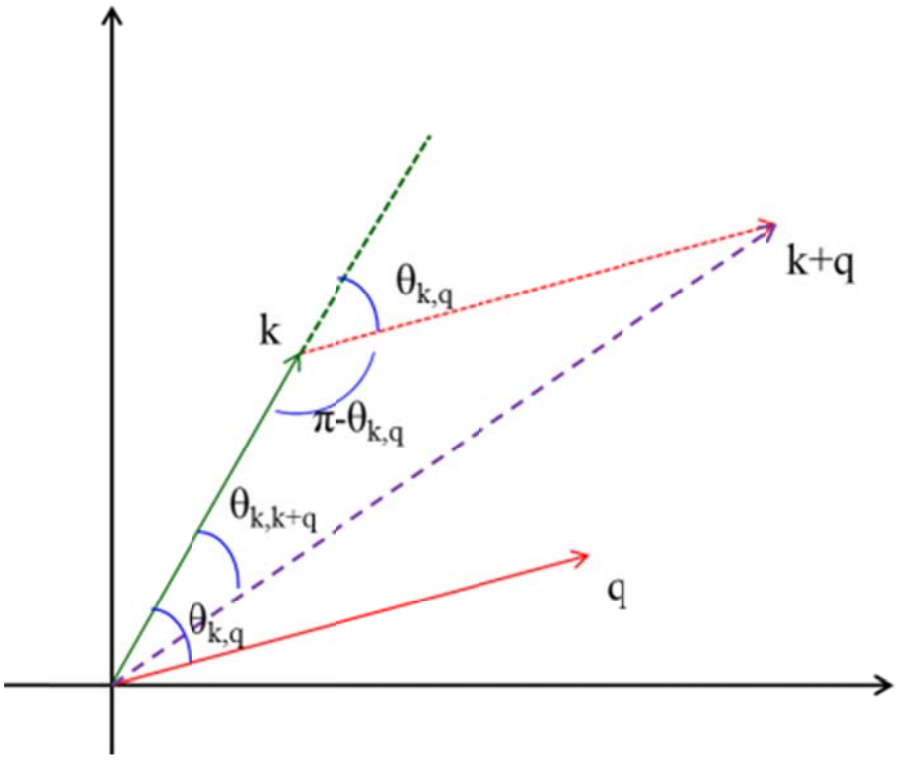

Figure 2-2 Azimuthal angle scheme for wave vectors **k** and **q**.

2.2.2 Dielectric function of HgTe/CdTe quantum wells

In order to calculate the dielectric function of HgTe/CdTe QWs, we first proceed to calculate the overlap factor in Eq. (2-22). The overlap between two states is evaluated by:

$$\langle \varphi(\mathbf{k}+\mathbf{q})|\varphi(\mathbf{k})\rangle$$

$$= \frac{1}{\sqrt{C_s^2(\mathbf{k}+\mathbf{q})+1}\sqrt{C_s^2(\mathbf{k})+1}}\begin{pmatrix}1 & C_s(\mathbf{k})e^{i\theta_{\mathbf{k}+\mathbf{q}}}\end{pmatrix}\begin{pmatrix}1\\ C_s(\mathbf{k})e^{-i\theta_{\mathbf{k}}}\end{pmatrix}e^{-i\mathbf{q}\cdot\mathbf{r}}$$

$$= \frac{1}{\sqrt{C_s^2(\mathbf{k}+\mathbf{q})+1}\sqrt{C_s^2(\mathbf{k})+1}}e^{-i\mathbf{q}\cdot\mathbf{r}}\left[1+C_s(\mathbf{k}+\mathbf{q})C_s(\mathbf{k})e^{i}\left(\theta_{\mathbf{k}+\mathbf{q}}-\theta_{\mathbf{k}}\right)\right]. \quad (2\text{-}31)$$

The overlap factor becomes:

$$F^{ss'}(\mathbf{k}+\mathbf{q},\mathbf{k}) = |\langle\varphi(\mathbf{k}+\mathbf{q})|\varphi(\mathbf{k})\rangle|^2$$

$$= \frac{\left[1+C_s(\mathbf{k}+\mathbf{q})C_s(\mathbf{k})e^{-i(\theta_{\mathbf{k}+\mathbf{q}}-\theta_{\mathbf{k}})}\right]\left[1+C_s(\mathbf{k}+\mathbf{q})C_s(\mathbf{k})e^{i(\theta_{\mathbf{k}+\mathbf{q}}-\theta_{\mathbf{k}})}\right]}{(C_s^2(\mathbf{k}+\mathbf{q})+1)(C_s^2(\mathbf{k})+1)}$$

$$= \frac{\left[1+C_s(\mathbf{k}+\mathbf{q})C_s(\mathbf{k})\cos\left(\theta_{\mathbf{k}+\mathbf{q}}-\theta_{\mathbf{k}}\right)+C_s^2(\mathbf{k}+\mathbf{q})C_s^2(\mathbf{k})\right]}{(C_s^2(\mathbf{k}+\mathbf{q})+1)(C_s^2(\mathbf{k})+1)}. \quad (2\text{-}32)$$

Let $\theta_{\mathbf{k}+\mathbf{q},\mathbf{k}} = \theta_{\mathbf{k}+\mathbf{q}} - \theta_{\mathbf{k}}$. The cosine term written as $\cos\theta_{\mathbf{k}+\mathbf{q},\mathbf{k}}$ can be evaluated using the cosine rule, which is shown in Figure 2-2, where $\theta_{\mathbf{k},\mathbf{q}} = \theta_{\mathbf{q}} - \theta_{\mathbf{k}}$. Now the cosine term arrives at:

$$\cos\theta_{\mathbf{k}+\mathbf{q},\mathbf{k}} = \frac{k+q\cos\theta_{\mathbf{k},\mathbf{q}}}{\sqrt{k^2+q^2+2kq\cos\theta_{\mathbf{k},\mathbf{q}}}}. \quad (2\text{-}33)$$

In the system of the HgTe/CdTe QW, the polarization function $\Pi(\mathbf{q},i\omega_n)$ is written as the integral of the momentum k.

$$\Pi(\mathbf{q},i\omega_n) = \lim_{\Omega\to\infty}\frac{1}{\Omega}\sum_{\mathbf{k},s,s'}F^{ss'}(\mathbf{k}+\mathbf{q},\mathbf{k})\frac{f_{\mathbf{k}+\mathbf{q},s'}-f_{\mathbf{k},s}}{\varepsilon_{\mathbf{k}+\mathbf{q},s'}-\varepsilon_{\mathbf{k},s}-i\omega_n}$$

$$= \sum_{s,s'}\int\frac{d\mathbf{k}}{(2\pi)^2}F^{ss'}(\mathbf{k}+\mathbf{q},\mathbf{k})\frac{f_{\mathbf{k}+\mathbf{q},s'}-f_{\mathbf{k},s}}{\varepsilon_{\mathbf{k}+\mathbf{q},s'}-\varepsilon_{\mathbf{k},s}-i\omega_n}, \quad (2\text{-}34)$$

or:

$$\Pi(\mathbf{q},i\omega_n) = -\sum_{s,s'}\int\frac{d\mathbf{k}}{(2\pi)^2}F^{ss'}(\mathbf{k}+\mathbf{q},\mathbf{k}) \times\left(\frac{f_{\mathbf{k},s'}}{\varepsilon_{\mathbf{k}+\mathbf{q},s}-\varepsilon_{\mathbf{k},s'}+i\omega_n}+\frac{f_{\mathbf{k},s}}{\varepsilon_{\mathbf{k}+\mathbf{q},s'}-\varepsilon_{\mathbf{k},s}-i\omega_n}\right), \quad (2\text{-}35)$$

with the Fermi-Dirac distribution function:

$$f_{\mathbf{k},s} = \frac{1}{e^{\beta(\varepsilon_{\mathbf{k},s}-\mu)}+1}, \quad (2\text{-}36)$$

where $\beta=1/k_BT$, with k_B the Boltzmann constant.

To evaluate the Eq. (2-34), we apply the analytic continuation step: $i\omega_n \rightarrow \omega + i\delta$, which create a retarded function. δ is an infinitesimal. Then, we use the identity:

$$\frac{1}{f(x) \pm i(\delta \rightarrow 0)} = P\frac{1}{f(x)} \mp i\pi\delta\big(f(x)\big). \tag{2-37}$$

The imaginary part of the result will be:

$$Im\Pi(\mathbf{q},\omega) = \pi \sum_{s,s'} \int \frac{d\mathbf{k}}{(2\pi)^2} F^{ss'}(\mathbf{k}+\mathbf{q},\mathbf{k}) \times \big(f_{\mathbf{k}+\mathbf{q},s'} - f_{\mathbf{k},s}\big)\delta\big(\varepsilon_{\mathbf{k}+\mathbf{q},s'} - \varepsilon_{\mathbf{k},s} - \omega\big). \tag{2-38}$$

It is very straightforward to do the delta function, and the double integration is reduced to a single integration. The identity $\Pi(q,\omega) = \Pi^*(q,-\omega)$ can be easily proved by rearranging the **k** summation in Eq. (2-34); the real part of $P^{(1)}(\mathrm{q},\omega)$ is an even function of ω, while the imaginary part of $\Pi(q,\omega)$ is odd function of $\Pi(q,\omega)$. Thus, the real part can be calculated using Kramers-Kronig relation:

$$Re\Pi(\mathbf{q},\omega) = \frac{2}{\pi} P \int_0^\infty \frac{\omega' ImP^{(1)}(\mathbf{q},\omega')}{\omega'^2 - \omega^2} d\omega'. \tag{2-39}$$

P on the right hand side of the equation denotes Cauchy principal value. With the delta function, the real part of the polarization function becomes:

$$Re\Pi(\mathbf{q},\omega) = \sum_{s,s'} \int \frac{d\mathbf{k}}{(2\pi)^2} \times F^{ss'}(\mathbf{k}+\mathbf{q},\mathbf{k}) \frac{\big(f_{\mathbf{k}+\mathbf{q},s'} - f_{\mathbf{k},s}\big)\big(\varepsilon_{\mathbf{k}+\mathbf{q},s'} - \varepsilon_{\mathbf{k},s}\big)}{\big(\varepsilon_{\mathbf{k}+\mathbf{q},s'} - \varepsilon_{\mathbf{k},s}\big)^2 - \omega^2}. \tag{2-40}$$

For the long wavelength limit ($q \rightarrow 0$), Eq. (2-35) is expanded in terms of q:

$$\Pi(\mathrm{q}, i\omega_n) = -\int \frac{d\mathbf{k}}{(2\pi)^2} f_{\mathbf{k},+} \Big(\frac{1}{v_+(k) q\cos\theta + i\omega_n} + \frac{1}{v_+(k)\, q\cos\theta - i\omega_n} \Big)$$

$$+\int \frac{d\mathbf{k}}{(2\pi)^2} F^{\mp}(\mathbf{k}+\mathbf{q},\mathbf{k})\left(f_{\mathbf{k}+\mathbf{q},+}-1\right)\frac{1}{\varepsilon_{\mathbf{k},+}-\varepsilon_{\mathbf{k},-}-i\omega_n}. \tag{2-41}$$

Here, $v_s(k)$ is the velocity as a function of k:

$$v_s(k) = \left(-2D + R_{k,s}\right)k, \tag{2-42}$$

$$R_{k,s} = \frac{(A^2 - 2BM) - 2Bk^2}{s\sqrt{A^2k^2 + (M - Bk^2)^2}}. \tag{2-43}$$

The first term in Eq. (2-41) corresponds to the intraband polarization, which vanishes in the long wavelength limit; the second term is ascribed to the interband. Under this condition, the imaginary part is:

$$Im\Pi(q \to 0, i\omega_n) = \frac{2\tilde{k}}{\pi^2}\frac{(A^2 - 2BM) + 2B\tilde{k}^2}{\omega}\int_0^{\pi} d\theta F^{\mp}(\theta)\left(f_{\theta,+}-1\right),$$

$$\tilde{k} = \left(\frac{-(A^2 - 2BM) + \sqrt{(A^2 - 2BM)^2 - B^2(4M^2 - \omega^2)}}{2B^2}\right)^{\frac{1}{2}} \leq k_F. \tag{2-44}$$

The real part is:

$$Re\Pi(q \to 0, i\omega_n) = \frac{1}{8\pi^2}\int d\mathbf{k}\left(F^{\mp}(\mathbf{k}+\mathbf{q},\mathbf{k})\frac{\left(f_{k,+}-1\right)}{\sqrt{A^2k^2 + (M - Bk^2)^2} - \omega}\right). \tag{2-45}$$

When ω = 0, the imaginary part of the polarization function becomes zero, the real part of the polarization gives the static screening.

Imaginary part of the dielectric function:

The delta function in Eq. (2-38) has the identity:

$$\delta\left(\varepsilon_{\mathbf{k}+\mathbf{q},s'} - \varepsilon_{\mathbf{k},s} - \omega\right) = \frac{\delta\left(\theta_{\mathbf{k},\mathbf{q}} - \theta^0_{\mathbf{k},\mathbf{q}}\right)}{\left|\frac{\partial\left(\varepsilon_{\mathbf{k}+\mathbf{q},s'} - \varepsilon_{\mathbf{k},s} - \omega\right)}{\partial\theta}\right|_{\theta_{\mathbf{k},\mathbf{q}}=\theta^0_{\mathbf{k},\mathbf{q}}}}$$

$$= \frac{\delta\left(\theta_{\mathbf{k},\mathbf{q}} - \theta^0_{\mathbf{k},\mathbf{q}}\right)}{\left|\frac{\partial \varepsilon_{\mathbf{k}+\mathbf{q},s'}}{\partial\theta}\right|_{\theta_{\mathbf{k},\mathbf{q}}=\theta^0_{\mathbf{k},\mathbf{q}}}}, \tag{2-46}$$

where the derivative in the denominator is:

$$\frac{\partial \varepsilon_{\mathbf{k}+\mathbf{q},s'}}{\partial\theta} = kq\sin\theta_{\mathbf{k},\mathbf{q}}\left[2D + s'\frac{(2BM - A^2) - 2B^2|\mathbf{k}+\mathbf{q}|^2}{\sqrt{[M - B|\mathbf{k}+\mathbf{q}|^2]^2 + A^2|\mathbf{k}+\mathbf{q}|^2}}\right],$$

$$\sin\theta_{\mathbf{k},\mathbf{q}} = \sqrt{1 - \cos^2\theta_{\mathbf{k},\mathbf{q}}}.$$

$\theta^0_{\mathbf{k},\mathbf{q}}$ can be obtained by solving the delta function:

$$\varepsilon_{\mathbf{k}+\mathbf{q},s'}\left(\theta_{\mathbf{k},\mathbf{q}}\right) - \varepsilon_{\mathbf{k},s} - \omega = 0.$$

Finally the integral becomes 1D:

$$Im\Pi(q,\omega)$$

$$= \frac{1}{4\pi}\sum_{s,s'}\int_0^\infty dk\, F^{ss'}(\mathbf{k}+\mathbf{q},\mathbf{k})$$

$$\times \frac{\left(f_{\mathbf{k}+\mathbf{q},s'} - f_{\mathbf{k},s}\right)}{\left|kq\sin\theta_{\mathbf{k},\mathbf{q}}\left[2D + s'\frac{(2BM - A^2) - 2B^2|\mathbf{k}+\mathbf{q}|^2}{\sqrt{[M - B|\mathbf{k}+\mathbf{q}|^2]^2 + A^2|\mathbf{k}+\mathbf{q}|^2}}\right]\right|}\Bigg|_{\theta_{\mathbf{k},\mathbf{q}}=\theta^0_{\mathbf{k},\mathbf{q}}}. \tag{2-47}$$

The imaginary part of the dielectric function is:

$$\kappa(q,\omega) = -V_q Im\Pi(q,\omega). \tag{2-48}$$

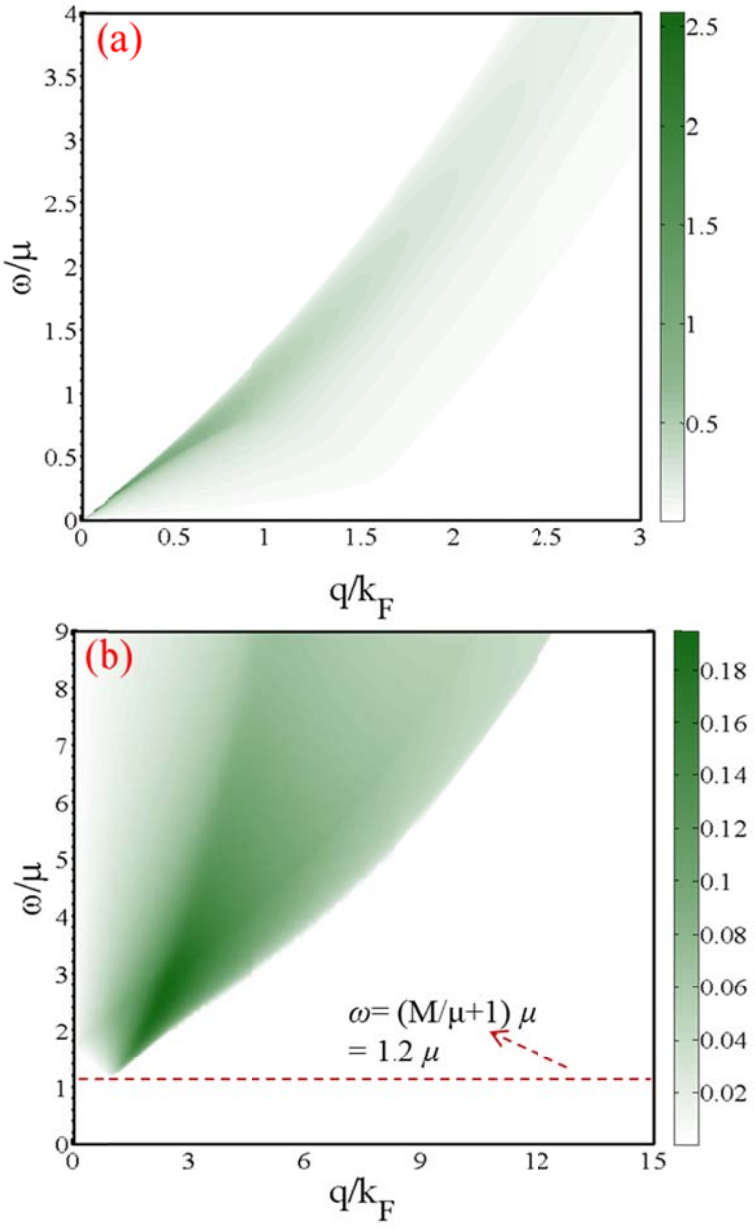

Figure 2-3. Dielectric function of HgTe/CdTe QWs as a function of ω (in units of μ) and q (in units of k_F) at zero temperature; μ is the chemical potential, which is 50 meV. (a) The dielectric function contribution from intraband excitations; (b) the dielectric function contributed from interband excitations. The red line indicates that the minimum interband excitation frequency ω is above 1.2 μ.

The imaginary part of dielectric function as a function of momentum and frequency at zero temperature is plotted in Figure 2-3, where (a) is contributed by the intraband excitations and (b) by interband. The Fermi energy is set to 50 meV for numerical calculation. At zero temperature, the intraband excitations mainly occur in the low frequency regime due to the reduced phase space at higher energy levels. On the other hand, there are no interband excitations allowed at the regime where the frequency is lower than 1.2 μ, as indicated by the red line. Moreover, we can see that momentum transfer q is monotonically related to the excitation frequency ω, as restricted by the energy conservation law.

In Figure 2-4, we present the frequency dependent imaginary part of the polarization function at temperatures ranging from 0 K to 300 K. The peak positions of the polarization function clearly shift to higher frequency with increasing temperature, especially at small chemical potentials. At non-zero temperature, electrons could be thermally excited to above the Fermi level; the higher the temperature that the system reaches, the more electrons hop up to the excited states. Therefore, the redistribution of the electronic structure at high temperature takes over partially filled states at higher levels, which require stronger energy for excitation. For the cases with high chemical potential, *e.g.*, Figure 2-4(c), however, the temperature has less thermal effect on the electrons. This is because at the high energy level, the density of states decreases significantly, and the redistribution of the electronic structure is less affected by the thermal excitation at room temperature.

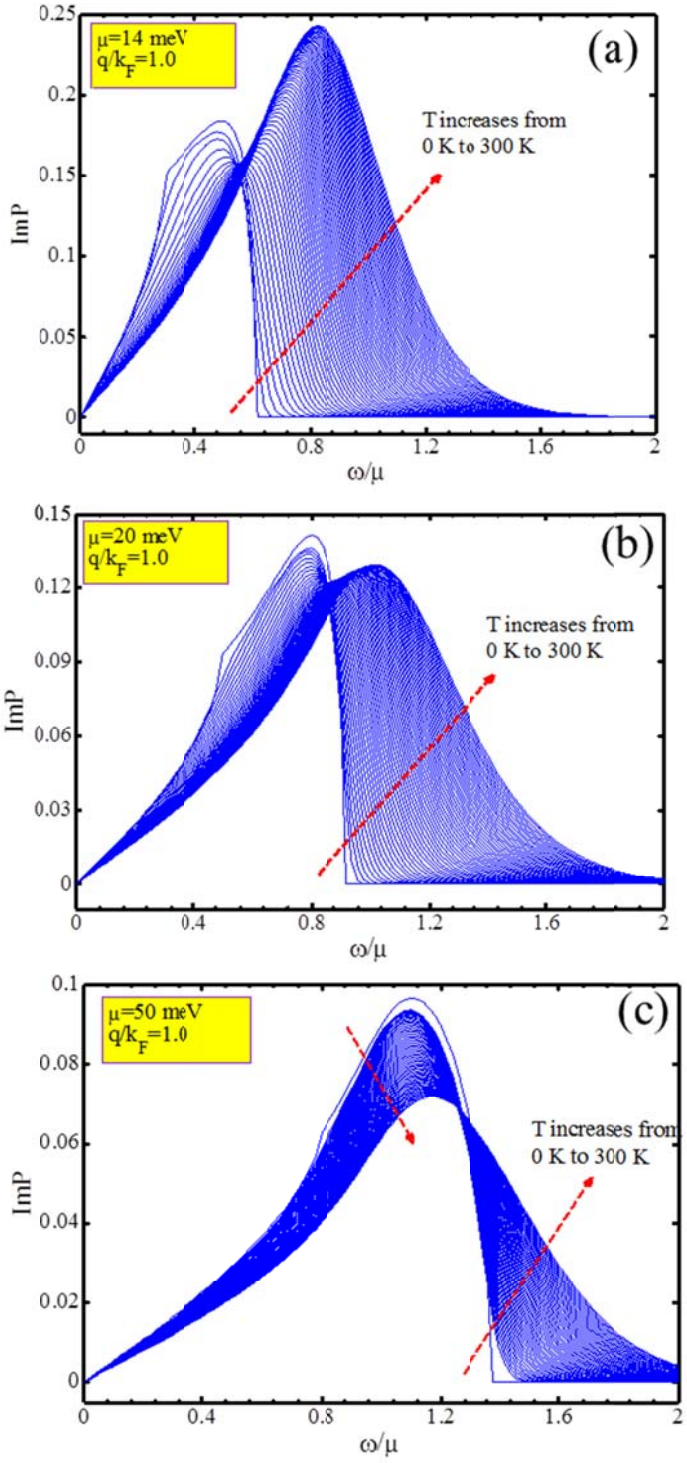

Figure 2-4. Imaginary part of the polarization function versus frequency at different temperature, and different chemical potentials (a) 10 meV, (b) 20 meV, (c) 50 meV.

Real part of the dielectric function.

While the real part in Eq. (2-40) is treated as:

$$Re\Pi(\mathbf{q},\omega) = \frac{1}{4\pi^2}\sum_{s,s'}\int_0^{\infty} kdk \int_0^{2\pi} d\theta \times F^{ss'}(\mathbf{k}+\mathbf{q},\mathbf{k})\frac{(\varepsilon_{\mathbf{k}+\mathbf{q},s'} - \varepsilon_{\mathbf{k},s} - \omega)(f_{\mathbf{k}+\mathbf{q},s'} - f_{\mathbf{k},s})}{(\varepsilon_{\mathbf{k}+\mathbf{q},s'} - \varepsilon_{\mathbf{k},s} - \omega)^2 + \delta^2} \quad (2\text{-}49)$$

δ is taken as 0.01 for small frequency, and 0.1 ω for high frequency.

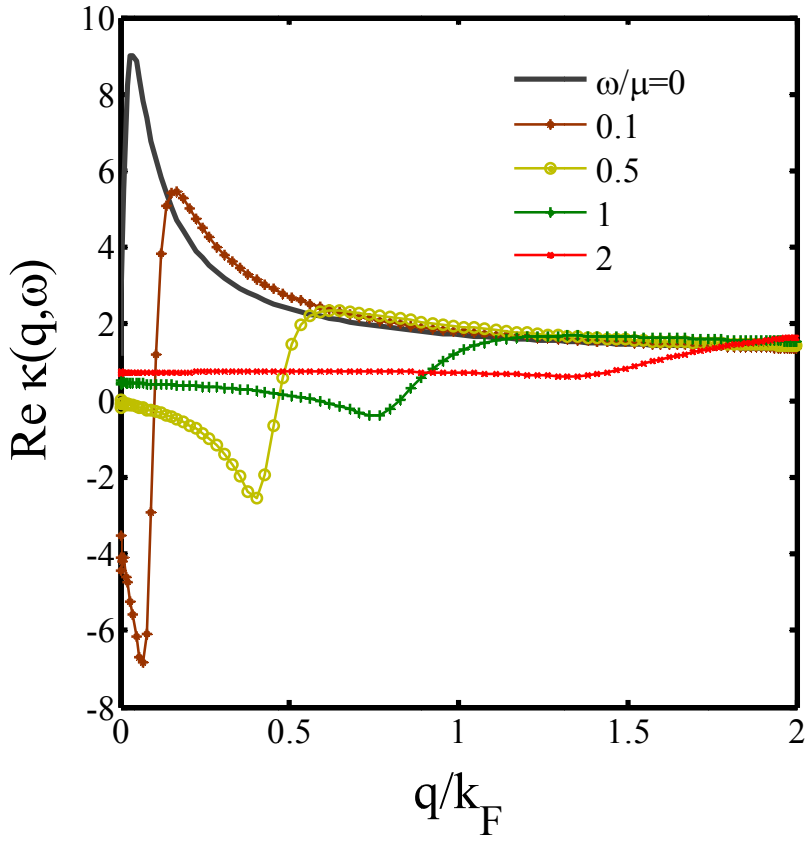

Figure 2-5. Real part of the dielectric function versus momentum q at various frequencies. The chemical potential μ = 50 meV.

The real part of dielectric function is plotted in Figure 2-5. The case ω = 0 with arbitrary q is relevant for the static screening of charged impurities, which is positive

and has a strong screening effect within $q < k_F$. The dynamic screening effect has a sign flip with respect to the frequency and decreases with increasing frequency.

2.2.3 Plasmon

The plasmon mode can be obtained by looking for the poles of the density correlation function, or equivalently, by solving for $\kappa(q, \omega) = 0$. The plasmon dispersion is shown in Figure 2-6, where the yellow area stands for the electron-hole continuum or single-particle excitation (SPE). The SPE continuum is defined by the nonzero value of the imaginary part of the polarizability, $\mathrm{Im}\kappa(q, \omega) \neq 0$. From the SPE map in ($q$, ω) space in Figure 2-6, we find that in our non-parabolic 2D systems, both intraband and interband transitions are possible, but the direct transition (q = 0) is forbidden, which is very different from that of 2D graphene and normal 2D system with parabolic energy dispersion.[151-154] It is known that the plasmon mode is damped when lying inside the SPE continuum, because the collective mode decays to electron-hole pair. For a normal 2D system with parabolic energy dispersion, the plasmon mode survives at long wavelengths, and only enters the SPE continuum at a critical wave vector and, therefore, does not exist at very high wave vectors;[152] while in 2D graphene, the plasmon mode does not enter into the intraband SPE for all wave vectors, but decays into the real interband electron-hole pairs in the interband SPE regime at higher wave vectors,[152] since interband transitions are regarded as the main decay channel for plasmon modes[155]. However, in our 2D system with non-parabolic energy dispersion, the collective mode enters both inter- and intraband SPE continuum. The phenomenon that all spectral weight of the plasmon mode is

transferred to the SPE indicates relative high absorption under an external electric field.

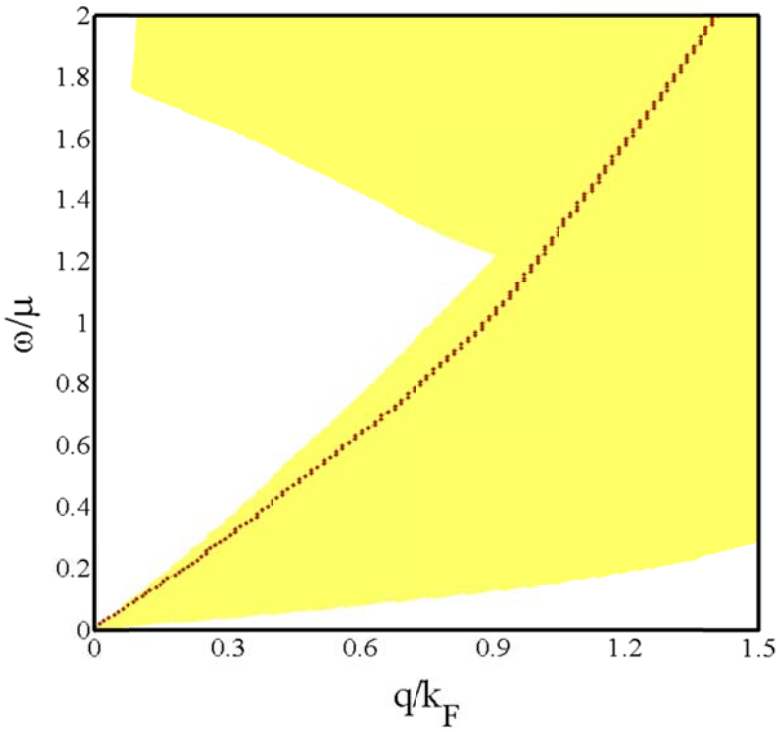

Figure 2-6. Plasmon dispersion relation. The yellow area shows the non-zero imaginary part of dielectric function.

In summary, we have briefly reviewed the dielectric function in RPA fashion. We also calculated the real part and imaginary part of dielectric function of HgTe/CdTe QWs as a function of frequency. We find that the thermal effect has significant impact on the dielectric function of HgTe/CdTe QWs, which is different from that of graphene.The plasmon dispersion relation is damped even in the intraband SPE due to the relative high absorption under an external electric field.

CHAPTER 3 ENERGY LOSS RATE OF A CHARGED PARTICLE IN HGTE/CDTE QUANTUM WELLS

Electron energy loss spectroscopy (EELS) has been a very useful probe of materials properties. In EELS, the interaction between a charged external particle and an electronic system has been employed to reveal electron excitations in condensed matter physics and nuclear physics.[156-159] The scattering cross section of an external particle by an electronic system can be directly related to the density-density correlation function, the screening properties and the inter-particle coupling. In moving through an electronic system, the charged particle experiences both momentum and energy loss due to the nature of the inelastic scattering. For *n*-type HgTe/CdTe QWs, 2DEG is confined in the "well" with a gap in the bulk states related to the well thickness. The scattering of an external charged particle in the system can involve both the gapless edge states as well as the gapped bulk states.

In this Chapter, we focus on the scattering behaviour accounting for the gapped bulk states of HgTe/CdTe QWs, as the scattering on the 1D edge could be neglected when the chemical potential lies in the valence band.

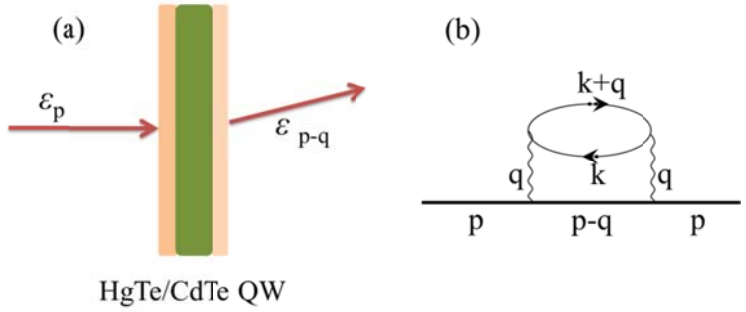

figure 3-1 (a) A charged particle traverses a HgTe/CdTe QW with energy loss of $\omega = \varepsilon_{\mathbf{p}} - \varepsilon_{\mathbf{p-q}}$, and direction change due to the inelastic scattering; (b) Feynman diagram in the self-energy of the charged particle given by the solid line. The wavy line stands for the screened Coulomb potential.

3.1 Formalism

In this chapter, we study the energy loss rate of an external electron in the *n*-type HgTe/(Cd, Hg)Te QWs. As indicated in figure 3-1(a) and (b), we consider a process of an incoming particle of momentum $\mathbf{p}$ and energy $\varepsilon_{\mathbf{p}} = \hbar^2\boldsymbol{p}^2/2m$, interacting with the HgTe/(Cd, Hg)Te QW through a screened Coulomb interaction $g_{\mathbf{q}}$. The momentum transfer and the energy loss in a scattering are $\mathbf{q}$ and $\omega = \varepsilon_{\mathbf{p}} - \varepsilon_{\mathbf{p-q}}$, $(\hbar = 1)$. The energy loss rate of a particle in a two dimensional system is typically defined as:

$$\frac{dE_{\mathbf{p}}}{dt} = \int \frac{d\mathbf{q}}{(2\pi)^2} W(\mathbf{q}, \omega)\left(E_{\mathbf{p}} - E_{\mathbf{p-q}}\right). \tag{3-1}$$

$W(\mathbf{q}, \omega)$ is the transition probability which can be calculated from Fermi's golden rule. The transition probability between two states is defined by:

$$W_{if} = \frac{2\pi}{\hbar}\left|H'_{ij}\right|^2 \rho_f, \tag{3-2}$$

with

$$\left|H'_{ij}\right|^2 = |\langle f|H'|i\rangle|^2. \tag{3-3}$$

H' represents the time independent potential of the 2DEG in the HgTe/CdTe well, and *i* and *f* in subscript denote the initial state and the final state respectively. The transition probability describes the transition rate from the *f* state to the *i* state in the system with constant potential during a period of time. ρ_f is the density operator of the final states. We assume that each transition happens in the single-state only, and ρ_f can be written as a delta function corresponding to the frequency of the incoming electron. The delta function explains the energy conservation in each transition. Thus, the probability at which the electrons are making transitions is expressed as:

$$\begin{aligned} W_{if} &= \frac{2\pi}{\hbar\Omega^2}\sum_{\mathbf{k},s,s'}\left|\langle\varphi_{\mathbf{k}',s'}\left|V_{\mathbf{q}}\rho(\mathbf{q})e^{-i\mathbf{q}\cdot\mathbf{r}}\right|\varphi_{\mathbf{k},s}\rangle\right|^2 \delta\big(E_{\mathbf{k},s} - E_{\mathbf{k}+\mathbf{q},s'} \\ &\quad + \hbar\omega\,\big)\big(f_{\mathbf{k},s} - f_{\mathbf{k}+\mathbf{q},s'}\big) \\ &= \frac{2\pi}{\hbar\Omega^2}\left|V_{\mathbf{q}}\right|^2\sum_{\mathbf{k},s,s'}\left|\langle\varphi_{\mathbf{k}+\mathbf{q},s'}\left|\rho(\mathbf{q})\right|\varphi_{\mathbf{k},s}\rangle\right|^2\big(f_{\mathbf{k},s} - f_{\mathbf{k}+\mathbf{q},s'}\big)\delta\big(E_{\mathbf{k},s} \\ &\quad - E_{\mathbf{k}+\mathbf{q},s'} + \hbar\omega\,\big), \end{aligned} \tag{3-4}$$

where Ω is the volume of the Brillouin zone. The difference in the Fermi-Dirac function implies the net transition from state **k** to the state **k**+**q**. The imaginary part of the inverse dielectric function in the linear screening theory is given by[148]:

$$Im\left[\frac{1}{\kappa(\mathbf{q},\omega)}\right] = \frac{\pi}{\Omega}\big(1 - e^{-\beta\omega}\big)\sum_{m,n}\left|\langle m|\rho(\mathbf{q})|n\rangle\right|^2 \delta(E_n - E_m + \hbar\omega\,). \tag{3-5}$$

Comparing Eq. (3-4) with Eq. (3-5), the transition probability has the form:

$$W(\mathbf{q},\omega)=\frac{2}{\hbar\Omega}\frac{V_{\mathbf{q}}^{S}}{1-e^{-\beta\omega}}Im\left[\frac{1}{\kappa(\mathbf{q},\omega)}\right]. \tag{3-6}$$

$V_{\mathbf{q}}^{S}$ is the screened Coulomb potential coupling the interaction between the incident electron and 2D electrons gas in the "well". $V_{\mathbf{q}}^{S}$, for simplicity, has of the form from the 2D system[160]:

$$V_{\mathbf{q}}^{S}=\frac{1}{q+q_s}. \tag{3-7}$$

Here, q_s is the screening wavenumber,

$$q_s=\frac{m^*e}{2\pi\hbar^2\kappa_s}\left(1-e^{-\frac{\hbar^2\beta\pi n}{m^*}}\right)m, \tag{3-8}$$

where m^* is the effective mass of the electron, and n is the carrier density of the HgTe/CdTe QW, which is self-consistent with chemical potential, and κ_s is the static electric constant of the material. In the above expression, we have only included the scattering by the particle-hole excitation, assuming that the plasmon of the gapless states is heavily damped (see Figure 2-6) and that the inter-band plasmon is at a much higher energy. The dynamical polarization function in the random-phase-approximation is Eq. (2-34).

In the following, we shall use the static approximation on the real part of the dielectric function by taking $\omega = 0$. The upper limit of the q-integration is $2p$, which is the maximum allowed momentum transfer in a scattering. Thus the integral is rewritten as:

$$\frac{dE_{\mathbf{p}}}{dt}=\frac{1}{2\hbar\pi^2}\frac{1}{1-e^{-\beta\omega}}\int_0^{2\pi}d\theta\int_0^{2p}qdqIm\left[\frac{V_{\mathbf{q}}}{\kappa(\mathbf{q},\omega)}\right](2pq\cos\theta-q^2). \tag{3-9}$$

3.2 Results and Discussion

In Figure 3-2, we plot the momentum dependence of the energy loss rate (ELR) of an external electron in the *n*-type HgTe/CdTe QW. The zero-temperature chemical potential is chosen to be 0.05 eV. At low energy, the electron is only being scattered by the intraband excitations. In the present system, the band velocity is about 7×10^5 m/s and the electron effective mass is about $0.015m_e$. For an incident electron with p =1/nm, (we set $\hbar = 1$ hereafter). there is a large mismatch between the momentum of the incoming particle and that of the band electron. Therefore the incoming electron loses very little energy to the intraband excitation of the QW. When this incident energy exceeds the threshold energy, which is the sum of the band gap and the chemical potential, $E_{\text{th}} = \varepsilon_g + \mu$ (corresponding to p = 2.4/nm), the electron can be strongly scattered by the interband excitations. As a result, the ELR increases significantly. The ELR by the intraband process and that by the interband process both increase with the incoming electron momentum. This is because the momentum transfer (or scattering phase space) increases with p. For the intraband process, the ELR is roughly quadratic in p. The ELR increases very rapidly with p, however, at the onset of the interband process. When the incident energy reaches E_{th}, the ELR resembles an exponential type of p-dependence. This suggests an activation-type electronic transition near the E_{th}. At high momentum, all electronic excitations contribute to the energy and momentum exchange with the incoming particle and the ELR tends to saturate. This result is very different from non-doping cases, where the ELR is dominated by the interband contribution. [161, 162]

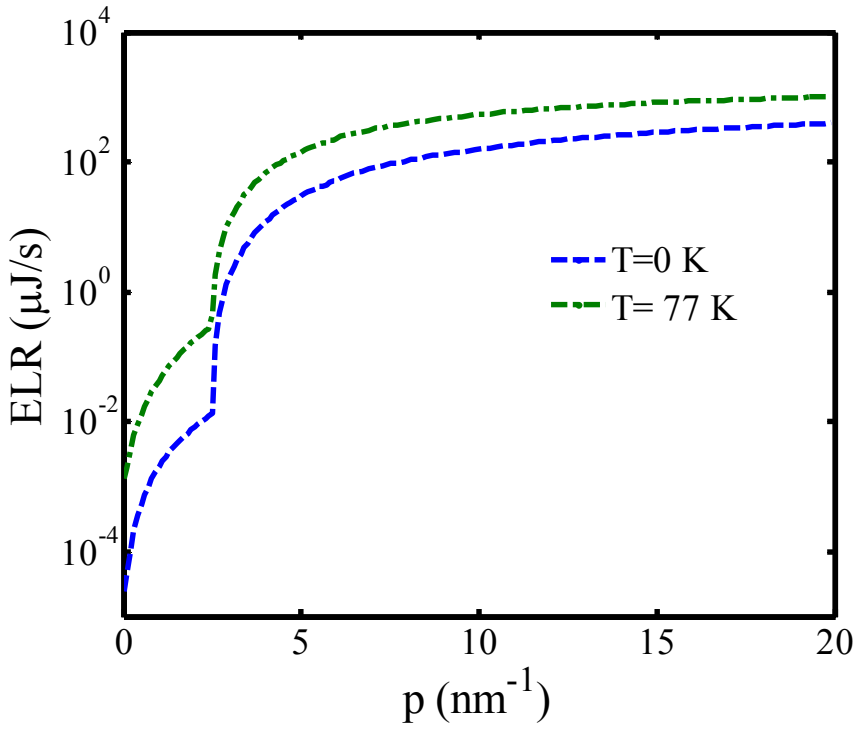

Figure 3-2 Momentum dependent ELR of an incident electron at 0 K and 77 K. $\hbar = 1$.

The ELR from the intraband process increases montonically with the temperature. As temperature increases, more carriers contribute to the static screening. As a result, the coupling between the incident particle and the quasiparticle excitations in the QW becomes stronger, and the ELR increases. Figure 3-3 shows the temperature dependence of the ELR with incident momentum of 1.0/nm and 10/nm corresponding to the intraband process. At p = 10/nm, the ELR is mainly due to the interband process. The interband transition rate decreases with increasing temperature due to the reduced phase space at high temperatures. This partly cancels the temperature effect of static screening. As a result, the ELR is approximately temperature independent at high temperature and high momentum.

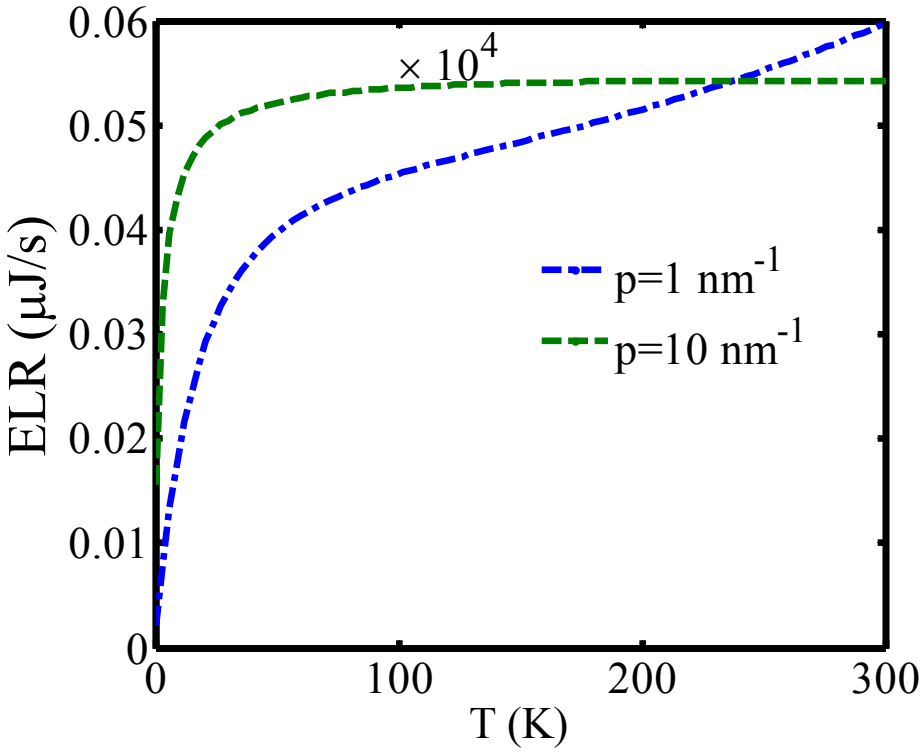

Figure 3-3. ELR versus temperature for external electrons with momenta p = 1 nm^{-1} and p = 10 nm^{-1}

The mean inelastic scattering rate of the incident particle by the quantum is defined as: $1/\tau = \left(dE_{\mathbf{p}}/dt\right)E_{\boldsymbol{p}}^{-1}$. Figure 3-4 shows the mean scattering rate at zero temperature. For the intraband process, the scattering rate is nearly constant. There is a rapid increase in the rate near E_{th}. At high momentum, the rate decreases with p. The interesting point is that for a large range of p, the scattering rate is between 1 and 5 terahertz. Therefore it is expected that the ELR can be tuned resonantly by weak terahertz radiation.

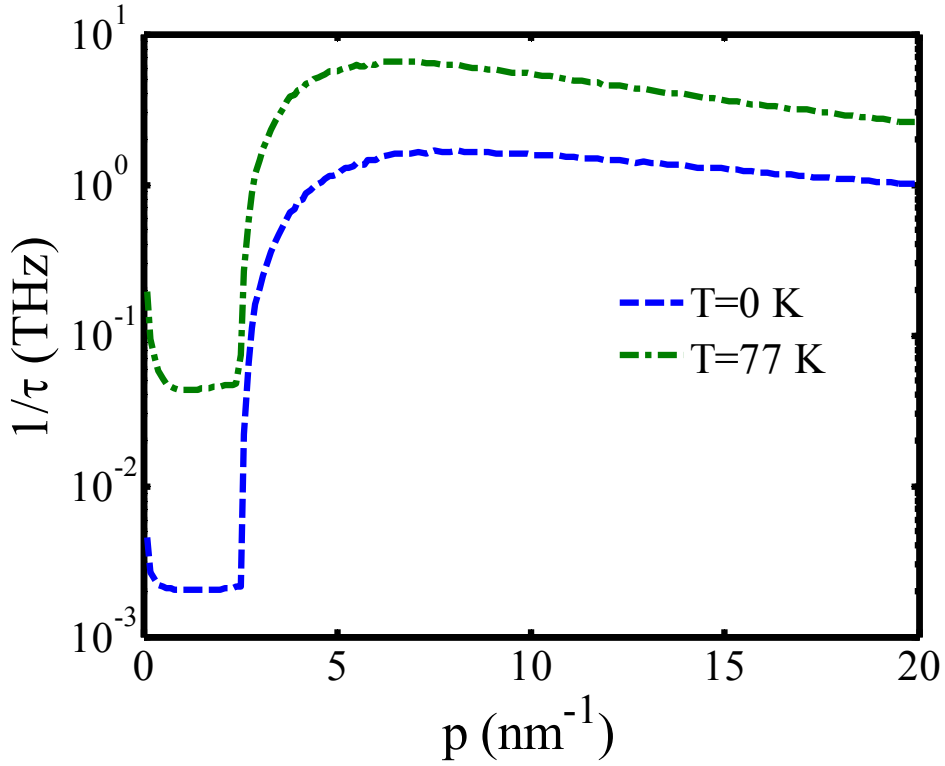

Figure 3-4 Mean inelastic scattering rate as a function of incident momentum at 0 K and 77 K.

We now briefly discuss another related physical quantity, the diffusion constant, defined as $D_{\mathbf{p}} \sim (mp)^2\tau_{\mathbf{p}} \sim E_{\mathbf{p}}\tau_{\mathbf{p}}$. Figure 3-5 shows the momentum dependent diffusion constant at zero temperature. The diffusion constant increases with the energy in the intraband excitation regime. The onset of the interband process leads to a sudden drop of $D_{\mathbf{p}}$ and a diffusion peak is observed at E_{th}. For large momenta, $D_{\mathbf{p}}$ is approximately a quadratic function of the incoming momentum. For incoming energies immediately above E_{th}, the diffusion is minimal in a finite range of p. This is quite intriguing, as it suggests that the incident electron is nearly localized due to the strong scattering by the interband excitations.

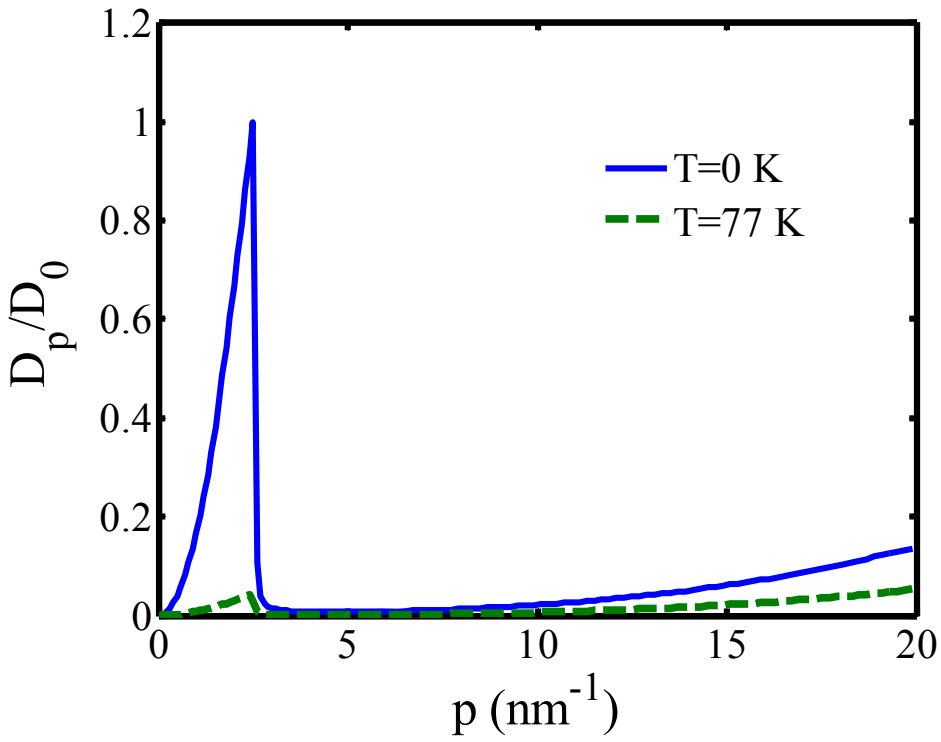

Figure 3-5. Normalised diffusion constant versus momentum of the incident electron at 0 K and 77 K. $D_0 = D_{max}(T=0)$.

In conclusion, the energy loss rate of an electron in an *n*-type HgTe/CdTe QW has been calculated. We found that, for slow electrons, the ELR is determined by the intraband contribution only, while for fast electrons, the ELR is dominated by the interband contribution. The mean inelastic scattering rate is in the terahertz frequency regime. At different energies, the incident electron can either diffuse resonantly, or almost be localized.

CHAPTER 4 DYNAMIC CONDUCTIVITY OF AN *N*-TYPE HGTE/CDTE QUANTUM WELL TOPOLOGICAL INSULATOR

The real part frequency dependent conductivity $\sigma(\omega)$ gives information on the absorption spectrum. In this Chapter we will study the frequency dependent conductivity of the bulk in the 2D topological insulator system, the HgTe/CdTe QWs. We apply a homogeneous, oscillating electric field to our system and use linear-response theory to calculate the current response of the system to such an external field.[163] We also find that the effective ion potential is screened by the self-consistent field of the electrons, and therefore, we neglect all the terms that is non-linear in the screened ion potential (which is to the lowest order of electron-impurity interaction). In the numerical results, we will first consider the frequency-dependent electrical transport of the bulk state of an *n*-type HgTe/CdTe QW with different chemical potentials. Under small excitation energy, only the intra-band excitation contributes to the conductivity, as there is a significant gap lying between the conduction- and valence-bands. We will also consider on the temperature effect contributed dielectric function. In the high frequency regime, Born approximation is applicable and only the lowest order electron-impurity interaction is required.

4.1 Formalism

4.1.1 Current operator

We consider an HgTe/CdTe QW lying in the *x*-*y* plane, and the thickness along the *z* direction is 7.0 nm. Under a weak time-dependent electric field, $\boldsymbol{E} =$

$\boldsymbol{E_0}e^{-i\omega t}$, the many body Hamiltonian of the system, in second quantized notation, is written as,

$$H = H_0 + H^{e-e} + H^{e-I}. \tag{4-1}$$

H_0 is the non-interacting Hamiltonian of a 2D system coupled to an electric field.

$$H_0 = H_{(\mathbf{k}+\mathbf{A})} = \sum_{\mathbf{k},s} \varepsilon_{\mathbf{k}+\mathbf{A},s} a^{\dagger}_{\mathbf{k},s} a_{\mathbf{k},s}. \tag{4-2}$$

$$\mathbf{A}_e = \frac{c\mathbf{E}}{i\omega} e^{-i\omega t}.$$

Here, $\mathbf{A}_e$ is the vector potential of the external electric field and **E** is the electric field. $a^{\dagger}_{k,s}$ and $a_{k,s}$ are the creation and annihilation operators for an electron with momentum *k* and band *s*. The energy dispersion $\varepsilon_{\mathbf{k},s}$ is given by Eq. (1-4).

$H^{e\text{-}e}$ is the electron-electron interaction.

$$H^{e-e} = \frac{1}{2} \sum_{\mathbf{k}',\mathbf{k},\mathbf{q},ss'} V(\mathbf{q}) \left[\varphi^{\dagger}_{\mathbf{k}+\mathbf{q},s} \varphi_{\mathbf{k},s} \varphi^{\dagger}_{\mathbf{k}'-\mathbf{q},s'} \varphi_{\mathbf{k}',s'} \right] a^{\dagger}_{\mathbf{k}+\mathbf{q},s} a^{\dagger}_{\mathbf{k}'-\mathbf{q},s'} a_{\mathbf{k}',s'} a_{\mathbf{k},s}. \tag{4-3}$$

$H^{e\text{-}I}$ is the electron-random impurities interaction.

$$H^{e-I} = -Z \int dq V_{\mathbf{q}} \sum_i e^{-i\mathbf{q}\cdot\mathbf{R}_i} \sum_{\mathbf{k},ss'} \left(\varphi^{\dagger}_{\mathbf{k}+\mathbf{q},s'} \varphi_{\mathbf{k},s} \right) a^{\dagger}_{\mathbf{k}+\mathbf{q},s'} a_{\mathbf{k},s}. \tag{4-4}$$

$V_{\mathbf{q}} = \frac{e^2}{2\kappa_0 \kappa_s |\mathbf{q}|}$ is the Fourier transform of the electron-electron Coulomb potential, κ_s is the background static dielectric constant. For CdTe, κ_s =9.4. R_i is the position of the i^{th} ion. φ is the wave function of electrons in the HgTe/CdTe QW. The total average current density of the system is defined as:

$$\mathbf{j} = c \langle \frac{\partial H}{\partial \mathbf{A}_e} \rangle. \tag{4-5}$$

To the lowest order of the electric field (linear response), the current density is given as:

$$\mathbf{j}_{\mathbf{k},\alpha} = e\sum_{\mathbf{k},s}\left(-2De\mathbf{A}_e - 2D\mathbf{k} + R_{\mathbf{k},s}\mathbf{k}\right)\langle a^{\dagger}_{\mathbf{k},s}a_{\mathbf{k},s}\rangle. \tag{4-6}$$

where

$$R_{\mathbf{k},s} = \frac{A^2 - 2BM + 2B^2k^2}{s\sqrt{(M - Bk^2)^2 + A^2k^2}}. \tag{4-7}$$

We rewrite the total average current density in two parts:

$$\boldsymbol{j}(\omega) = \boldsymbol{j}^{ns}(\omega) + \boldsymbol{j}^{sc}(\omega). \tag{4-8}$$

$\boldsymbol{j}^{ns}(\omega)$ is the current with no scattering:

$$\begin{aligned}\mathbf{j}^{ns}(\omega) &= (-2D)\frac{ie^2}{\omega}\mathbf{E}\sum_{\mathbf{k},s}\langle a^{\dagger}_{\mathbf{k},s}a_{\mathbf{k},s}\rangle = \left(-\frac{2mD}{\hbar^2}\right)\frac{ine^2}{m\omega}\mathbf{E} \\ &= \left(-\frac{2mD}{\hbar^2}\right)\sigma_0\mathbf{E}.\end{aligned} \tag{4-9}$$

$\sigma_0 = ine^2/m\omega$ is the well-known Drude conductivity in the absence of electron-impurity scattering. D is just a parameter of the material which is independent of the frequency, while $\boldsymbol{j}^{sc}(\omega)$ is the current including scattering:

$$j^{sc}(\omega) = e\sum_{\mathbf{k},s}\left(-2D + R_{\mathbf{k},s}\right)\mathbf{k}\,\langle a^{\dagger}_{\mathbf{k},s}a_{\mathbf{k},s}\rangle. \tag{4-10}$$

4.1.2 Density matrix *F*

Now, let us defined the single-electron density matrix element between states $\langle\mathbf{k},\alpha|$ and $|\mathbf{k}+\mathbf{q},\alpha'\rangle$ as:

$$F_{\alpha'\alpha}(\mathbf{k}+\mathbf{q},\mathbf{k},t) = \langle a^{\dagger}_{\mathbf{k},\alpha}a_{\mathbf{k}+\mathbf{q},\alpha'}\rangle, \tag{4-11}$$

where $\alpha = \pm 1$ corresponds to the valence and conduction band. The equation of motion for the single-electron density matrix element is[157, 163-165]:

$$i\frac{\partial}{\partial t}F_{\alpha'\alpha}(\mathbf{k}+\mathbf{q},\mathbf{k},t)=\frac{1}{\hbar}[F_{\alpha'\alpha}(\mathbf{k}+\mathbf{q},\mathbf{k},t),H]. \tag{4-12}$$

Substitute Eqs. (4-3) and (4-4) into Eq. (4-12),

$$\begin{aligned} i\frac{\partial}{\partial t}F_{\alpha'\alpha}(\mathbf{k}+\mathbf{q},\mathbf{k},t) & \\ &= \left(\varepsilon_{\mathbf{k}+\mathbf{q}+\mathbf{A},\alpha'}-\varepsilon_{\mathbf{k}+\mathbf{A},\alpha}\right)F_{\alpha'\alpha}(\mathbf{k}+\mathbf{q},\mathbf{k},t) \\ &+\sum_{\mathbf{q}'}V_{\mathbf{q}}\left[n(\mathbf{q}')-Z\sum_{i}e^{-i\mathbf{q}'\cdot\mathbf{R}_i}\right] \\ &\times\left[\left(\varphi^{\dagger}_{\mathbf{k}+\mathbf{q},\alpha}\varphi_{\mathbf{k},\alpha}\right)F_{\alpha'\alpha}(\mathbf{k}+\mathbf{q},\mathbf{k}+\mathbf{q}')\right. \\ &\left.-\left(\varphi^{\dagger}_{\mathbf{k}+\mathbf{q}',\alpha'}\varphi_{\mathbf{k}+\mathbf{q}'-\mathbf{q},\alpha'}\right)F_{\alpha'\alpha}(\mathbf{k}+\mathbf{q}'-\mathbf{q},\mathbf{k})\right]. \end{aligned} \tag{4-13}$$

or simplicity, we set $\hbar=1$, put it back to the equation at the end of our calculation. We have also neglected the nonlinear terms in the external field. The electron density of the system is defined as:

$$n(q)=\sum_{s,s'=\pm1}\left[\sum_{\mathbf{k}}\varphi^{\dagger}_{\mathbf{k},s}\varphi_{\mathbf{k}+\mathbf{q},s'}F_{s's}(\mathbf{k}+\mathbf{q},\mathbf{k})\right]. \tag{4-14}$$

Let $\mathbf{p}=0$; Thus the expression for $\boldsymbol{j}^{sc}(\omega)$ is

$$\begin{aligned} j^{sc}(\omega)=-\frac{e}{\omega}\sum_{\mathbf{q}}V_{\mathbf{q}}&\left[n(-\mathbf{q})-Z\sum_{i}e^{-i\mathbf{q}\cdot\mathbf{R}_i}\right] \\ &\times\sum_{\mathbf{k},s,s'}\left[\left(R_{\mathbf{k}+\mathbf{q},s'}-R_{\mathbf{k},s}\right)\mathbf{k}\right. \\ &\left.+\left(R_{\mathbf{k}+\mathbf{q},s'}-2D\right)\mathbf{q}\right]\left[\varphi^{\dagger}_{\mathbf{k},s}\varphi_{\mathbf{k}+\mathbf{q},s'}F_{s's}(\mathbf{k}+\mathbf{q},\mathbf{k})\right] \end{aligned}$$

$$= -\frac{Ze}{\omega}\sum_{\mathbf{q}} V_{\mathbf{q}} \sum_{i} e^{-i\mathbf{q}\cdot\mathbf{R}_i}$$

$$\times \sum_{k,s,s'} \left[\left(R_{\mathbf{k+q},s'} - R_{\mathbf{k},s}\right)\mathbf{k}\right.$$

$$\left. + \left(R_{\mathbf{k+q},s'} - 2D\right)\mathbf{q}\right]\left[\varphi^{\dagger}_{\mathbf{k},s}\varphi_{\mathbf{k+q},s'}F_{s's}(\mathbf{k}+\mathbf{q},\mathbf{k})\right]. \quad (4\text{-}15)$$

In arriving at Eq. (4-15), we have used the following property for an isotropic system,

$$\sum_{\mathbf{q}} V_{\mathbf{q}} n(-\mathbf{q}) \sum_{\mathbf{k},s,s'} \left[R_{\mathbf{k+q},s'}\cdot(\mathbf{k}+\mathbf{q}) - R_{\mathbf{k},s}\right.$$

$$\left.\cdot\,\mathbf{k}\right] \times \varphi^{\dagger}_{\mathbf{k},s}\varphi_{\mathbf{k+q},s'}F_{s's}(\mathbf{k}+\mathbf{q},\mathbf{k}) = 0.$$

We now present the main results. In the absence of the impurities and the applied field, electrons are free and are described by the Fermi-Dirac distribution, $f = \frac{1}{1+e^{\beta(\varepsilon_{\mathbf{k}}-\mu)}}$, where $\beta = 1/k_B T$, with k_B the Boltzmann constant and μ is the chemical potential. The zeroth-order density matrix element is given as:

$$F^{(0)}_{\alpha'\alpha}(\mathbf{k}+\mathbf{q},\mathbf{k},t) = f_{\mathbf{k}}\delta_{\mathbf{k},0}\delta_{\alpha'\alpha}. \quad (4\text{-}16)$$

In the first order approximation, we assume that the external field is zero and determine the change of in the static electron density matrix due to the impurities. From Eq. (4-13), we obtain the equation for the first order density matrix self-consistently:

$$
\begin{aligned}
0 = {} & \left(E_{\mathbf{k}+\mathbf{q},\alpha'} - E_{\mathbf{k},\alpha}\right) F^{1}_{\alpha'\alpha}(\mathbf{k}+\mathbf{q},\mathbf{k},t) \\
& - \sum_{\mathbf{q}'} V_{\mathbf{q}'} \left[n(\mathbf{q}') - Z \sum_{i} e^{-i\mathbf{q}'\cdot\mathbf{R}_i} \right] \\
& \times \left[\left(\varphi^{\dagger}_{\mathbf{k}+\mathbf{q},\alpha'} \varphi_{\mathbf{k},\alpha} \right) F_{\alpha'\alpha}(\mathbf{k}+\mathbf{q}',\mathbf{k}+\mathbf{q}) \right. \\
& \left. - \left(\varphi^{\dagger}_{\mathbf{k}+\mathbf{q}',\alpha'} \varphi_{\mathbf{k}+\mathbf{q}'-\mathbf{q},\alpha'} \right) F_{\alpha'\alpha}(\mathbf{k}+\mathbf{q}'-\mathbf{q},\mathbf{k}) \right].
\end{aligned}
\tag{4-17}
$$

The first order density matrix is:

$$
\begin{aligned}
& F^{1}_{\alpha'\alpha}(\mathbf{k}+\mathbf{q},\mathbf{k},t) \\
& = - \frac{\left(\varphi^{\dagger}_{\mathbf{k}+\mathbf{q},\alpha'} \varphi_{\mathbf{k},\alpha} \right) \left(f_{\mathbf{k}+\mathbf{q},\alpha'} - f_{\mathbf{k},\alpha} \right)}{E_{\mathbf{k}+\mathbf{q},\alpha'} - E_{\mathbf{k},\alpha}} V_{\mathbf{q}} \left[n^{1}(\mathbf{q}) \right. \\
& \left. - Z \sum_{i} e^{-i\mathbf{q}\cdot\mathbf{R}_i} \right].
\end{aligned}
\tag{4-18}
$$

Upon using Eq. (4-14), we obtain the electron density corresponding to the density matrix $F^{(1)}$:

$$
n^{1}(\mathbf{q}) = -\Pi(q,0) V_{\mathbf{q}} \left[n^{1}(\mathbf{q}) - Z \sum_{i} e^{-i\mathbf{q}\cdot\mathbf{R}_i} \right]. \tag{4-19}
$$

and then,

$$
n^{1}(\mathbf{q}) = Z \left[1 - \frac{1}{\kappa(q,0)} \right] \sum_{i} e^{-i\mathbf{q}\cdot\mathbf{R}_i}, \tag{4-20}
$$

where $\kappa(q,\omega)$ is the dielectric function is defined as

$$
\kappa(q,\omega) = 1 - V_{\mathbf{q}} \Pi(q,\omega). \tag{4-21}
$$

$\Pi\,(q,\omega)$ is the polarization function:

$$
\Pi\,(q,\omega) = \int \frac{d\mathbf{k}}{(2\pi)^2} \sum_{\alpha'\alpha} \frac{\left| \varphi^{\dagger}_{\mathbf{k}+\mathbf{q},\alpha'} \varphi_{\mathbf{k},\alpha} \right|^2 \left(f_{\mathbf{k}+\mathbf{q},\alpha'} - f_{\mathbf{k},\alpha} \right)}{\varepsilon_{\mathbf{k}+\mathbf{q},\alpha'} - \varepsilon_{\mathbf{k},\alpha} - \omega - i\delta} (\delta \to 0). \tag{4-22}
$$

Substituting Eq. (4-20) into Eq. (4-18), we find the density matrix element of first order to be:

$$F^{(1)}_{\alpha'\alpha}(\mathbf{k}+\mathbf{q},\mathbf{k},t) = -Z\frac{\left(\varphi^{\dagger}_{\mathbf{k}+\mathbf{q},\alpha'}\varphi_{\mathbf{k},\alpha}\right)\left(f_{\mathbf{k}+\mathbf{q},\alpha'}-f_{\mathbf{k},\alpha}\right)}{\varepsilon_{\mathbf{k}+\mathbf{q},\alpha'}-\varepsilon_{\mathbf{k},\alpha}}\frac{V_{\mathbf{q}}}{\kappa(q,0)}\sum_i e^{-i\mathbf{q}\cdot\mathbf{R}_i}. \tag{4-23}$$

Next, we consider the time-dependent part of the single-electron density matrix element $F^{(2)}$ under the influence of the external field and of the impurities.

$$\begin{aligned} & i\frac{\partial}{\partial t}F^2_{\alpha'\alpha}(\mathbf{k}+\mathbf{q},\mathbf{k},t) = \omega F^2_{\alpha'\alpha}(\mathbf{k}+\mathbf{q},\mathbf{k},t) \\ & = \left(E_{\mathbf{k}+\mathbf{q},\alpha'}-E_{\mathbf{k},\alpha}\right)F^2_{\alpha'\alpha}(\mathbf{k}+\mathbf{q},\mathbf{k},t) \\ & +e\left[\left(R_{\mathbf{k}+\mathbf{q},\alpha'}-R_{\mathbf{k},\alpha}\right)\mathbf{k}\cdot\mathbf{A}_e+\left(R_{\mathbf{k}+\mathbf{q},\alpha'}-2D\right)\mathbf{q}\cdot\mathbf{A}_e\right]F^1_{\alpha'\alpha}(\mathbf{k}+\mathbf{q},\mathbf{k},t) \\ & -\sum_{\mathbf{q}'}V_{\mathbf{q}'}[n^2(\mathbf{q}')]\times\left[\left(\varphi^{\dagger}_{\mathbf{k}+\mathbf{q},\alpha'}\varphi_{\mathbf{k},\alpha}\right)F^0_{\alpha'\alpha}(\mathbf{k}+\mathbf{q}',\mathbf{k}+\mathbf{q})\right. \\ & \left.-\left(\varphi^{\dagger}_{\mathbf{k}+\mathbf{q}',\alpha'}\varphi_{\mathbf{k}+\mathbf{q}'-\mathbf{q},\alpha'}\right)F^0_{\alpha'\alpha}(\mathbf{k}+\mathbf{q}'-\mathbf{q},\mathbf{k})\right]. \end{aligned} \tag{4-24}$$

Then,

$$\begin{aligned} & F^2_{\alpha'\alpha}(\mathbf{k}+\mathbf{q},\mathbf{k},t) \\ & =\frac{iZe}{2\omega}\frac{\left(R_{\mathbf{k}+\mathbf{q},\alpha'}-R_{\mathbf{k},\alpha}\right)}{\kappa(q,0)}\sum_i e^{-i\mathbf{q}\cdot\mathbf{R}_i}\frac{V_{\mathbf{q}}\left(\varphi^{\dagger}_{\mathbf{k}+\mathbf{q},\alpha'}\varphi_{\mathbf{k},\alpha}\right)\left(f_{\mathbf{k}+\mathbf{q},\alpha'}-f_{\mathbf{k},\alpha}\right)}{\left(E_{\mathbf{k}+\mathbf{q},\alpha'}-E_{\mathbf{k},\alpha}-\omega\right)\left(E_{\mathbf{k}+\mathbf{q},\alpha'}-E_{\mathbf{k},\alpha}\right)}\mathbf{k}\cdot\mathbf{E} \\ & +\frac{iZe}{2\omega}\frac{\left(R_{\mathbf{k}+\mathbf{q},\alpha'}-2D\right)}{\kappa(q,0)}\sum_i e^{-i\mathbf{q}\cdot\mathbf{R}_i}\frac{V_{\mathbf{q}}\left(\varphi^{\dagger}_{\mathbf{k}+\mathbf{q},\alpha'}\varphi_{\mathbf{k},\alpha}\right)\left(f_{\mathbf{k}+\mathbf{q},\alpha'}-f_{\mathbf{k},\alpha}\right)}{\left(E_{\mathbf{k}+\mathbf{q},\alpha'}-E_{\mathbf{k},\alpha}-\omega\right)\left(E_{\mathbf{k}+\mathbf{q},\alpha'}-E_{\mathbf{k},\alpha}\right)}\mathbf{q}\cdot\mathbf{E} \\ & +n^2(\mathbf{q})\frac{V_{\mathbf{q}}\left(\varphi^{\dagger}_{\mathbf{k}+\mathbf{q},\alpha'}\varphi_{\mathbf{k},\alpha}\right)\left(f_{\mathbf{k}+\mathbf{q},\alpha'}-f_{\mathbf{k},\alpha}\right)}{E_{\mathbf{k}+\mathbf{q},\alpha'}-E_{\mathbf{k},\alpha}-\omega}. \end{aligned} \tag{4-25}$$

We construct the form of the electron density n^2 by multiplying overlap term with $F^{(2)}$ and summing over $\mathbf{k}$ and α.

$$\sum_{\mathbf{k},\alpha'\alpha} \varphi^{\dagger}_{\mathbf{k},s}\varphi_{\mathbf{k+q},s'}\, F^{2}_{\alpha'\alpha}(\mathbf{k}+\mathbf{q},\mathbf{k},t)$$

$$= \frac{iZe}{2\omega}\frac{\left(R_{\mathbf{k+q},\alpha'}-R_{\mathbf{k},\alpha}\right)}{\kappa(q,0)}\sum_{i} e^{-i\mathbf{q}\cdot\mathbf{R}_i}\sum_{\mathbf{k},\alpha'\alpha}\frac{V_{\mathbf{q}}\left|\varphi^{\dagger}_{\mathbf{k+q},\alpha'}\varphi_{\mathbf{k},\alpha}\right|^{2}\left(f_{\mathbf{k+q},\alpha'}-f_{\mathbf{k},\alpha}\right)\mathbf{k}\cdot\mathbf{E}}{\left(E_{\mathbf{k+q},\alpha'}-E_{\mathbf{k},\alpha}-\omega\right)\left(E_{\mathbf{k+q},\alpha'}-E_{\mathbf{k},\alpha}\right)}$$

$$+\frac{iZe}{2\omega}\frac{\left(R_{\mathbf{k+q},\alpha'}-2D\right)}{\kappa(q,0)}\sum_{i} e^{-i\mathbf{q}\cdot\mathbf{R}_i}\sum_{\mathbf{k},\alpha'\alpha}\frac{V_{\mathbf{q}}\left|\varphi^{\dagger}_{\mathbf{k+q},\alpha'}\varphi_{\mathbf{k},\alpha}\right|^{2}\left(f_{\mathbf{k+q},\alpha'}-f_{\mathbf{k},\alpha}\right)\mathbf{q}\cdot\mathbf{E}}{\left(E_{\mathbf{k+q},\alpha'}-E_{\mathbf{k},\alpha}-\omega\right)\left(E_{\mathbf{k+q},\alpha'}-E_{\mathbf{k},\alpha}\right)}$$

$$+n^{2}(\mathbf{q})V_{\mathbf{q}}\sum_{\mathbf{k},\alpha'\alpha}\frac{\left|\varphi^{\dagger}_{\mathbf{k+q},\alpha'}\varphi_{\mathbf{k},\alpha}\right|^{2}\left(f_{\mathbf{k+q},\alpha'}-f_{\mathbf{k},\alpha}\right)}{E_{\mathbf{k+q},\alpha'}-E_{\mathbf{k},\alpha}-\omega}. \tag{4-26}$$

The second order electron density is:

$$n^{2}(\mathbf{q}) =$$

$$\frac{iZe}{2\omega}\frac{V_{\mathbf{q}}}{\kappa(q,\omega)\kappa(q,0)}\sum_{i} e^{-i\mathbf{q}\cdot\mathbf{R}_i}\times\left\{\sum_{\mathbf{k},\alpha'\alpha}\left(R_{\mathbf{k+q},\alpha'}-R_{\mathbf{k},\alpha}\right)\frac{\left(\varphi^{\dagger}_{\mathbf{k+q},\alpha'}\varphi_{\mathbf{k},\alpha}\right)\left(f_{\mathbf{k+q},\alpha'}-f_{\mathbf{k},\alpha}\right)}{E_{\mathbf{k+q},\alpha'}-E_{\mathbf{k},\alpha}-\omega}\mathbf{k}\cdot\mathbf{E}-\right.$$

$$\sum_{\mathbf{k},\alpha'\alpha}\left(R_{\mathbf{k+q},\alpha'}-R_{\mathbf{k},\alpha}\right)\frac{\left(\varphi^{\dagger}_{\mathbf{k+q},\alpha'}\varphi_{\mathbf{k},\alpha}\right)\left(f_{\mathbf{k+q},\alpha'}-f_{\mathbf{k},\alpha}\right)}{E_{\mathbf{k+q},\alpha'}-E_{\mathbf{k},\alpha}}\mathbf{k}\cdot\mathbf{E}+\sum_{\mathbf{k},\alpha'\alpha}\left(R_{\mathbf{k+q},\alpha'}-\right.$$

$$\left.2D\right)\frac{\left(\varphi^{\dagger}_{\mathbf{k+q},\alpha'}\varphi_{\mathbf{k},\alpha}\right)\left(f_{\mathbf{k+q},\alpha'}-f_{\mathbf{k},\alpha}\right)}{E_{\mathbf{k+q},\alpha'}-E_{\mathbf{k},\alpha}-\omega}\mathbf{q}\cdot\mathbf{E}-$$

$$\left.\sum_{\mathbf{k},\alpha'\alpha}\left(R_{\mathbf{k+q},\alpha'}-2D\right)\frac{\left(\varphi^{\dagger}_{\mathbf{k+q},\alpha'}\varphi_{\mathbf{k},\alpha}\right)\left(f_{\mathbf{k+q},\alpha'}-f_{\mathbf{k},\alpha}\right)}{E_{\mathbf{k+q},\alpha'}-E_{\mathbf{k},\alpha}}\mathbf{q}\cdot\mathbf{E}\right\}. \tag{4-27}$$

The second order density matrix element can be obtained by substituting Eq. (4-27) in to Eq. (4-25). Next, we proceed to calculate the current in the presence of impurities and electric field.

$$\varphi^{\dagger}_{\mathbf{k},s}\varphi_{\mathbf{k+q},s'}F^{2}_{\alpha'\alpha}(\mathbf{k}+\mathbf{q},\mathbf{k},t)$$

$$= \frac{iZe}{2\omega^2}\frac{V_{\mathbf{q}}}{\kappa(q,0)}\sum_i e^{i\mathbf{q}\cdot\mathbf{R}_i}$$

$$\times\left\{\sum_{\mathbf{k},\alpha'\alpha}\left(R_{\mathbf{k+q},\alpha'}-R_{\mathbf{k},\alpha}\right)\frac{\left|\varphi^{\dagger}_{\mathbf{k+q},\alpha'}\varphi_{\mathbf{k},\alpha}\right|^2\left(f_{\mathbf{k+q},\alpha'}-f_{\mathbf{k},\alpha}\right)}{\left(E_{\mathbf{k+q},\alpha'}-E_{\mathbf{k},\alpha}-\omega\right)}\mathbf{k}\cdot\mathbf{E}\right.$$

$$\left.-\sum_{\mathbf{k},\alpha'\alpha}\left(R_{\mathbf{k+q},\alpha'}-R_{\mathbf{k},\alpha}\right)\frac{\left|\varphi^{\dagger}_{\mathbf{k+q},\alpha'}\varphi_{\mathbf{k},\alpha}\right|^2\left(f_{\mathbf{k+q},\alpha'}-f_{\mathbf{k},\alpha}\right)}{\left(E_{\mathbf{k+q},\alpha'}-E_{\mathbf{k},\alpha}\right)}\mathbf{k}\cdot\mathbf{E}\right\}$$

$$+\frac{iZe}{2\omega^2}\frac{V_{\mathbf{q}}}{\kappa(q,0)}\sum_i e^{i\mathbf{q}\cdot\mathbf{R}_i}$$

$$\times\left\{\sum_{\mathbf{k},\alpha'\alpha}\left(R_{\mathbf{k+q},\alpha'}-2D\right)\frac{\left|\varphi^{\dagger}_{\mathbf{k+q},\alpha'}\varphi_{\mathbf{k},\alpha}\right|^2\left(f_{\mathbf{k+q},\alpha'}-f_{\mathbf{k},\alpha}\right)}{\left(E_{\mathbf{k+q},\alpha'}-E_{\mathbf{k},\alpha}-\omega\right)}\mathbf{q}\cdot\mathbf{E}\right.$$

$$\left.-\sum_{\mathbf{k},\alpha'\alpha}\left(R_{\mathbf{k+q},\alpha'}-2D\right)\frac{\left|\varphi^{\dagger}_{\mathbf{k+q},\alpha'}\varphi_{\mathbf{k},\alpha}\right|^2\left(f_{\mathbf{k+q},\alpha'}-f_{\mathbf{k},\alpha}\right)}{\left(E_{\mathbf{k+q},\alpha'}-E_{\mathbf{k},\alpha}\right)}\mathbf{q}\cdot\mathbf{E}-\right\}$$

$$+\frac{iZe}{2\omega^2}n^2(\mathbf{q})V_{\mathbf{q}}\sum_{\mathbf{k},\alpha'\alpha}\frac{\left(\varphi^{\dagger}_{\mathbf{k+q},\alpha'}\varphi_{\mathbf{k},\alpha}\right)\left(f_{\mathbf{k+q},\alpha'}-f_{\mathbf{k},\alpha}\right)}{E_{\mathbf{k+q},\alpha'}-E_{\mathbf{k},\alpha}-\omega}\mathbf{E}. \tag{4-28}$$

By substituting Eq. (4-28) into Eq. (4-15), the scattering current can be solved.

4.1.3 Computing the conductivity

To numerically evaluate the conductivity, we consider the system to be isotropic with **j** parallel to **E**. For simplify, we also assume that the external electric field is aligned to the *x* direction. The conductivity is given by,

$$\mathbf{j} = \sigma\mathbf{E}. \tag{4-29}$$

The conductivity contributed by the scattering current is:

$$\sigma_x^{sc}(\omega) = \frac{iZne^4}{8\pi\kappa_s\omega^3} I_q(\omega), \tag{4-30}$$

$$I_q(\omega) = \int dq \frac{V_{\mathbf{q}}}{\kappa(q,0)}$$

$$\times \left\{ \frac{V_{\mathbf{q}}\Pi_2(q,\omega)}{\kappa(q,0)} [\Pi_2(q,\omega) - \Pi_2(q,0) + q\Pi_4(q,\omega) - q\Pi_4(q,0)] \right.$$

$$+ \frac{V_{\mathbf{q}}\Pi_4(q,\omega)}{\kappa(q,0)} [q\Pi_2(q,\omega) - q\Pi_2(q,0) + q^2\Pi_4(q,\omega) - q^2\Pi_4(q,0)]$$

$$+2q[\Pi_3(q,\omega) - \Pi_3(q,0)] + q^2[\Pi_5(q,\omega) - \Pi_5(q,0)]$$

$$+[\Pi_1(q,\omega) - \Pi_1(q,0)] + 4Dq[\Pi_2(q,\omega) - \Pi_2(q,0)]. \tag{4-31}$$

The Π functions are defined as follow:

$$\Pi_i(q,\omega) = \sum_{\mathbf{k},\alpha'\alpha} Q_i \frac{\left|\varphi^{\dagger}_{\mathbf{k+q},\alpha'}\varphi_{\mathbf{k},\alpha}\right|^2 \left(f_{\mathbf{k+q},\alpha'} - f_{\mathbf{k},\alpha}\right)}{\left(E_{\mathbf{k+q},\alpha'} - E_{\mathbf{k},\alpha} - \hbar\omega\right)}, \tag{4-32}$$

where

$$Q_1 = \left(R_{\mathbf{k+q},\alpha'} - R_{\mathbf{k},\alpha}\right)^2 k^2, \tag{4-33}$$

$$Q_2 = \left(R_{\mathbf{k+q},\alpha'} - R_{\mathbf{k},\alpha}\right) k cos\theta_{kq}, \tag{4-34}$$

$$Q_3 = \left(R_{\mathbf{k+q},\alpha'} - R_{\mathbf{k},\alpha}\right) R_{\mathbf{k+q},\alpha'} k cos\theta_{kq}, \tag{4-35}$$

$$Q_4 = \left(R_{\mathbf{k+q},\alpha'} - 2D\right), \tag{4-36}$$

$$Q_5 = \left(R_{\mathbf{k+q},\alpha'} - 2D\right)^2, \tag{4-37}$$

The total conductivity including the second order in electron-impurity scattering is written as:

$$\sigma_x(\omega) = \sigma_x^{ns}(\omega) + \sigma_x^{sc}(\omega) = -\left[2m^*D + \frac{Z^2}{8\pi}\frac{r_s}{\gamma^2} I_z(\gamma)\right] \sigma_0. \tag{4-38}$$

We used the dimensionless notation $z = q/k_F$, $\gamma = \omega/\mu$. $r_s = m^*e^2/(\hbar^2 k_F)$. Taking $m^* = 0.015m$, k_F, the Fermi wave vector, can be calculated self-consistently from the carrier density.

Although many terms appeared in Eq. (4-31), the real part of the conductivity is dominated by the following term:

$$\frac{Z^2}{8\pi}\frac{r_s}{\gamma^2}\int z^2 dz \frac{V(z)}{\kappa(z,0)}\left\{Im\Pi_5(z,\gamma) + \frac{V(z)\Pi_4(z,\gamma)}{\kappa(z,\gamma)}[\Pi_4(z,\gamma) - \Pi_4(z,\gamma)]\right\}. \quad (4\text{-}39)$$

Compared to a free 2DEG where the conductivity is determined by the dielectric function, the conductivity in the HgTe/CdTe QW has a more complicated dependence on the electronic transitions. An extra term, $\left(R_{\mathbf{k}+\mathbf{q},\alpha'} - 2D\right)$, appears in the dielectric function and the conductivity. This term arises from the velocity v in the valence band below the Fermi level:

$$v = \frac{\partial \varepsilon_{\mathbf{k}}}{\partial k} = \left(-2D + R_{\mathbf{k},\alpha}\right)k. \quad (4\text{-}40)$$

4.2 Results and discussion

In Figure 4-1, we present the real part of the conductivity at two different chemical potential. The minimum conductivity can be found soon after a dramatic drop in the low frequency regime, and it then clearly increases with a very broad absorption peak. This minimum point distinguishes the intra- and inter-band excitation, and the larger the Fermi energy, the higher frequency the minimum conductivity lies at, e.g. near $\omega = 0.1$ eV for $\mu = 50$ meV and near $\omega = 0.01$ eV for $\mu = 12$ meV. Under a weak excitation, intra-band excitation dominates with a very fast decrease to near zero before the inter-band contribution takes over. The interband

excitation contribution is enhanced with smaller Fermi energy, as there are more empty excited states on the valence band at lower doping levels, which thus raises the transition probability for the conduction electrons.

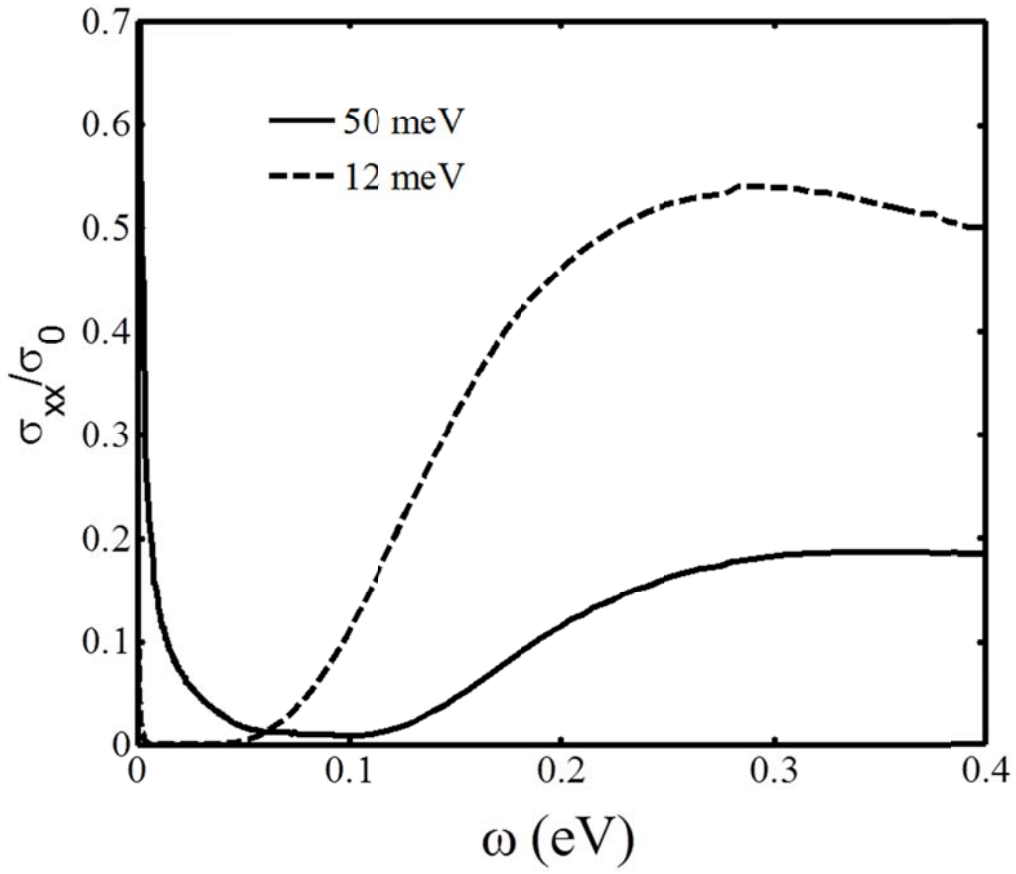

Figure 4-1. The real part of the conductivity as a function of frequency at the different chemical potentials of 12 meV and 50 meV; σ_0 is normalized to $n = 1 \times 10^{11}$ cm^{-2}.

In Figure 4-2, we plot the real part of conductivity for $\mu = 12$ meV, as a function of frequency at the temperatures of 0 K, 4 K, 77 K, and 300 K. In this frequency range which is much lower than the band gap, the conductivity is due to the contribution from intra-band excitations only. We can make some interesting

observations. At fixed temperature, the conductivity decreases rapidly with the frequency at low frequency. This is consistent with the inverse power law dependence of electron-impurity scattering. The temperature dependence of the conductivity is shown in Figure 4-3. At low temperature and for low frequency the conductivity decreases with increasing temperature. This is mainly because the thermal excitation reduces the allowed phase space for intraband transitions (defined by $f_{\mathbf{k+q},\alpha'} - f_{\mathbf{k},\alpha}$). Thus the electron density correlation function (the Π_i functions) decreases with increasing temperature. Also at low frequency the dielectric function is close to its static limit and weakly frequency dependent. As a result, the conductivity decreases as the temperature increases. At high temperatures, more thermally excited carriers reduce the dynamic screening and the electron-impurity scattering is stronger. This leads to the situation where the conductivity increases with temperature. The turnaround in the temperature dependence gives rise to a conductivity minimum in the low temperature regime. At the frequency of 0.1 ω/μ, the minimum is at around 50 K, while for high frequencies, the dynamical screening dominates over the whole temperature regime, and conductivity increases monotonically with temperature. It is worth pointing out that the temperature contribution from the dielectric function has no effect on the inter-band excitation, since the gap plus the Fermi energy is much larger than room-temperature thermal effect.

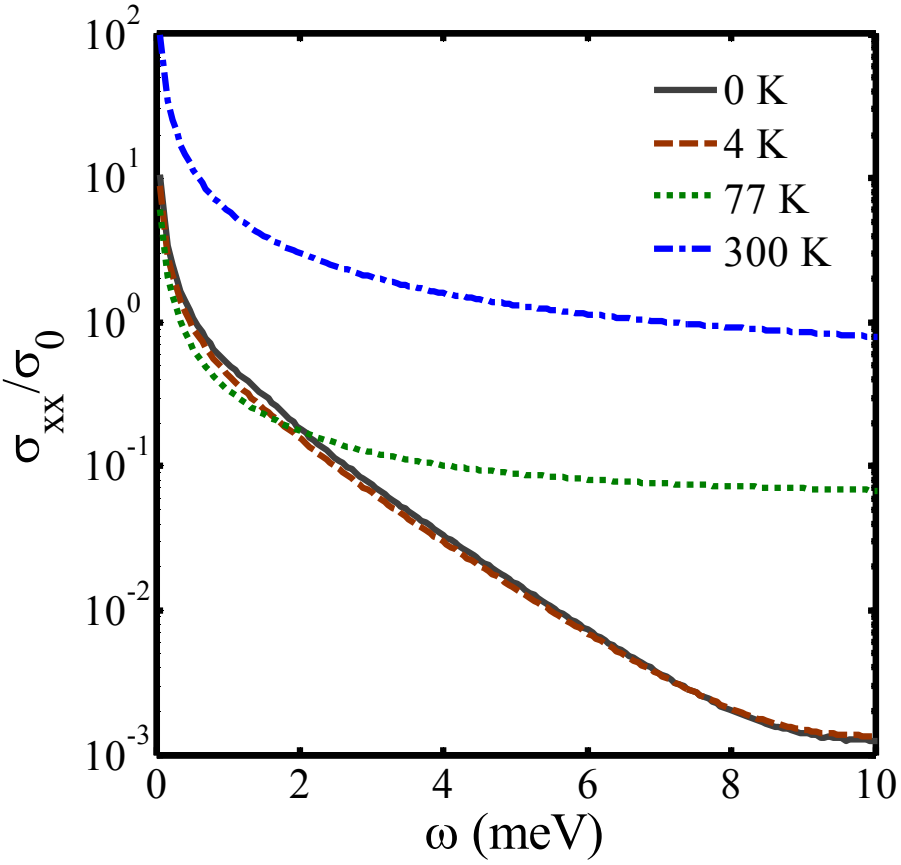

Figure 4-2. The real part of the conductivity versus frequency at different temperatures with μ = 12 meV. ($\hbar = 1$).

By comparing Eq. (4-38) to the Drude model $\sigma = \frac{ine^2}{m^*(\omega+i/\tau)}$, the inverse scattering time can be identified,

$$\tau^{-1} = (Zr_s/16\pi m^* D\gamma)\mathrm{Im}I_z(\omega) \qquad (4\text{-}41)$$

The frequency dependent inverse scattering time is plotted in Figure 4-4. The inverse scattering time depends on the frequency very differently in the low temperature regime from in the high temperature regime. When the temperature is low, the scattering is mainly due to the electrons near the Fermi surface. Electron-impurity scattering by these electrons is inversely proportional to the frequency. As

the frequency increases, electrons travel a shorter distance between scatterers and suffer less scattering. This picture is consistent with the Drude conductivity for degenerate electrons. In the high temperature regime, more electrons away from the Fermi level can participate in the electron-impurity scattering. These thermally excited electrons interact with photons and impurities. As the frequency increases, more thermally excited electrons from deep inside the Fermi sphere can simultaneously satisfy the energy and momentum conservation required in a scattering event. As a result, the scattering rate increases with the frequency.

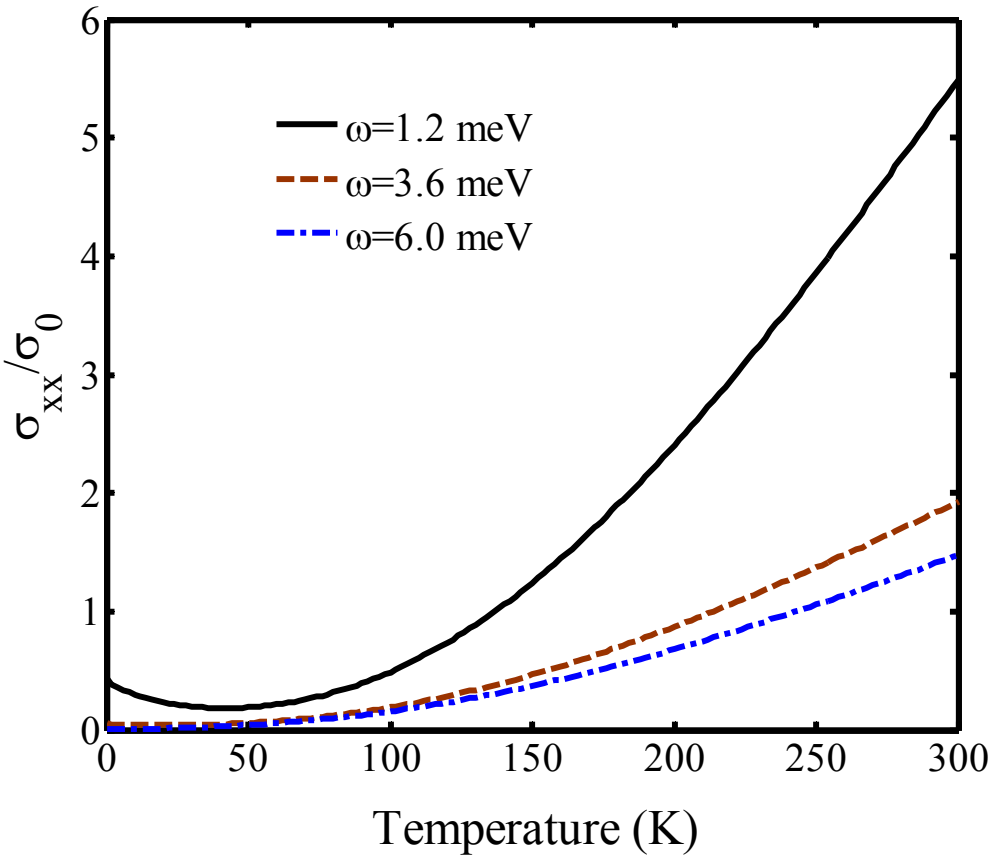

Figure 4-3. The real part of the conductivity as a function of temperature for three frequencies: 1.2 meV, 3.6 meV and 6.0 meV.

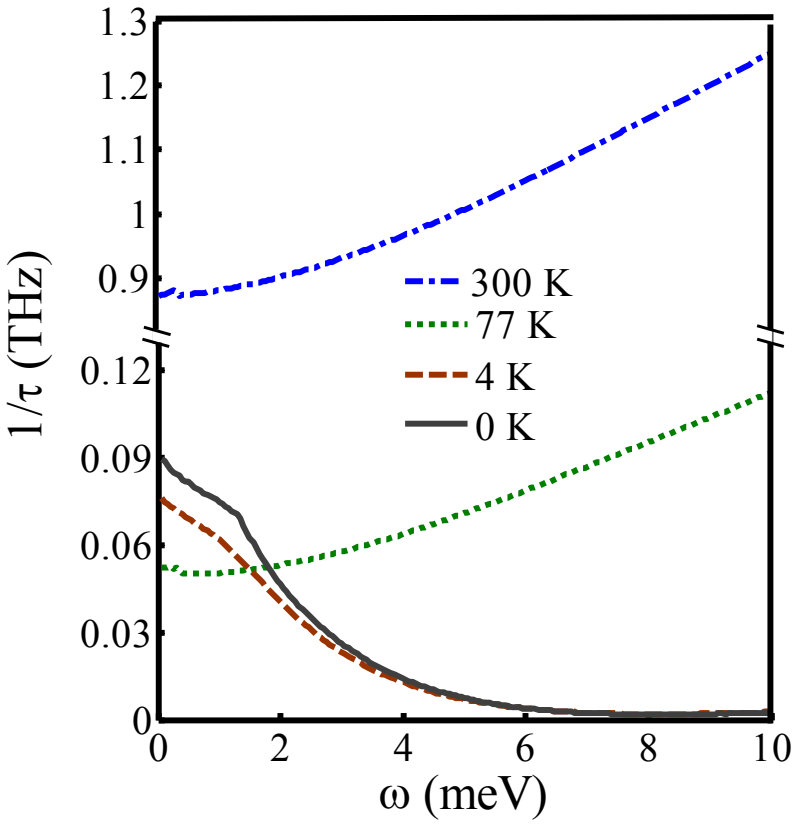

Figure 4-4. Scattering rate versus frequency at four different temperatures: 0 K, 4 K, 77 K and 300 K.

In summary, by using the quantum equations of motion for the electron density matrix, we have calculated the frequency dependent conductivity of the HgTe/CdTe QW in the presence of random impurities. Both the frequency dependence and the temperature dependence of the conductivity and the inverse scattering time have been presented. The inverse transport scattering time decreases with the frequency in the low temperature regime and increases with the frequency in the high temperature regime. Our analysis is based on the properties that the single-particle scattering probability decreases with the frequency and that the number of electrons satisfying the scattering conditions at high temperature increases with the frequency.

CHAPTER 5 PHOTON MIXING IN TOPOLOGICAL INSULATOR HGTE/CDTE QUANTUM WELLS IN THE TERAHERTZ REGIME

The nonlinear multiplication (or up-conversion) process is one common way to obtain low frequency electromagnetic waves from 0.3 THz to 20 THz.[166] One important technique is photon mixing, *e.g.* four wave mixing, which has been thoroughly investigated in the past few decades.[167-170] Three pulsed fields of either the same (degenerate) or different frequencies (non-degenerate) are collinearly focused onto a sample and mixed together to induced a fourth coherent wave with frequency ω_e. Generally, ω_e is a linear combination of the other three frequencies (ω_1, ω_2, ω_3) in a given time order.

The nonlinear optical response (NOR) of the surface state of HgTe/CdTe QW is similar to that of graphene (except that they have slightly different Fermi velocities),[171] and hence the topological insulator (TI) surface state is also expected to be strongly optically nonlinear. In this Chapter, we demonstrate that the bulk state with non-parabolic energy dispersion of an HgTe/CdTe QW can lead to a strong photon mixing effect in the terahertz frequency regime under femtosecond irradiation. It is shown that at a moderate electrical field of around 10^4 V/cm, the generation efficiency of terahertz current from femtosecond fields in the third order is around 10^{-4}. Furthermore, in this class of TI structures, the nonlinear effect remains strong for temperatures up to 150 K. Unlike the gapless surface state in a TI, the existence of which is critically dependent on the thickness of the sample, the bulk state is much more robust. Therefore our result should lead to wider application of TIs in electronics and photonics.

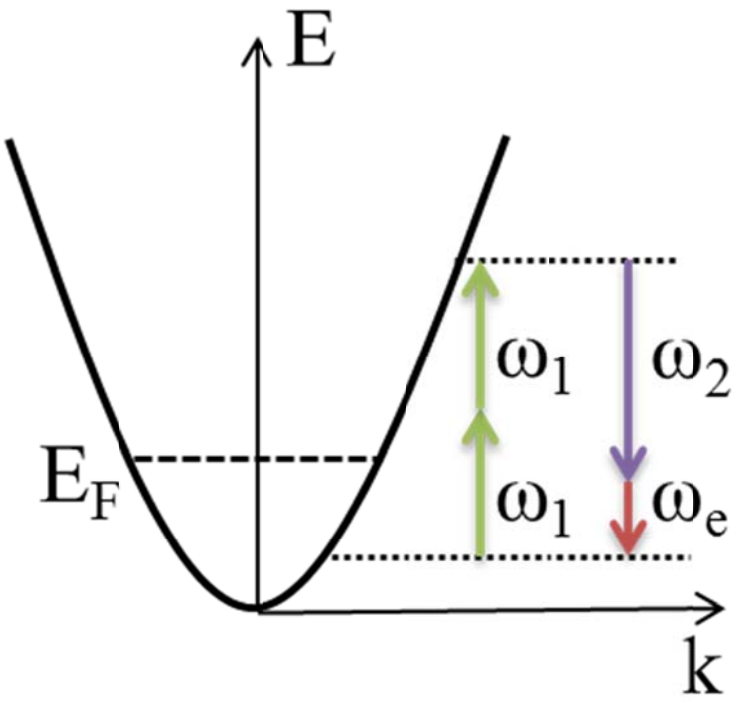

Figure 5-1. Schematic diagram of energy transfer of intraband electrons for four-wave mixing in the bulk HgTe/CdTe QW.

5.1 Formalism

In the limit of no pumping saturation, the mixing of three different fields (ω_1, ω_2, ω_3) is dominated by the third order current oscillations at frequencies that correspond to all possible combinations of (ω_1, ω_2, ω_3)). Here we consider an important case, shown as Figure 5-1, where three ultrafast fields (of the order of femtoseconds, ω_1, ω_2, ω_3) are incident on the TI and search for the response of the order of terahertz, δ. The study of four-wave mixing now becomes the problem of the third order nonlinear response. We assume that the photon mixing process is nearly phase matched, so that the generation of higher-order harmonics can be neglected. [170]

5.1.1 Current densitiy

The i^{th}-order current density is given by:

$$J_x^{(n)} = e\int d\mathbf{k} v_x^{(n)}\left[f(\varepsilon_k) - f\left(\varepsilon_k + \varepsilon_{ph}\right)\right], \tag{5-1}$$

where $f(\varepsilon)$ is the Fermi-Dirac distribution function, ε_{ph} is total energy of the incoming photons and k_B is the Boltzmann constant. The upper integration limit is equal to the Fermi energy μ at $T = 0$ K. At finite temperature, the upper limit is chosen as 2μ.

We consider an external field in the form of $\mathbf{E}(\mathbf{r},t) = \sum \mathbf{E}_i \exp[i\left(\mathbf{q}_i \cdot \mathbf{r} - \omega_\mu t\right)]$, where $\mathbf{E}_i$, $\mathbf{q}_i$ and ω_i are the amplitude, wavevector and frequency of the i-th wave of the electric field. The velocity of electrons in the bulk states along the direction of the electric field is given as $v_x = \partial\varepsilon_k/\partial k_x$. Without loss of general properties, we assume that the applied field is along the x-direction. Under the minimum coupling scheme, $k_x \to k_x - e\mathrm{A}_x(\mathbf{r},t)$, where $\mathrm{E}_x(\mathbf{r},t) = -\partial\mathrm{A}_x(\mathbf{r},t)/\partial t$. Hereafter, we define $\mathrm{u}_x = -e\mathrm{A}_x(\mathbf{r},t)$.

5.1.2 Third order velocity

The energy spectrum of the bulk state is:

$$E_k = C - D\left(k_x^2 + k_y^2\right) \pm s\sqrt{A^2\left(k_x^2 + k_y^2\right) + \left[M - B\left(k_x^2 + k_y^2\right)\right]^2}, \tag{5-2}$$

where $s = \pm 1$ indicates the valence and the conduction band respectively. The square-root term in Eq. (5-2) rendered the energy spectrum highly non-parabolic. In what follows, we shall show that this non-parabolic energy dispersion leads to a strong non-linear optical response in the TI bulk state.

$$\frac{\partial E}{\partial k_x} = -2D(k_x + u_x)$$

$$+\frac{A^2(k_x + u_x) - 2B(k_x + u_x)\left[M - B\left((k_x + u_x)^2 + k_y^2\right)\right]}{\sqrt{A^2\left((k_x + u_x) + k_y^2\right) + \left[M - B\left((k_x + u_x)^2 + k_y^2\right)\right]^2}}. \quad (5\text{-}3)$$

To study the nonlinear effect, we expand the group velocity in terms of the external electric field. Up to third order of the electric field, it can be shown that the velocity components are given as:

$$v_x^{(0)} = -2Dk_x + \frac{Rk_x}{\sqrt{F}}, \quad (5\text{-}4)$$

$$v_x^{(1)} = -2Du_x + \frac{RF + (4B^2F - R^2)k_x^2}{F\sqrt{F}}u_x, \quad (5\text{-}5)$$

$$v_x^{(2)} = \frac{3R(R^2 - 4FB^2)k_x^3 + 3F(4B^2F^2 - R^2)k_x^2}{2F^2\sqrt{F}}u_x^2, \quad (5\text{-}6)$$

$$v_x^{(3)} = G(k_x)u_x^3. \quad (5\text{-}7)$$

Here we have used the shorthand notations:

$$R = A^2 - 2MB + 2B^2k^2,$$

$$F = (Bk^2 - M)^2 + A^2k^2,$$

$G(k_x)$

$$= \frac{(4FB^2 - 5R^2)(R^2 - 4FB^2)k_x^4 + 2FR(3R^2 - 12B^2F)k_x^2 + (4B^2F - R^2)F^2}{2F^3\sqrt{F}}.$$

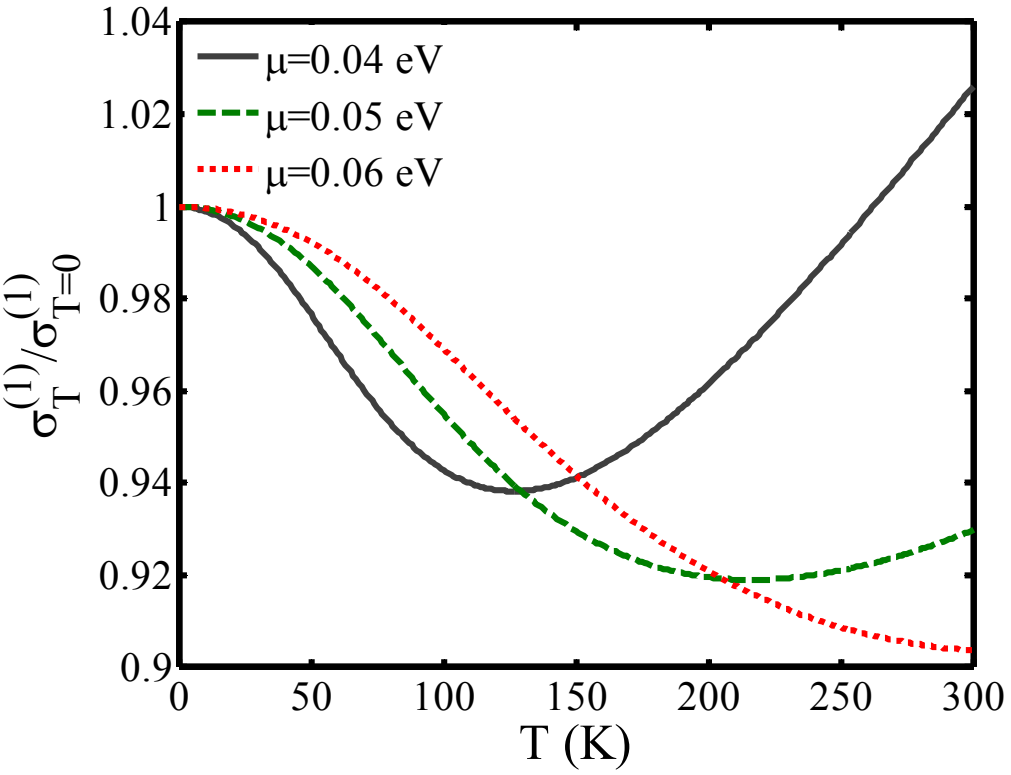

Figure 5-2. Temperature dependence of the first order conductivity at chemical potentials of 0.04 eV, 0.05 eV, and 0.06 eV. The excitation frequency of the photons is ω = 100 THz.

5.1.3 Conductivity

Due to time reversal symmetry (TRS) in the TI, the second order velocity does not contribute to the current density. For $\omega_1 = \omega + \delta_1$, $\omega_2 = \omega + \delta_2$ and $\omega_3 = 2\omega$, the third order current at $\omega_1 + \omega_2 - \omega_3 = \delta_1 + \delta_2 = \delta$ is given as

$$J_x^{(3)} = i\frac{e^4 E_1 E_2 E_3}{\omega_1\omega_2\omega_3}\int_0^{2\pi} d\theta \int_0^{2\mu} kdkG(k_x)[f(\varepsilon_k) - f(\varepsilon_k + \delta)]. \qquad (5\text{-}8)$$

5.2 Results and discussion

Figure 5-2 plots the first order conductivity as a function of temperature with different chemical potentials. We choose the excitation frequency as 100 THz, and all the curves are normalized with respect to zero temperature. It is obvious that the linear conductivity decreases at low temperature to a minimum value and then increases with higher temperature. The minimum points vary corresponding to the level of doping. The thermal effects, however, should be relatively small, as the scale of variation is less than 1%, which suggests that the temperature does not contribute much to the linear response.

Figure 5-3 shows the temperature dependence of the third order current $J^{(3)}(\delta)$. The frequencies of the three incident photons are chosen to be ω = 100 THz and δ = 1 THz. Since the reported carrier density in HgTe/CdTe QWs varies over a wide range from 2 - 40 × 10^{11} cm^{-2},[172] we choose a range of chemical potential, from 0.04 eV to 0.06 eV, to show the influence of the carrier concentration on the third order current. We set the amplitude of the three fields to be the same. There exists an optimal temperature around 50 K at which the mixing efficiency is greatest. At low temperature, only those carriers in a small region of δ below the Fermi surface contribute to $J^{(3)}(\delta)$. As the temperature increases, more carriers contribute to $J^{(3)}(\delta)$. Further increasing the temperature causes more low energy carriers to conduct. Due to the unique band structure of the TI, the third order velocity given in Eq. (5-8) is positive at high energy and negative at low energy. As a result, at high temperatures, $J^{(3)}(\delta)$ decreases with temperature.

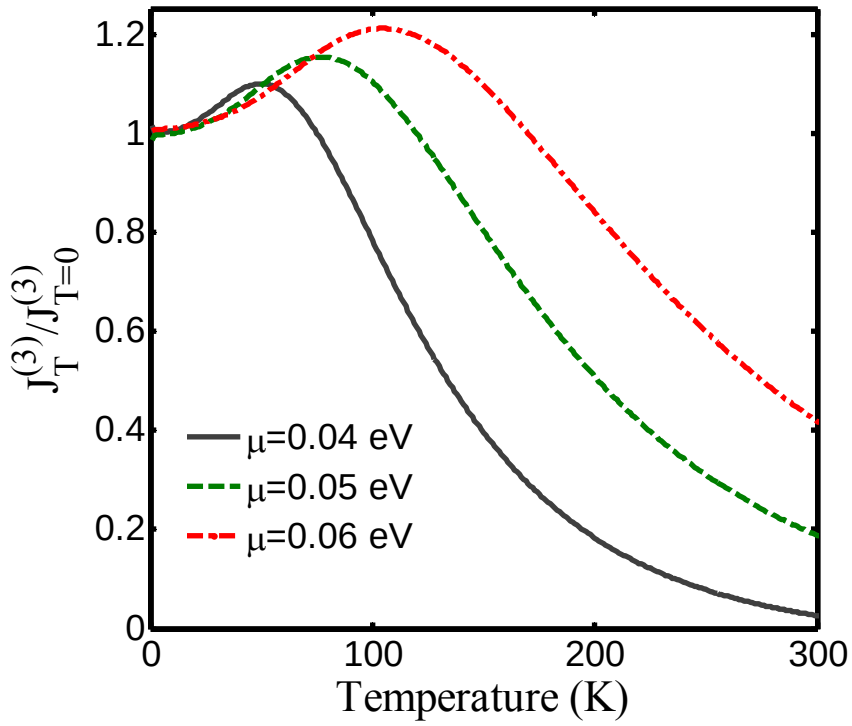

Figure 5-3 Temperature dependence of the third order current at various chemical potentials. The electric field is 10^4 V/cm, and the excitation frequency of the photons is ω = 100 THz.

In Figure 5-4, we plot the ratio of the third order current to the linear current as a function of the frequency difference δ at zero temperature. In response to the three fields, there are three linear currents of equal amplitude oscillating at ω_1, ω_2 and ω_3. In calculating $J^{(3)}(\delta)/J^{(1)}$, we choose the one oscillating at ω_1 as $J^{(1)}$. Under an electric field of 10^4 V/cm, $J^{(3)}(\delta)$ has a magnitude of around 10^{-4} of that of the linear current, suggesting that the terahertz generation efficiency of the TI from the femtosecond laser is comparable to or slightly better than that from the nonlinear semiconductor crystal commonly used in terahertz generation. The nonlinear current increases approximately as δ^2 at low δ. This can be understood from the phase space analysis.

At zero temperature, the available carrier number contributing to the linear current is nearly constant since ω is much larger than μ and nearly all electrons in the conduction band can conduct. The available carrier number contributing to the nonlinear current is directly proportional to δ. The average energy of each photo excited carrier in the final state is also δ. As a result the nonlinear current increases approximately as δ^2.

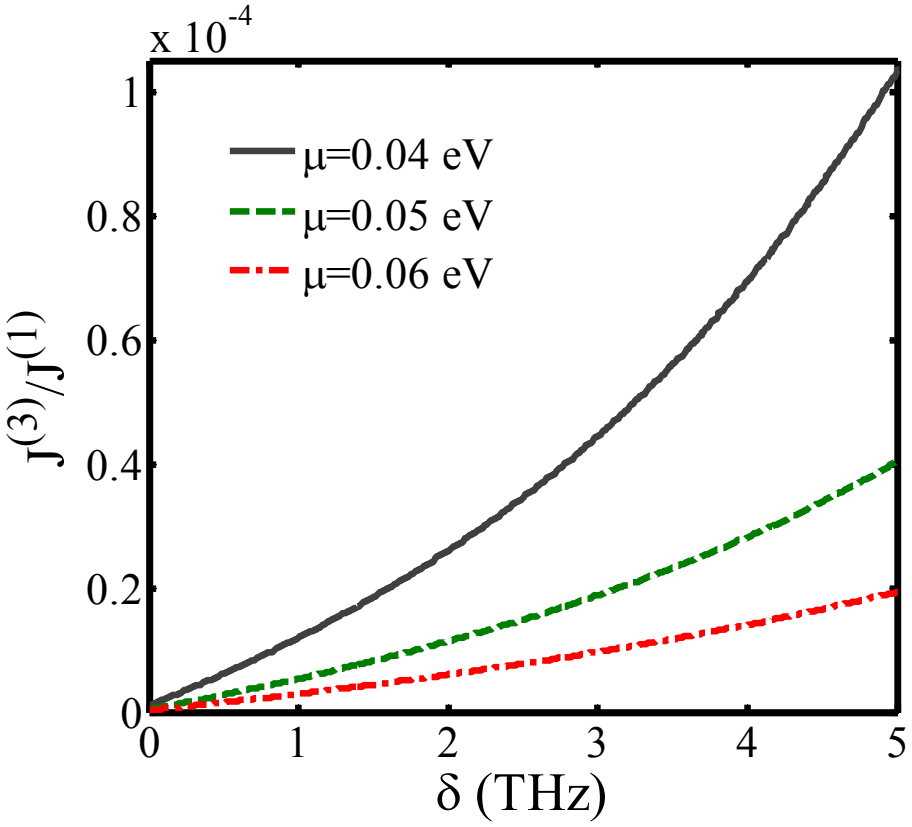

Figure 5-4. The ratio of the third order nonlinear optical response to the linear optical response versus the tuning frequency δ at various chemical potentials at zero temperature. The electric field is 10^4 V/cm, and the frequencies of the photons are ω = 100 THz, ω_3 = 200 THz.

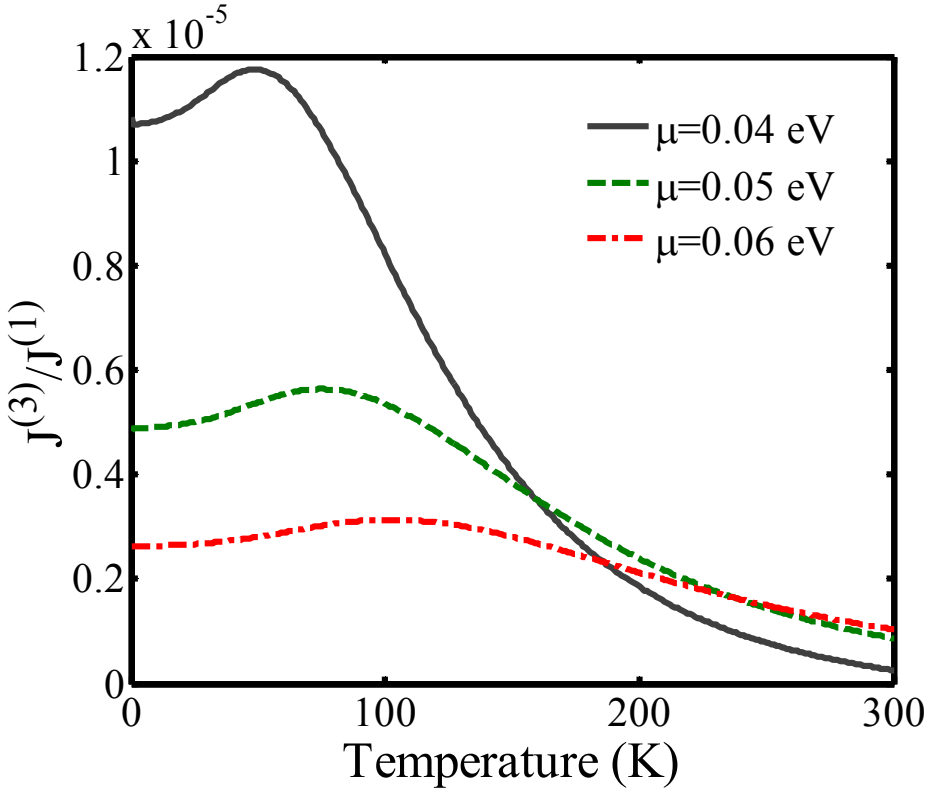

Figure 5-5 The ratio of the third order nonlinear optical response to the linear optical response as a function of temperature at various chemical potentials.

The temperature dependent nonlinear response at δ = 1 THz in Figure 5-5 reveals that the thermal excitation has a much more significant impact on the non-linear response by comparing to the thermal influence behaviour of linear and nonlinear conductivity in Figure 5-2 and Figure 5-3, respectively. It is easy to see that the nonlinear response is stronger at low temperature and low doping level. This is because, on the one hand, electrons are effectively confined around the Fermi level at low temperature, and on the other hand, the lower the doping level is, the more empty states remain in the conduction band above the Fermi level, which is of benefit for the excitation.

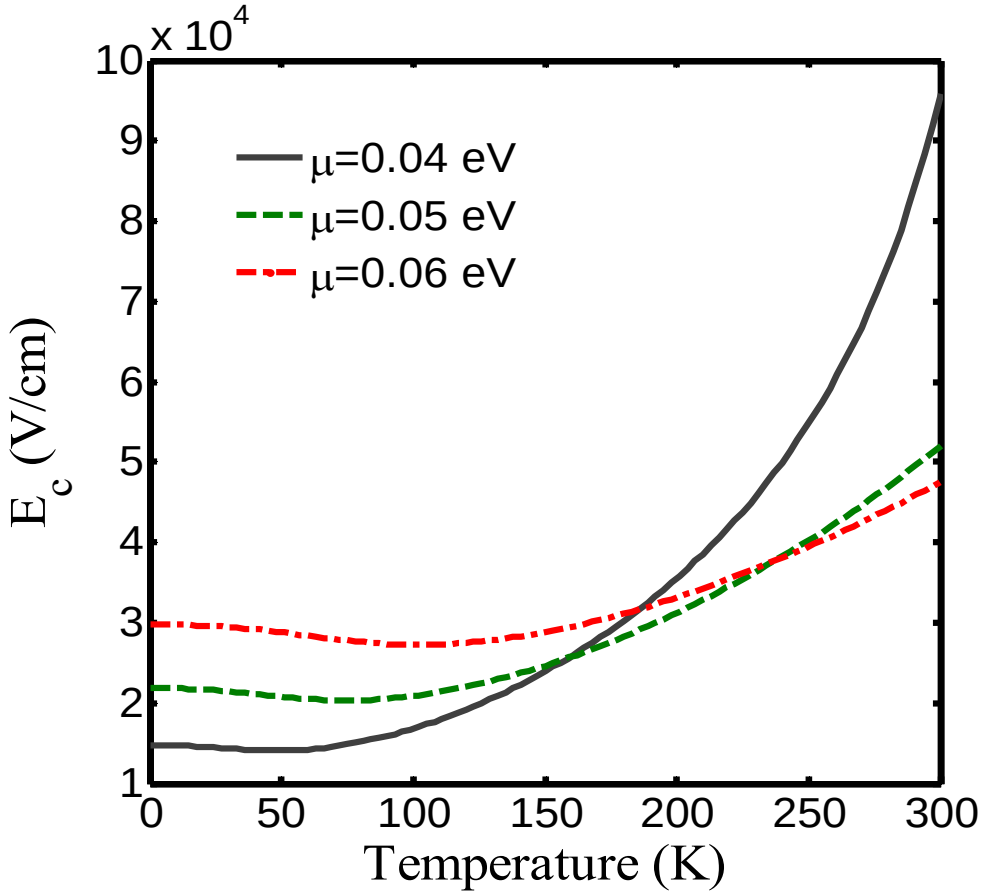

Figure 5-6. Temperature dependence of the critical electric field at various chemical potentials for $J^{(3)}(\delta)/J^{(1)}=10^{-5}$, ω = 100 THz, ω_3 = 200 THz and δ = 1THz.

A critical electric field can be defined to characterize the electric field strength required for the third order NOR to achieve a given conversion efficiency. Here we consider an efficiency of 10^{-5} and plot the critical field as a function of temperature in Figure 5-6. It can be seen that the critical field decreases very slowly for temperature below 100 K. This is due to the slow increase in the carrier numbers contributing to the nonlinear current. At high temperature the nonlinear current decrease rapidly with temperature, leading to a rapid increase in the critical field. In the present system where the nonlinear velocity is inversely proportional to the

energy of the carrier, the nonlinear term is generally stronger for low concentration sample at low temperatures and vice versa at high temperatures. This results in a crossover of the critical field from low temperature to high temperature.

5.3 Terahertz generation

Radiation of terahertz frequency has played a key role in many areas of future technology including medical diagnosis, security and materials. Exploring the efficient terahertz emitter is still the key challenge. The most common technique for producing low-power terahertz radiation is through nonlinear multiplication (frequency upconversion) of lower frequency oscillators.[173] Since the second-order non-linear susceptibility of the medium only occus in asymmetric structure crystals, the third-order nonlinear, which can become significant when the pump light is intense enough, is much easer to develop.[174, 175] Based on the modeling results we obtained above (in section 5.2), we consider a partial degenerate four-photon mixing process, where we let $\delta_1 = \delta_2$, and the frequency of terahertz emission is determined by $\delta = 2\delta_1$. This process is also known as third order nonliear three-wave mixing, but involves the interaction of four photons.[176] As shown in Figure 5-7(c),[177] a terahertz wave (with frequency denoted as ω_{THz}) is generated by the interation of two degenrated pump waves (with frequency denoted as ω_p) and a differnet frequency signal wave (with frequency denoted as ω_s) in the HgTe/CdTe QW nonlinear medium. The signal wave is fixed, while the pump wave is tunable. The wave meter is employed to determined the frequency of the photomixer radiation by monitoring the frequency difference of the two lasers to an accuracy of δ_1. The emitted terahertz radition will be collected by the Bolometer. To ensure that the experiments work well, two aspects have to be considered carefully: (i) the energy conseravtion law

$\omega_{THz} = 2\omega_p - \omega_s$, shown in Figure 5-7(a); (ii) the momentum conservation law $k_{THz} = 2k_p - k_s$, shown in Figure 5-7(b). In the real experiment, however, it is common to find that this process is accompanied with a nonlinear phase mismatch induced by self phase modulation and cross phase modulation, and a linear phase mismatch due to the dispersion.[178] And therefore, additional techniques may be need to improve the phase matching of the system presented in Figure 5-7(c).

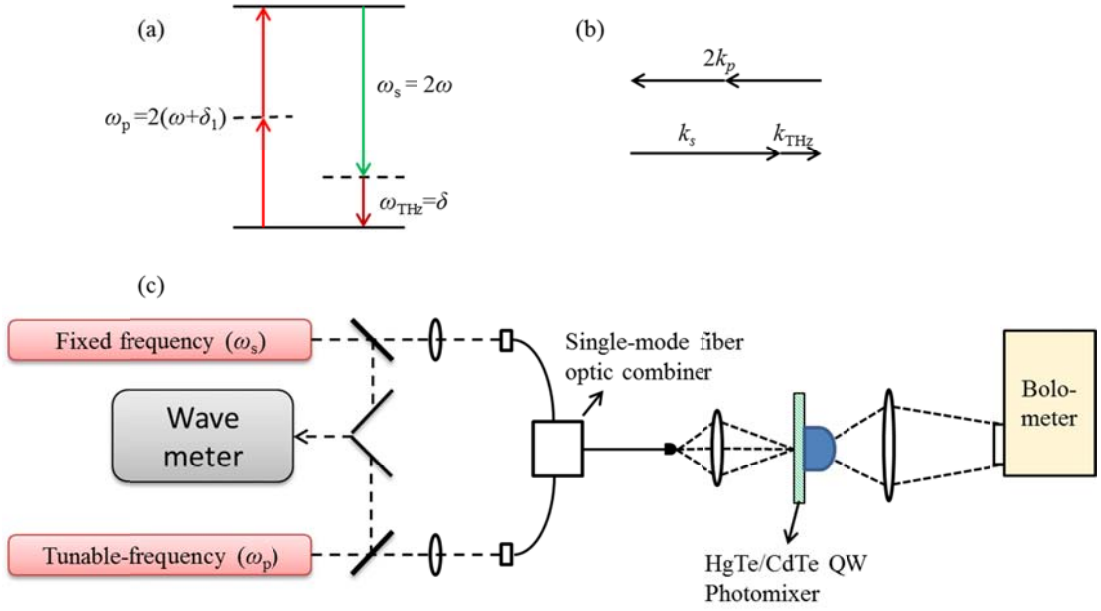

Figure 5-7. (a) Schematic of energy conservation diagram, (b) the phase-matching diagram, (c) the experiment configuration for terahertz radiation measurement[177].

In summary, we have shown that bulk states of the TI can also exhibit a stong photon mixing effect in the terahertz rgime under an electric field around 10^4 V/cm and a frequency of the order of femtoseconds. The conversion efficiency can be increased by a factor of 4 if the radiation frequencies are reduced to 50, 50 and 100

THz. Our results suggest that HgTe/CdTe QWs can be of potential use in device applications for nonlinear photon mixing. Since the gapless surface state in the TI is critically dependent on the thickness of the sample and the bulk state is much more robust, our finding is of particular interest for potential TI application in photonics and optics.

CHAPTER 6 SEMICLASSICAL STUDY OF NONLINEAR OPTICAL RESPONSE DUE TO THE INTRA-BAND TRANSISTIONS

The optical conductivity of HgTe/CdTe QWs has long been an interesting topic since the tuneable band gap can give rise to an optical response in the terahertz-far-infrared (FIR) regime, which is benefit for optoelectronic devices, especially, THz detectors and emitters.[179, 180] It has been demonstrated that HgTe/CdTe superlattices have significant nonlinear optical properties such as large $\chi^{(3)}$, a THz response and a high saturation threshold. In this paper, we will study the nonlinear response of HgTe/CdTe QWs with two types of band structure without breaking the nontrivial topological property.[181]

6.1 Formalism

The energy dispersion relation can be obtained:

$$\varepsilon_{\mathbf{k},s} = C - Dk^2 + s\sqrt{(M - Bk^2)^2 + A^2k^2}, \tag{6-1}$$

where $s = \pm 1$ determines the valence band and conduction band respectively. We will consider the bulk state with fixed M defining the gap and thus the inversion of the band structure. By varying the other parameters, the direct energy gap at k=0 can be transformed to an indirect one. We drop the term C, since it only shifts the over-all energy of the band structure without affecting the wave function. The other four parameters (A, B, D, and M) are listed in Table 6-1. It has been pointed out that the topologically nontrivial insulator cannot be adiabatically tuned to a trivial insulator as long as $\frac{M}{2B} > 0$. Therefore, we fix the values of M and B, changing the values of A

and *D* to obtain two different band structures, denoted as type I and type II, as shown in Figure 6-1.

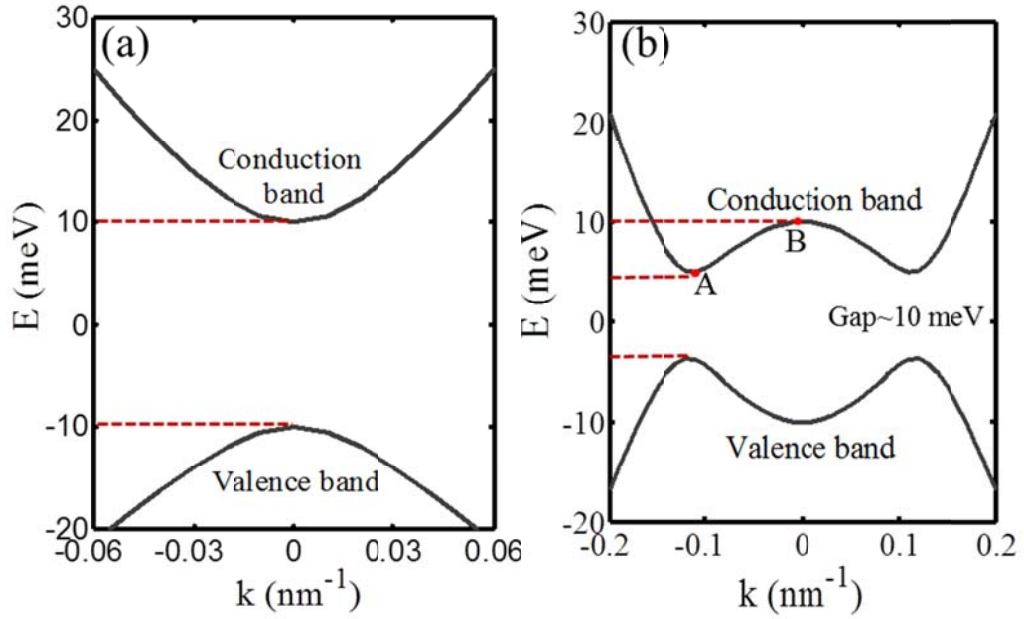

Figure 6-1. Two types of band structures in the small momentum regime: (a) direct-gap band structure, denoted as type I. The minimum gap is 20 meV. (b) Mexican hat band structure, denoted as type II. The minimum gap is about 10 meV, and the maximum gap is 20 meV.

Table 6-1. Values of parameters *A*, *B*, *D*, and *M*.

parameters	*A* (meV·nm)	*B* (meV·nm^2)	*D* (meV·nm^2)	*M* (meV)
TypeI[11]	364.5	-686	-512	-10
TypeII	36.45	-686	-51.2	-10

In the formalism, we assume that an *n*-type HgTe/CdTe QW under a time dependent electric field $\boldsymbol{E}(t) = \boldsymbol{E}_0 e^{i\omega t}$ along the *x* direction. In a homogenous system,

the electron distribution function, in the presence of scattering, can be derived from the Boltzmann equation:

$$\frac{\partial f}{\partial t} - \frac{\partial f}{\partial \mathbf{k}} \cdot e\mathbf{E} = -\frac{(f - f_0)}{\tau}, \tag{6-2}$$

where τ is the momentum relaxation time of electrons and holes due to impurity and phonon scattering. f_0 and f are the equilibrium and non-equilibrium Fermi distribution functions, respectively. f_0 has the form of:

$$f_0 = \frac{1}{1 + e^{\beta(\varepsilon_{\mathbf{k}} - \mu)}}, \tag{6-3}$$

where μ is the chemical potential, $\beta = k_B T$ with k_B the Boltzmann constant; and $\varepsilon_{\mathbf{k}}$ is the energy dispersion relation of HgTe/CdTe QW.

Defining $F_n = f - f_0$ and substituting $\frac{\partial F_n}{\partial t} = -in\omega F_n$ into Eq. (6-1), we obtain:

$$F_n = \frac{e\tau E_0}{1 - in\omega\tau} \frac{\partial F_{n-1}}{\partial k_x}, \tag{6-4}$$

with $n \geq 1$, and $F_0 = f_0$. Therefore, the current density is written as:

$$J^{(n)} = \frac{1}{2\pi^2} \int -e v_x F_n d\mathbf{k}. \tag{6-5}$$

$v_x = v_F \cos\theta$, where the Fermi velocity v_F is about 5.5×10^5 m/s. The conductivity is defined by:

$$J^{(n)} = \sigma^{(n)} E_0. \tag{6-6}$$

Substituting Eq. (6-5) into Eq. (6-6), the nth order optical conductivity along the x direction is:

$$\sigma^{(n)} = -\frac{e^2}{2\pi^2 \hbar} \frac{v_F \tau}{1 - in\omega\tau} \int_0^{2\pi} \cos\theta \, d\theta \int_0^{\infty} \frac{\partial F_{n-1}}{\partial k_x} k dk. \tag{6-7}$$

The HgTe/CdTe QW bulk state with fixed $M = -10$ meV has a big energy gap of about 20 meV for the one-gap case, and around 10 meV for the double-gap case,

both of which are significantly large at low frequency, which allows us to consider the intraband excitation only. The second order conductivity is always zero as long as the time reversal symmetry is preserved. Using $\frac{\partial f_0}{\partial k_x} = \frac{\partial f_0}{\partial k}\cos\theta - \frac{1}{k}\sin\theta\frac{\partial f_0}{\partial \theta}$, together with Eq. (6-4) and Eq. (6-7), the conductivity for the first order and third order can be written down:

$$\frac{Re\sigma^{(3)}}{Re\sigma^{(1)}} = \frac{3e^2\tau^2E_0^2}{4\hbar^2}\frac{(11\omega^2\tau^2-1)(1+\omega^2\tau^2)}{(1-11\omega^2\tau^2)^2+36(\omega^2\tau^2-\omega^4\tau^4)^2} \times \frac{\int_0^\infty\left(\frac{1}{k}\frac{\partial f_0}{\partial k}-\frac{\partial^2 f_0}{\partial k^2}-k\frac{\partial^3 f_0}{\partial k^3}\right)dk}{\int_0^\infty \frac{\partial f_0}{\partial k}kdk}; \tag{6-8}$$

$$\frac{Im\sigma^{(3)}}{Im\sigma^{(1)}} = \frac{9e^2\tau E_0^2}{2\hbar^2}\frac{(1-\omega^4\tau^4)}{(1-11\omega^2\tau^2)^2+36(\omega^2\tau^2-\omega^4\tau^4)^2} \times \frac{\int_0^\infty\left(\frac{1}{k}\frac{\partial f_0}{\partial k}-\frac{\partial^2 f_0}{\partial k^2}-k\frac{\partial^3 f_0}{\partial k^3}\right)dk}{\int_0^\infty \frac{\partial f_0}{\partial k}kdk}. \tag{6-9}$$

6.2 Results

Since the band structure is about k symmetry, the integral is taken over all k>0. At zero temperature, $\partial f_0/\partial k$ is simply a delta function $-\delta(k-k_F)$. The first order and third order conductivity, in Eq. (6-8) and Eq. (6-9) respectively, will be reduced to

$$\frac{Re\sigma^{(3)}}{Re\sigma^{(1)}} = \frac{3e^2\tau^2E_0^2}{4\hbar^2}\frac{(11\omega^2\tau^2-1)(1+\omega^2\tau^2)}{(1-11\omega^2\tau^2)^2+36(\omega^2\tau^2-\omega^4\tau^4)^2} \times \frac{\delta(k-k_{F1})-\delta(k-k_{F2})}{k^2\delta(k-k_F)}; \tag{6-10}$$

$$\frac{Im\sigma^{(3)}}{Im\sigma^{(1)}} = \frac{9e^2\tau E_0^2}{2\hbar^2}\frac{(1-\omega^4\tau^4)}{(1-11\omega^2\tau^2)^2+36(\omega^2\tau^2-\omega^4\tau^4)^2} \times \frac{\delta(k-k_{F1})-\delta(k-k_{F2})}{k^2\delta(k-k_F)}. \quad (6\text{-}11)$$

It is worth mentioning that when Fermi energy falls in between points A and B in Figure 6-1(b), the Delta function will have two solutions, k_{F1} and k_{F2}. We note that even at non-zero temperature, the contributions from the high order derivative terms in Eq. (6-9) are nearly zero. The dominant term $\partial f_0/\partial k$ at non-zero temperature is found to be:

$$\frac{\partial f_0}{\partial k} = \frac{1}{\beta}f_0(f_0-1)v(k), \quad (6\text{-}12)$$

$$v(k) = -2Dk + \frac{A^2-2BM+2B^2k^2}{\sqrt{A^2k^2+(M-Bk^2)^2}}k$$

where $v(k)$ is the velocity as a function of the k vector. It is obvious that the difference between third order and first order integration is merely the factors of $1/k$ and k. The scattering time is estimated from $\tau = \frac{\mu^* m^*}{e}$ = 0.57 ps with the bulk mobility $\mu^* \approx 10^5$ cm^2/(V s) and the effective mass at the bottom of the conduction sub-band $m^* \approx 0.01\ m_e$.[182] The electric field is fixed at 5000 V/cm. We plot the ratio of the real part of the third order conductivity to the first order conductivity as a function of frequency and chemical potential, respectively, at different temperatures.

6.3 Discussion

Figure 6-2 shows the frequency dependent ratio of the real part third order conductivity to the first order conductivity for type I and type II band structures, respectively, at four temperatures: 0 K, 4 K, 77 K and 300 K. An electric field of

5000 V/cm was applied for the numerical calculation. Within the frequency range considered, the nonlinear response dominates the first order linear conductivity, and the maximum responses are located at a frequency around 0.65 THz, which is independent of temperature and chemical potential. The nonlinear responses exhibit a dramatic drop toward higher frequency after the peak due to the enhancement of the linear response and the decrease in the third order nonlinear response.

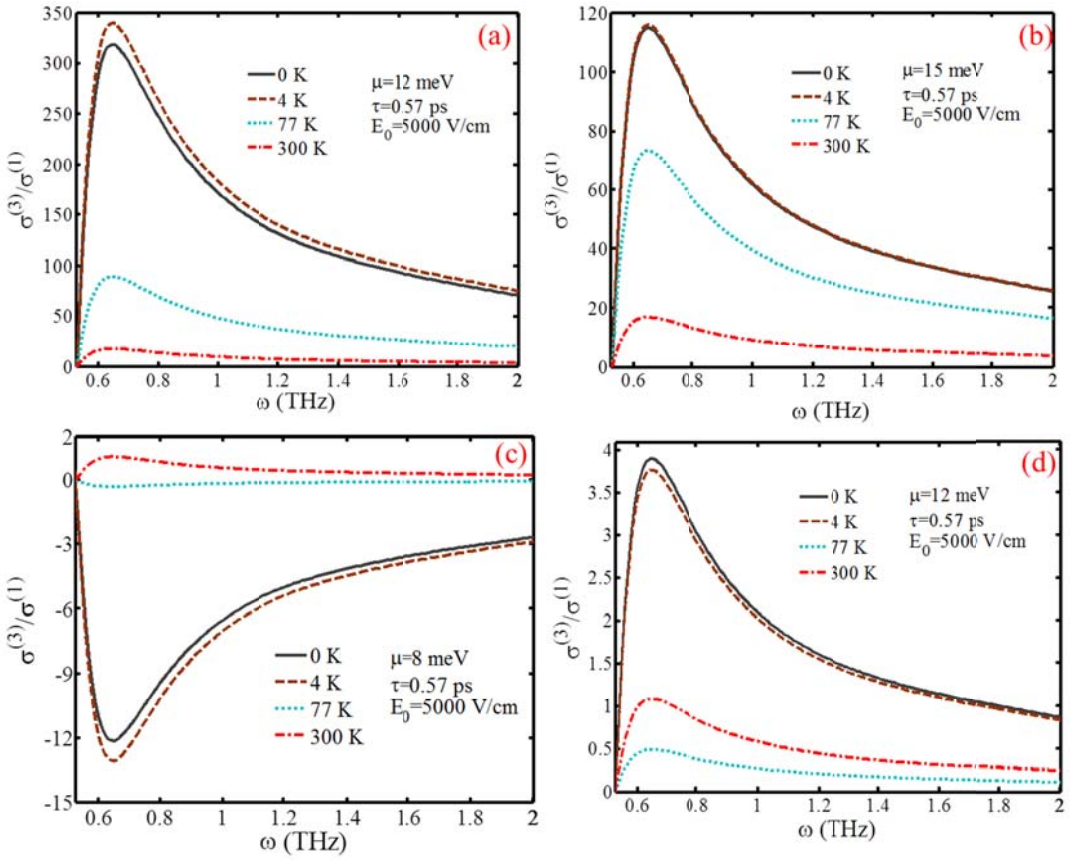

Figure 6-2. Ratio of the real part of the third order conductivity to the first order conductivity as a function of frequency. (a), (b) are from the type I case with μ equal to 12 meV and 15 meV, respectively. (c), (d) are from the type II case with values of μ equal to 8 meV and 12 meV, repectively.

When the band structure is deformed from type I to type II, the valence band is changed to a "Mexican hat" shape, and the minimum of the valence band moves to Point B. Now, we consider the case in the type II band structure with chemical potential lying between the "A" level and "B" level. The $\sigma^{(3)}/\sigma^{(1)}$ for μ = 8 meV is plotted in Figure 6-2(c). Since the linear response is always positive, the opposite sign of $\sigma^{(3)}/\sigma^{(1)}$ at low temperatures originates from the third order nonlinear response. This singular response happens only when the chemical potential lies far below the "A" level (10 meV) due to the anomalous response of the hole excitation close to Point A, where the density of states is much more condensed. When the temperature increase to 300 K, the electrons are thermally excited up above the Fermi level and redistributed by the Fermi-Dirac distribution function. As a result, the third order nonlinear response behaves in a similar way to the three other cases in Figure 6-2(a), (b), (d), for which the μ lies above 10 meV.

Negative conductance is a reflection of the amplification of the electromagnetic field, while positive conductance is related to the absorption. The sign changes of the third order nonlinear response suggests that by modifying the band structure or gating the chemical potential, the HgTe/CdTe QW can be designed as the gain medium of a laser for terahertz radiation. This is possible. It has been experimentally demonstrated that both the conduction band and valence band consisting of hole-type states can be obtained with well widths larger than 6.3 nm, which forms a 2D electron-hole system that no spatial separation is between the 2D electrons and 2D holes.[183] As a result, the self-consistent oscillations of electron and hole densities could occur under an appropriate external electric field, which could lead to terahertz emission.[184, 185]

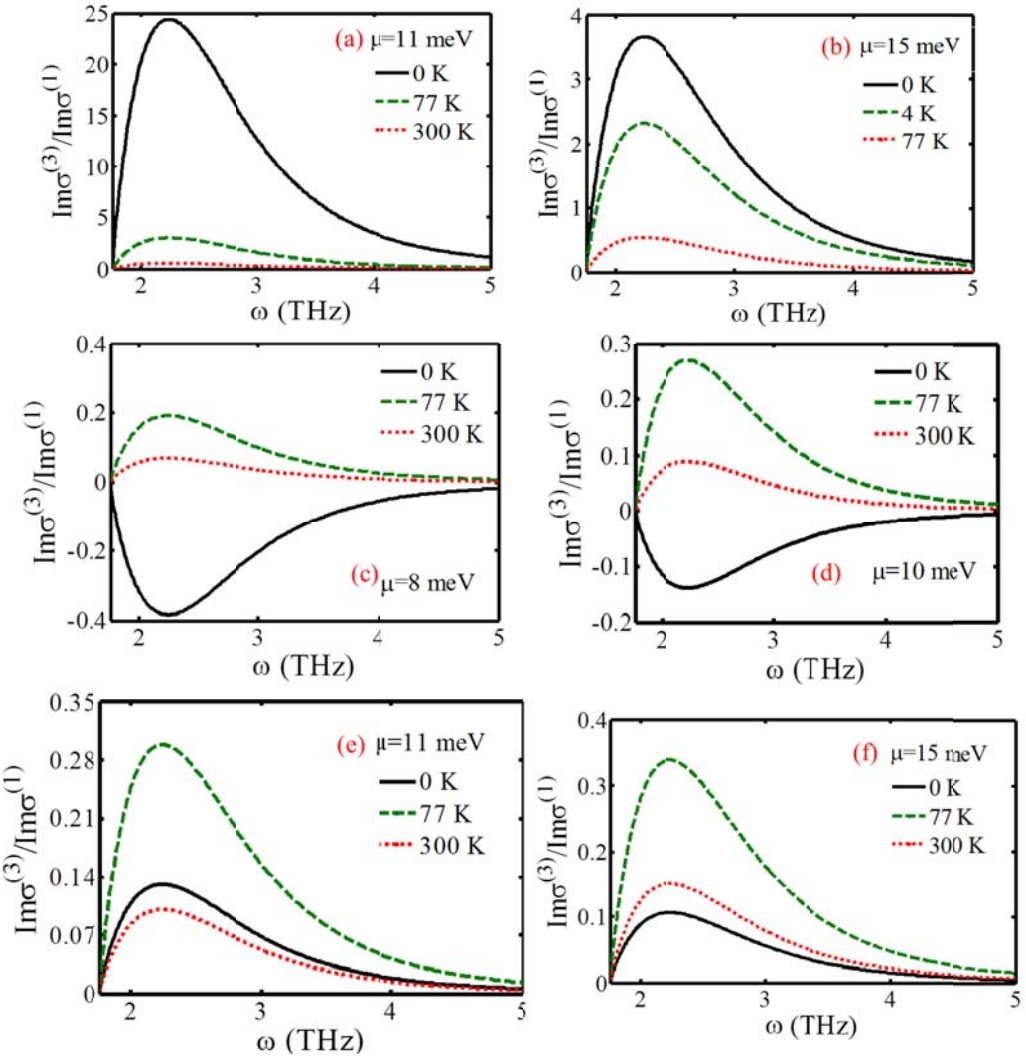

Figure 6-3. Ratio of the imaginary part of the third order conductivity to the first order conductivity as a function of frequency. (a), (b) are from the type I case with μ equal to 11 meV and 15 meV, respectively. (c)-(f) are from the type II case with values of μ equal to 8 meV, 10 meV, 11 meV and 15 meV, repectively.

Figure 6-3 presents the ratio of the imaginary part of third order conductivity to that of the first order conductivity as a function of frequency for type I and type II band structures, respectively. The imaginary part of the conductivity stand for the π/2 out-of-phase inductive current, e.g. the dispersion of plasmon polarition. We

defined the frequency cut-off at the frequency where the relation of $\omega\tau - 1 = 0$ in the numerator of the imaginary part of third order conductivity, which is different from that of the real part ($11\omega\tau - 1 > 0$) by comparing Eq. (6-8) and Eq. (6-9). We can also see that the structure of the curves, shown in figure 6-3, are pretty similar to that of real part conductivity except for the peaks shifting to higher frequency at around 2.25 THz, which is also independent of temperature and chemical potential.

Figure 6-4 presents the nonlinear response as a function of chemical potential corresponding to the two peak frequencies in Fig. 6-2. For type I in Figure 6-4(a), the ratio decreases with increasing chemical potential, which is ascribed to the reduced vector phase at higher energy levels, while in the type II band structure, as plotted in Figure 6-4(b), the nonlinear response is divided into two regimes regarding the position of μ. The ratio obviously increases in the regime where μ lies below Point A, after which the ratio turns sharply negative, and then slowly increases with the chemical potential. It is clear that at low temperature and small chemical potential, the third order conductivity dominates the first order conductivity.

Finally, we will discuss the thermal effect on the nonlinear response. As we can see from Figure 6-2 and Figure 6-4, the thermal effect causes a significant depression of the third order conductivity. At low temperature, only a small number of electrons are thermally excited in the valence band, and thus, the weak thermal excitation does not destroy too many valence band electrons, which is of benefit for the third order nonlinear conductivity. At higher temperature, the linear response increases rapidly, and other scattering processes, such as electron-phonon scattering, are involved due to the strong thermal excitation. Therefore, the ratio $\sigma^{(3)}/\sigma^{(1)}$ decreases dramatically.

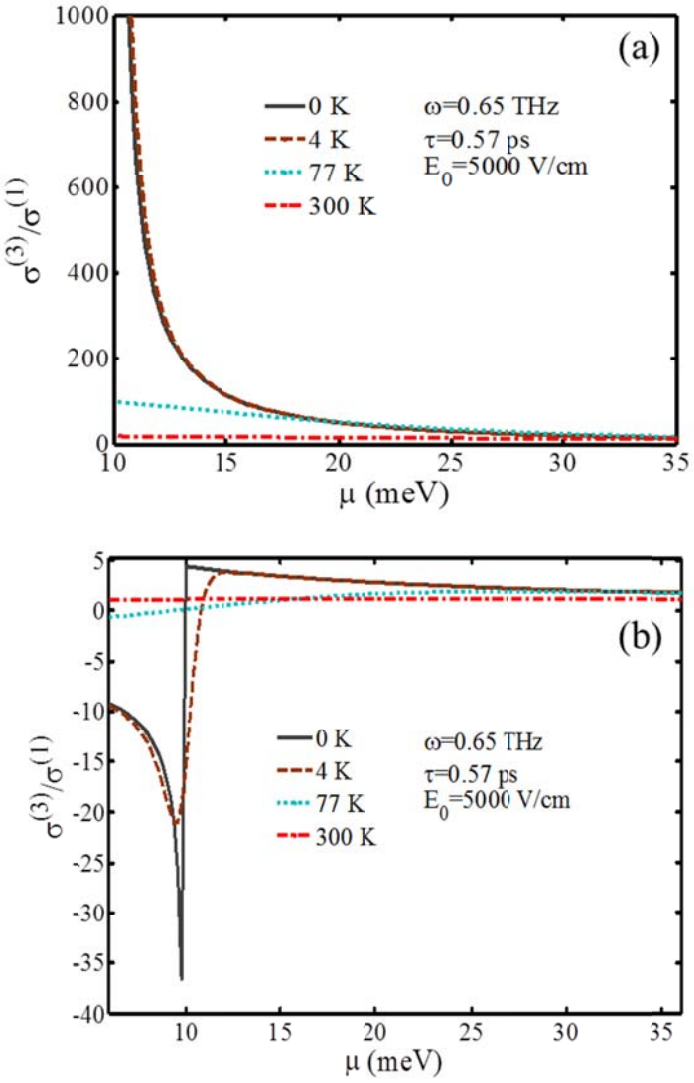

Figure 6-4. Nonlinear response as a function of chemical potential for two types of band structure, type I (a) and type II (b), at the peak frequency of 0.65 THz as shown in Fig. 6-2.

In conclusion, we calculated the ratio of the real part of the third order conductivity to the first order conductivity. The third order conductivity dominates in the low temperature regime with small chemical potential under an appropriate electric field. In both type I and type II band structures, thermal perturbation imposes

a negative influence on the third order nonlinear response, especially when μ is located below Point A in Figure 6-1,corresponding to an energy level of 10 meV in the type II band structure. Our studies suggest a potential application of HgTe/CdTe in nonlinear photonics and optoelectronics devices in both light emission and amplification.

CHAPTER 7 QUANTUM MECHANIC STUDY OF NONLINEAR OPTICAL RESPONSE DUE TO INTER-BAND TRANSISTIONS IN THE SURFACE STATES

Without a magnetic field, the surface state of the 3D TIs is gapless. In this case, the optical response in the low energy regime can occur without considering the bulk effect since the bulk band gap is of the order of 300 meV, or 75 terahertz (THz). Therefore, the surface of a 3D TI can be analogized as 2D graphene which has been proposed as a promising terahertz emitter and detector. X. Zhang et al.[112] reported that the low-energy optical absorbance of the topological surface states of Bi_2Se_3 film is $\pi\alpha/2$, just half the value of single-layer graphene where α is the fine-structure constant.

In this Chapter, we calculate the third order nonlinear optical conductance of Bi_2Se_3 crystals or thin films under a time-dependent electric field. We show that the surface states of the TI exhibit a strong nonlinear response involving three photons in the low energy regime. This model is also valid for other strong 3D TIs.

7.1 Modelling

In the low energy regime, the effective Hamiltonian of the surface state of a TI is given by Ref. [53]:

$$H_{surf} = A_2 \begin{pmatrix} 0 & p_- \\ p_+ & 0 \end{pmatrix}, \tag{7-1}$$

where $p_\pm = p_x \pm i p_y$, $A_2 = \hbar v_F$. For Bi_2Se_3, A_2 =4.1 eV·Å.[10] We make two assumptions here. First, the bulk carrier density is low enough to allow only the surface states to

be considered. Second, the Bi_2Se_3 crystals or thin films are thick enough that the interactions among electrons from the top and bottom surface can be ignored.

Under an external electric field $E(t) = E_0 e^{i\omega t}$, the direction is along the *x*-axis, Eq (7-1) can be written as:

$$H_{surf} = A_2 \begin{pmatrix} 0 & p_- + eA_- \\ p_+ + eA_+ & 0 \end{pmatrix}. \tag{7-2}$$

Here, $A_\pm = A = \frac{E}{i\omega} e^{-i\omega t}$, and the wave function can be expanded in terms of two spinor components, $\alpha_n(\mathbf{p})$ and $\beta_n(\mathbf{p})$:

$$\Psi(\mathbf{p}, n) = \sum_{n=0}^{\infty} \begin{bmatrix} \alpha_n(\mathbf{p}) \\ \beta_n(\mathbf{p}) \end{bmatrix}. \tag{7-3}$$

With Eq (7-2) and Eq (7-3), we can solve the time-dependent Schrödinger equation $i\hbar\partial\psi/\partial t = H\psi$, and obtain two recursion equations for $\alpha_n(p)$ and $\beta_n(p)$:

$$\alpha_n(\mathrm{p}) = A \frac{\alpha_{n-1}(\mathbf{p}) p_+ + (p - n\omega)\beta_{n-1}(\mathbf{p})}{n\omega(n\omega - 2p)}; \tag{7-4}$$

$$\beta_n(\mathbf{p}) = A \frac{\beta_{n-1}(\mathbf{p}) p_- + (p - n\omega)\alpha_{n-1}(\mathbf{p})}{n\omega(n\omega - 2p)}. \tag{7-5}$$

These two equations recursively couple the *n* photon processes to the *n*-1 photon processes. The *n*th order total current can be calculated with the following equation:

$$\mathbf{J}_l^{(n)} = \frac{1}{4\pi^2} \int d\mathbf{p} \mathbf{j}_l^{(n)} N_T(\varepsilon). \tag{7-6}$$

Here:

$$N_T(\varepsilon) = n_F(-\varepsilon) - n_F(\varepsilon) = \tanh \frac{\varepsilon}{2k_B T}, \tag{7-7}$$

$$\mathbf{j}_l^{(n)} = e\Psi^* v_l \Psi / \tag{7-8}$$

$v_l = \partial H / \partial p_l$ is the current operator with $l = x, y$.

$$\mathbf{j}_x^{(n)} = e\Psi^* \frac{\partial H}{\partial p_x}\Psi, \tag{7-9}$$

$$\begin{aligned}
&\Psi^* \frac{\partial H}{\partial p_x}\Psi \\
&= \sum_0^{n'} (\alpha_{n'}^*(\mathbf{p}) \quad \beta_{n'}^*(\mathbf{p})) \begin{pmatrix} 0 & p_- + eA_- \\ p_+ + eA_+ & 0 \end{pmatrix} \sum_0^{n} \begin{pmatrix} \alpha_n(\mathbf{p}) \\ \beta_n(\mathbf{p}) \end{pmatrix} \\
&= v_F \sum_0^{n'} \sum_0^{n} [\beta_{n'}^*(\mathbf{p}) \quad \alpha_{n'}^*(\mathbf{p})] \begin{bmatrix} \alpha_n(\mathbf{p}) \\ \beta_n(\mathbf{p}) \end{bmatrix} \\
&= v_F \sum_0^{n} [\alpha_i^*(\mathbf{p})\beta_{n-i}(\mathbf{p}) + \alpha_{n-i}(\mathbf{p})\beta_i^*(\mathbf{p})].
\end{aligned}$$

By simplifying the Hamiltonian, the *n*th order current can be written as:

$$J^{(n)} = Re\frac{1}{2\pi^2}\int N(\varepsilon) p dp d\theta \left[\sum_{i=0}^{n} \alpha_i^*(\mathbf{p})\beta_{n-i}(\mathbf{p}) + \alpha_{n-i}(\mathbf{p})\beta_i^*(\mathbf{p})\right],$$

$$J^{(n)} = \frac{1}{2\pi^2}\int N(\varepsilon) p dp d\theta \; Re\left[\sum_{i=0}^{n} \alpha_i^*(\mathbf{p})\beta_{n-i}(\mathbf{p}) + \alpha_{n-i}(\mathbf{p})\beta_i^*(\mathbf{p})\right]. \tag{7-10}$$

When the electric field is absent, only $n = 0$ terms of Eq (7-4) and Eq (7-5) are nonzero. We obtain the result that $\alpha_0(\boldsymbol{p}) = 1/\sqrt{2}$ and $\beta_0(\boldsymbol{p}) = p_-/\sqrt{2}p$ by solving the Schrodinger equation with the Hamiltonian in Eq. (7-2). With these two initial spinor components, we can write down higher orders of α_n and β_n, which, for n=1, 2, and 3, can be expressed as follows:

$$\alpha_1 = \frac{A}{\sqrt{2}p\omega(\omega - 2p)}(pp_- + p_+ - \omega p_+), \tag{7-11}$$

$$\beta_1 = \frac{A}{\sqrt{2}p\omega(\omega - 2p)}(p_+^2 + p^2 - \omega p), \tag{7-12}$$

$$\alpha_2 = \frac{A^2[2p^3 - 4\omega p^2 + pp_+^2 + pp_-^2 + 2\omega^2 p_+^2]}{4\sqrt{2}p\omega^2(\omega - p)(\omega - 2p)}, \tag{7-13}$$

$$\beta_2 = \frac{A^2[2p_+p^2 + p_-p^2 - 2\omega p_-p - 4\omega p_+p + p_+^3 + 2\omega^2 p_+]}{4\sqrt{2}p\omega^2(\omega - p)(\omega - 2p)}, \tag{7-14}$$

$$\alpha_3 = \frac{A^3}{12\sqrt{2}p\omega^3(\omega - p)(3\omega - 2p)(\omega - 2p)}[3p_-p^3 + 3p_+p^3 + p_-^3p$$

$$+p_+^3p - 12\omega p_+p^2 - 9\omega p_-p^2 + 14\omega^2 p_+p + 8\omega^2 p_-p - 6\omega^3 p_+ - 3\omega p_+^3], \tag{7-15}$$

$$\beta_3 = \frac{A^3}{12\sqrt{2}p\omega^3(\omega - p)(3\omega - 2p)(\omega - 2p)}[3p^4 - 12\omega p^3 + 14\omega^2 p^3$$

$$+3p_+^2p^2 + 3p_+^2p^2 + p_-^2p^2 - 6\omega^3 p - 9\omega p_+^2 p - 3\omega p_-^2 p + 8\omega^2 p_+^2 + p_+^4]. \tag{7-16}$$

The first order total current is linear, and can be calculated by putting Eq. (7-11) and Eq. (7-12) back into Eq.(7-10).

$$\begin{aligned} J_1 &= \frac{e}{2\pi^2}\int N(\varepsilon)pdpd\theta Re(\alpha_0^*\beta_1 + \beta_0^*\alpha_1 + \alpha_1^*\beta_0 + \beta_1^*\alpha_0\ ) \\ &= \frac{e^2E}{4\hbar}N\left(\frac{\omega}{2}\right)e^{i\omega t}. \end{aligned} \tag{7-17}$$

The result for $J^{(1)}$ is very similar to that for graphene, which implies that the surface state of a TI can be treated as 2D graphene, except that there is only a single Dirac cone at the TI surface. It has been learnt that the universal conductance of a TI is $\sigma_0 = 2e^2/\hbar$. As a result, the first order conductivity can be expressed in the unit of σ_0, $\sigma_1 = \sigma_0 N(\omega/2)/8$. The second order current vanishes due to the time-reversal symmetry.

The third order current was calculated by combining Eqs. (7-15) and (7-16)

$$\begin{aligned} J_3 = \frac{e}{2\pi^2}\int N(\varepsilon)pdpd\theta \\ \cdot Re(\alpha_0^*\beta_3 + \beta_0^*\alpha_3 + \alpha_1^*\beta_2 + \beta_1^*\alpha_2 + \alpha_2^*\beta_1 + \beta_2^*\alpha_1 + \alpha_3^*\beta_0 \\ + \beta_3^*\alpha_0\ ) \end{aligned} \tag{7-18}$$

$$= \frac{2e^2}{\hbar}\frac{e^2 v_F^2 E_0^3}{8\hbar^2\omega^4}\left[\frac{13}{48}N\left(\frac{\omega}{2}\right) - \frac{2}{3}N(\omega) + \frac{45}{48}N\left(\frac{3\omega}{2}\right)\right]e^{3i\omega t}$$

$$+ \frac{2e^2}{\hbar}\frac{e^2 v_F^2 E_0^3}{8\hbar^2\omega^4}2N(\omega)e^{i\omega t}.$$

It is worth pointing out that the third order non-linear process involves two different mechanisms[171, 186-189]: the term $e^{3i\omega t}$ corresponds to the process of three photon absorption, while the term $e^{i\omega t}$ corresponds to the process of simultaneously absorbing two photons and emitting one photon. Since the third order nonlinear response is the superposition of two distinct processes, we calculated the third order conductivity by taking the root mean square of the two third order processes:

$$\langle\sigma_3\rangle = \sigma_0\frac{e^2 v_F^2 E_0^3}{8\hbar^2\omega^4}\sqrt{\frac{1}{2}|N_3(3\omega)e^{3i\omega t} + N_3(\omega)e^{i\omega t}|^2}. \quad (7\text{-}19)$$

Here,

$$N_3(3\omega) = \frac{13}{48}N\left(\frac{\omega}{2}\right) - \frac{2}{3}N(\omega) + \frac{45}{48}N\left(\frac{3\omega}{2}\right), \quad (7\text{-}20)$$

$$N_3(\omega) = 2N(\omega).$$

7.2 Results and discussion

The frequency dependence of the mean nonlinear conductance in the unit of σ_0 is plotted in Figure 1-1. The electric field was fixed at 1000 V/m. The nonlinear responses decrease exponentially with increasing frequency. For frequencies higher than 2 THz, the nonlinear response becomes weak even at low temperature. The frequency of the external excitation field plays a more important role than that of temperature since it is inversely biquadratically proportional to the third order total current.

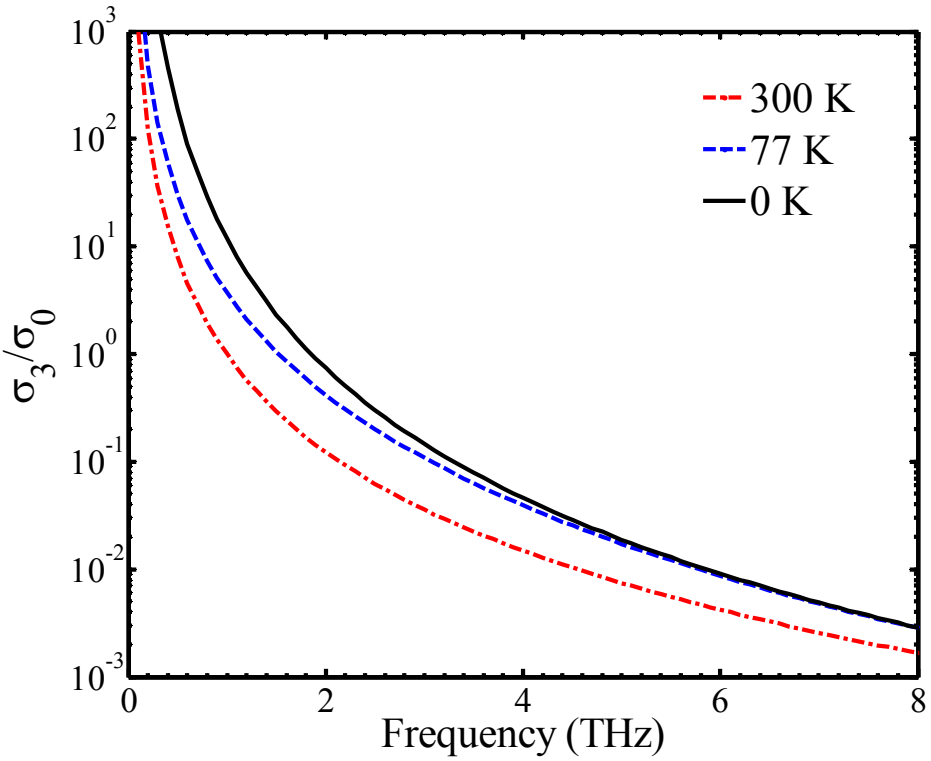

Figure 7-1. Frequency dependent nonlinear conductance in the unit of σ_0 at 0 K, 77 K, and 300 K.

Figure 7-2 shows a comparison between the first order linear optical conductance σ_1 and the third order mean nonlinear conductance σ_3 in the unit of σ_0 from 0 K to 300 K. The two conductances are normalized by their respective zero temperature values under an electric field of 260 V/cm with frequency of 1 THz. Both conductances show a steady drop with temperature up to 100 K, and then decrease slowly at higher temperature. It is noteworthy that the nonlinear conductance σ_3 is consistently above the linear conductance σ_1 over the whole temperature range, which suggests that the strong nonlinear effects are detectable even at a relatively weak electric field.

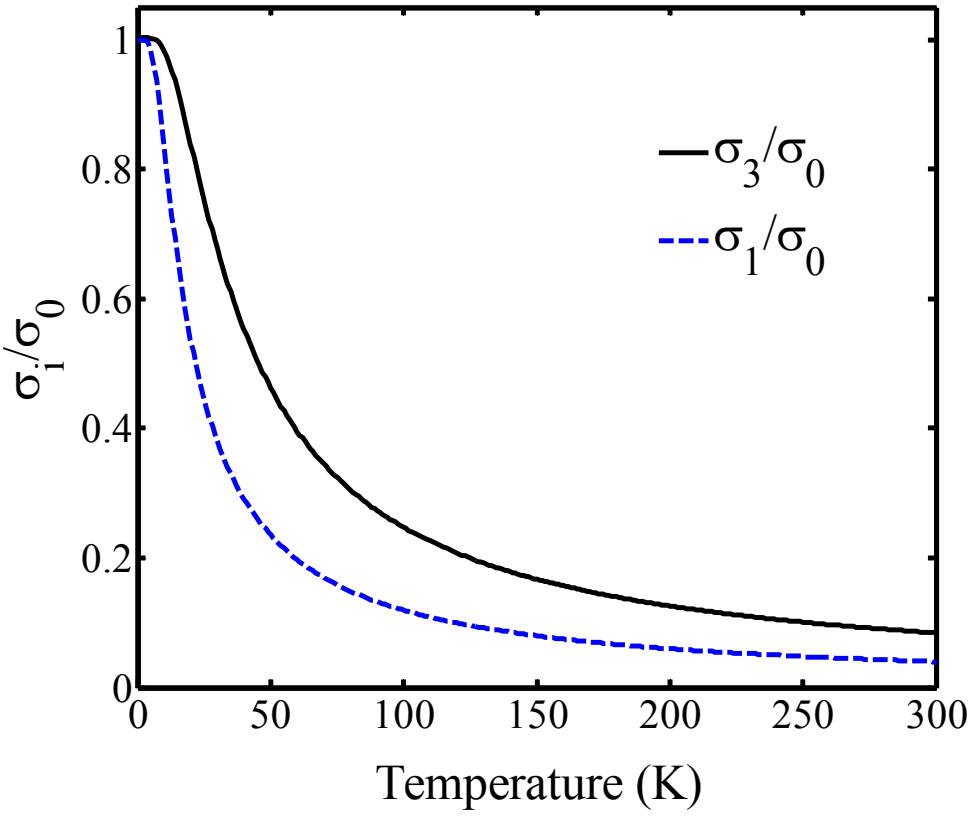

Figure 7-2. Temperature dependence of the nonlinear and linear conductance in the unit of σ_0 at a field of 260 V/cm and a frequency of 1 THz.

We introduce a critical field E_c such that above E_c the nonlinear conductance dominates over the linear conductance. The frequency dependency of E_c is shown in Figure 7-3(a). A stronger critical field is needed for a nonlinear optical effect at higher frequencies. At f = 1 THz, the values of E_c are 260 V/cm at 0 K, 3340 V/cm at 77 K, and 2500 V/cm at 300 K. These critical field strengths are accessible in a laboratory. Even for f = 5 THz at 300 K, the critical field strength 59000 V/cm can still be achieved in a laboratory, which is less than the phase transition field of the anti-ferroelectric (AFE) – ferroelectric (FE) transition reported in 0.94 $Na_{0.5}Bi_{0.5}TiO_3$-0.06$BaTiO_3$.[22] In a real experiment, however, such a high electric

field may damage the surface states. We suggest that the experiments should be carried out in the low frequency regime.

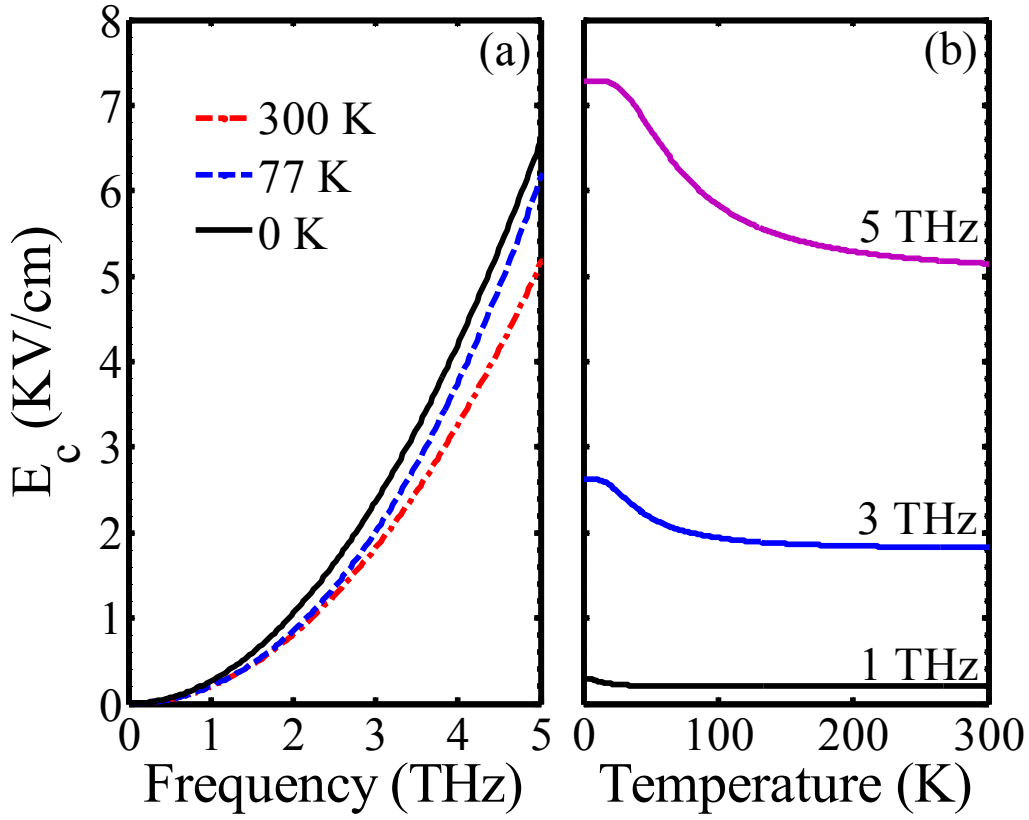

Figure 7-3. (a) Frequency dependence of the critical electric field E_c at various temperatures. (b) Temperature dependence of the critical electric field at various frequencies.

In Figure 7-3(b), we present the temperature dependence of E_c. The critical electric field strength is more affected by temperature at higher frequency than at lower frequency. At low temperature of $T < 20$ K, E_c is approximately constant since the weak thermal excitation is insufficient to influence the interband process in the THz regime. The low-T E_c-plateau is especially obvious at higher frequency since the carriers involved in the interband optical processes are 'deep' and are well-

protected from the thermal effect. At higher temperature, E_c decreases rapidly due to the more strongly reduced linear response at increasing temperature (see also Fig. 2).

For a fixed electrical field strength, there exists a threshold frequency ω_c defined by $\sigma_3/\sigma_1 = 1$. The frequency ω_c separates two regimes: for $\omega < \omega_c$ the nonlinear response dominates while for $\omega > \omega_c$ the linear response dominates. Figure 7-4 shows the temperature dependence of the threshold frequency. At very low temperature, the number of thermally excited electrons in the conduction band is low due to the vanishing density of states near the Dirac point and because the weak thermal excitation does not destroy too many valence band electrons. As a result, the linear and nonlinear responses are well-conserved and the threshold frequency ω_c is nearly temperature-independent. In the intermediate temperature regime, the thermal excitation exceeds the photon energy and the following effects simultaneously occur: (i) the conduction band is 'crowded' by thermally excited electrons; and (ii) the valence band electron population is thermally reduced. The combination of (i) and (ii) results in a reduced interband optical response. The three-photon process σ_3 involves 'deeper' electrons, however, and is less affected in comparison with the linear response. The overall stronger nonlinear response causes ω_c to increase with increasing temperature. At higher temperature, both linear and nonlinear responses are equally affected by the strong thermal excitation, and hence, ω_c remains constant.

Our results suggest that TI surfaces exhibit a rather strong nonlinear optical response in the THz frequency regime. It is worth to mention that our model consider that the system is in the absent of collisions, which would reduce the maximum conductivity at zero frequency due to the finite relaxation of electrons. In this case, the conductivity will decrease slowly with increasing frequency, since

collisions diminish the amount of kinetic energy of incident electrons by degrading it into thermal energy. However, this effect can happen at all frequencies, they introduce no striking frequency-dependent structure into the conductivity. Therefore, it is valid to neglect the relaxation rate as our aim is to obtain a qualitative understanding of the frequency-dependent behavior of conductivity of the metallic surface state of TIs.

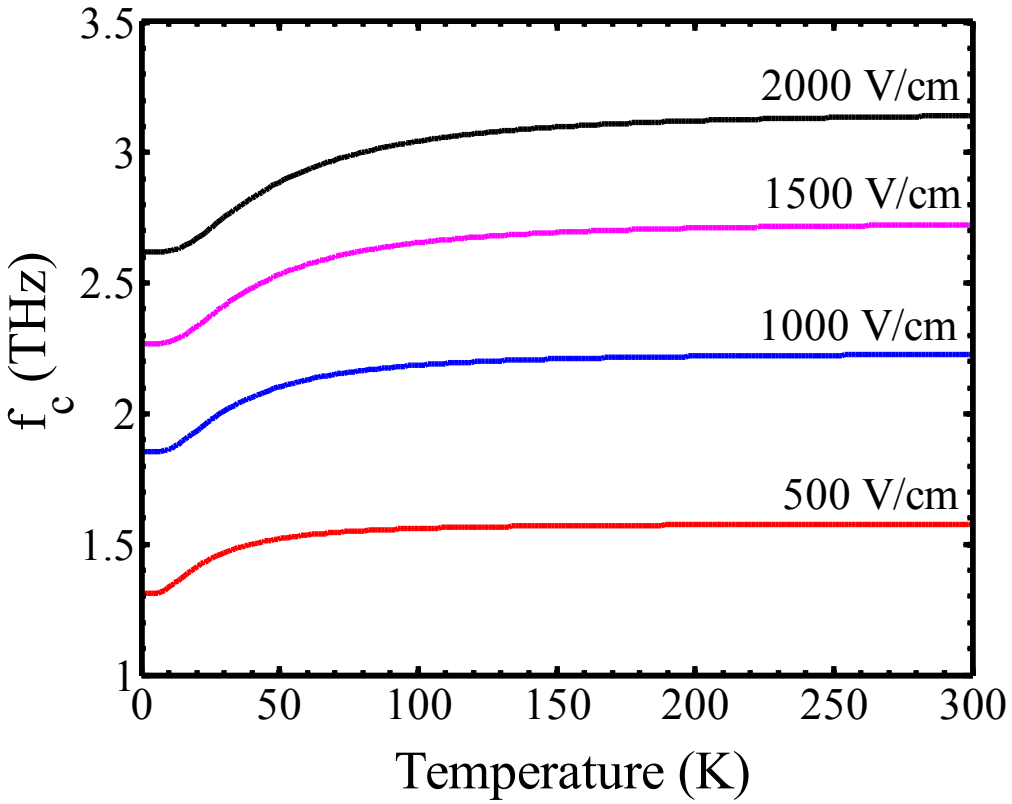

Figure 7-4. Threshold frequency versus temperature at different electric field strengths.

On the other hand, in real materials however, the free carriers from the bulk can absorb photons, causing fundamental optical responses. For Bi_2Se_3, the bulk carrier density is relatively high (~ $10^{18\text{-}19}$ cm^{-3}), as a result of Se charge vacancies. These

fundamental responses will lower the signal-to-noise ratio. Although the absorption of photons by free carriers is indirect, it is sensitive to the temperature, which produces thermal noise for the nonlinear effect. In a recent work by S. S. Hong et al.[115], progress has been made to reduce the carrier concentration to around 5×10^{16} cm^{-3} in Bi_2Te_2Se crystals. S. Jia et al.[24] have achieved a low carrier concentration of $\sim 2\times10^{11}$ cm^{-2} in Sb-doped Bi_2Se_3 nanoribbons. The low carrier concentration can effectively reduce the noise.

In conclusion, we have shown that the nonlinear optical response in gapless surface states of a 3D strong TI in the terahertz regime is significant. The band gap of the bulk is non-trivially large to a cut-off frequency of 75 THz and 25 THz for the linear and nonlinear responses, respectively. Such frequency cut-offs conveniently cover the entire useful THz frequency regime. With probable advances to reduce the carrier density of the bulk, 3D strong TIs have potential applications in THz nonlinear optics and photonics devices.

CONCLUSIONS

In the study of the energy loss rate of an electron in an *n*-type HgTe/CdTe QW, we found that, for slow electrons, the ELR is determined by the intraband contribution only, while for fast electrons, the ELR is dominated by the interband contribution. The mean inelastic scattering rate is in the terahertz frequency regime. At different energies, the incident electron can either diffuse resonantly, or almost be localized.

The dynamical conductivity has been investigated by using the quantum equation of motion for electron density matrix. We have calculated the frequency dependent conductivity of HgTe/CdTe QW in the presence of random impurity. Both the frequency dependence and the temperature dependence of the conductivity and the inverse scattering time are presented. The inverse transport scattering time decreases with the frequency in the low temperature regime and increases with the frequency in the high temperature regime. Our analysis is based on that the single particle scattering probability decreases with the frequency and that the number of electrons satisfying scattering condition at high temperature increase with the frequency.

We have shown that bulk states of TI can also exhibit a stong photon mixing effect in terahertz rgime under an electric field around 10^4 V/cm and frequency of the order of femtosecond. The conversion efficiency can be increased by a factor of 4 if the radiation frequencies are reduced to 50, 50 and 100 THz. Our results suggest that HgTe/CdTe QWs can be of potential use in device application for nonlinear photon mixing. Since the gapless surface state in TI is critically dependent on the

thickness of the sample and the bulk state is much more robust. Our finding is of particular intereting in potential application of TI in photonics and optics.

We calculated the ratio of real part third order conductivity over the first order conductivity. The third order conductivity dominates at low temperature regime with small chemical potential under an appropriate electric field. In both type I and type II band structures, thermal perturbation imposes a negative influences on the third order nonlinear response, especially when μ locates below "A" point corresponding to energy level of 10 meV in the type II band structure. Our studies suggest the potential application of HgTe/CdTe in nonlinear photonics and optoelectronics devices in both light emission and amplification.

Finally, we showed that the nonlinear optical response in gapless surface states of 3D strong TI in terahertz regime is significant. The band gap of the bulk is non-trivially large to a cut-off frequency of 75 THz and 25 THz for the linear and nonlinear responses, respectively. Such frequency cut-offs conveniently cover the entire useful THz frequency regime. With the probable advances to reduce the carrier density of the bulk, 3D strong TIs have potential applications in THz nonlinear optics and photonics devices.

REFERENCES

1. X. L. Qi and S. C. Zhang, Rev. Mod. Phys. **83** (4), 1057-1110 (2011).

2. M. Z. Hasan and C. L. Kane, Rev. Mod. Phys. **82** (4), 3045-3067 (2010).

3. L. Fu, C. L. Kane and E. J. Mele, Phys. Rev. Lett. **98** (10), 106803 (2007).

4. J. E. Moore and L. Balents, Phys. Rev. B **75** (12), 124306 (2007).

5. R. Roy, Phys. Rev. B **79** (19), 195321 (2009).

6. C. L. Kane and E. J. Mele, Phys. Rev. Lett. **95** (14), 146802 (2005).

7. Y. Xia, D. Qian, D. Hsieh, L. Wray, A. Pal, H. Lin, A. Bansil, D. Grauer, Y. S. Hor, R. J. Cava and M. Z. Hasan, Nat. Phys. **5** (6), 398-402 (2009).

8. D. Hsieh, Y. Xia, D. Qian, L. Wray, F. Meier, J. H. Dil, J. Osterwalder, L. Patthey, A. V. Fedorov, H. Lin, A. Bansil, D. Grauer, Y. S. Hor, R. J. Cava and M. Z. Hasan, Phys. Rev. Lett. **103** (14) (2009).

9. C. L. Kane and E. J. Mele, Phys. Rev. Lett. **95** (22), 226801 (2005).

10. B. A. Bernevig, T. L. Hughes and S. C. Zhang, Science **314** (5806), 1757-1761 (2006).

11. M. Fruchart and D. Carpentier, Cr. Phys. **14** (9-10), 779-815 (2013).

12. Y. Ando, J Phys. Soc. Jpn. **82** (10), 102001 (2013).

13. M. Konig, S. Wiedmann, C. Brune, A. Roth, H. Buhmann, L. W. Molenkamp, X. L. Qi and S. C. Zhang, Science **318** (5851), 766-770 (2007).

14. M. Konig, H. Buhmann, L. W. Molenkamp, T. Hughes, C. X. Liu, X. L. Qi and S. C. Zhang, J Phys. Soc. Jpn. **77** (3), 031007 (2008).

15. T. Zhang, P. Cheng, X. Chen, J. F. Jia, X. C. Ma, K. He, L. L. Wang, H. J. Zhang, X. Dai, Z. Fang, X. C. Xie and Q. K. Xue, Phys. Rev. Lett. **103** (26), 266803 (2009).

16. P. Deorani, J. Son, K. Banerjee, N. Koirala, M. Brahlek, S. Oh and H. Yang, Phys. Rev. B **90** (9), 094403 (2014).

17. A. M. Shuvaev, G. V. Astakhov, A. Pimenov, C. Brune, H. Buhmann and L. W. Molenkamp, Phys. Rev. Lett. **106** (10), 107404 (2011).

18. X. L. Wang, Y. Du, S. X. Dou and C. Zhang, Phys. Rev. Lett. **108** (26), 266806 (2012).

19. D. Kim, P. Syers, N. P. Butch, J. Paglione and M. S. Fuhrer, Nano. Lett. **14** (4), 1701-1706 (2014).

20. P. Di Pietro, M. Ortolani, O. Limaj, A. Di Gaspare, V. Giliberti, F. Giorgianni, M. Brahlek, N. Bansal, N. Koirala, S. Oh, P. Calvani and S. Lupi, Nat. Nanotechnol. **8** (8), 556-560 (2013).

21. M. Veldhorst, M. Snelder, M. Hoek, T. Gang, V. K. Guduru, X. L. Wang, U. Zeitler, W. G. van der Wiel, A. A. Golubov, H. Hilgenkamp and A. Brinkman, Nat. Mater. **11** (5), 417-421 (2012).

22. L. Fu and C. L. Kane, Phys. Rev. Lett. **102** (21), 216403 (2009).

23. D. Hsieh, Y. Xia, D. Qian, L. Wray, J. H. Dil, F. Meier, J. Osterwalder, L. Patthey, J. G. Checkelsky, N. P. Ong, A. V. Fedorov, H. Lin, A. Bansil, D. Grauer, Y. S. Hor, R. J. Cava and M. Z. Hasan, Nature **460** (7259), 1101-1105 (2009).

24. Y. L. Chen, J. H. Chu, J. G. Analytis, Z. K. Liu, K. Igarashi, H. H. Kuo, X. L. Qi, S. K. Mo, R. G. Moore, D. H. Lu, M. Hashimoto, T. Sasagawa, S. C. Zhang, I. R. Fisher, Z. Hussain and Z. X. Shen, Science **329** (5992), 659-662 (2010).

25. Z. Alpichshev, J. G. Analytis, J. H. Chu, I. R. Fisher, Y. L. Chen, Z. X. Shen, A. Fang and A. Kapitulnik, Phys. Rev. Lett. **104** (1), 016401 (2010).

26. X. C. Zhang, A. Pfeuffer-Jeschke, K. Ortner, V. Hock, H. Buhmann, C. R. Becker and G. Landwehr, Phys. Rev. B **63** (24), 245305 (2001).
27. Q. F. Sun, Y. X. Li, W. Long and J. A. Wang, Phys. Rev. B **83** (11), 115315 (2011).
28. G. M. Minkov, A. V. Germanenko, O. E. Rut, A. A. Sherstobitov, S. A. Dvoretski and N. N. Mikhailov, Phys. Rev. B **88** (4), 045323 (2013).
29. Z. Yang, Z. Yu, Y. Lansari, S. Hwang, J. W. Cook and J. F. Schetzina, Phys. Rev. B **49** (12), 8096-8108 (1994).
30. F. Gouider, M. Bugar, J. Konemann, Y. B. Vasilyev, C. Brune, H. Buhmann and G. Nachtwei, J Phys. Conf. Ser. **193** (1), 012066 (2009).
31. E. Hall, Am. J Mathema. **2**, 287-292 (1879).
32. K. von Klitzing, G. Dorda and M. Pepper, Phys. Rev. Lett **45** (6), 494-497 (1980).
33. R. B. Laughlin, Phys. Rev. B **23** (10), 5632-5633 (1981).
34. D. J. Thouless, M. Kohmoto, M. P. Nightingale and M. Dennijs, Phys Rev Lett **49** (6), 405-408 (1982).
35. R. B. Laughlin, Phys Rev Lett **50** (18), 1395-1398 (1983).
36. D. C. Tsui, H. L. Stormer and A. C. Gossard, Phys. Rev. Lett. **48** (22), 1559-1562 (1982).
37. M. I. Dyakonov and V. I. Perel, ZhETF Pis. Red. **13** (11), 657-660 (1971).
38. E. G. Mishchenko, A. V. Shytov and B. I. Halperin, Phys. Rev. Lett. **93** (22), 226602 (2004).
39. R. Raimondi and P. Schwab, Phys. Rev. B **71** (3), 033311 (2005).
40. B. A. Bernevig and S. C. Zhang, Phys. Rev. Lett. **95** (1), 016801 (2005).

41. S. Murakami, N. Nagaosa and S. C. Zhang, Science **301** (5638), 1348-1351 (2003).

42. S. Murakami, N. Nagaosa and S. C. Zhang, Phys. Rev. Lett. **93** (15), 156804 (2004).

43. Y. K. Kato, R. C. Myers, A. C. Gossard and D. D. Awschalom, Science **306** (5703), 1910-1913 (2004).

44. J. Wunderlich, B. Kaestner, J. Sinova and T. Jungwirth, Phys. Rev. Lett. **94** (4), 047204 (2005).

45. J. Sinova, D. Culcer, Q. Niu, N. A. Sinitsyn, T. Jungwirth and A. H. MacDonald, Phys. Rev. Lett. **92** (12), 126603 (2004).

46. X. L. Qi, Y. S. Wu and S. C. Zhang, Phys. Rev. B **74** (4), 045125 (2006).

47. B. A. Bernevig and S. C. Zhang, Phys. Rev. Lett. **96** (10), 106802 (2006).

48. N. A. Sinitsyn, J. E. Hill, H. Min, J. Sinova and A. H. MacDonald, Phys. Rev. Lett. **97** (10), 106804 (2006).

49. D. A. Abanin and D. A. Pesin, Phys. Rev. Lett. **109** (6), 066802 (2012).

50. M. Onoda and N. Nagaosa, Phys. Rev. Lett. **95** (10), 106601 (2005).

51. L. Fu and C. L. Kane, Phys. Rev. B **76** (4), 045302 (2007).

52. R. Roy, Phys. Rev. B **79** (19), 195322 (2009).

53. H. J. Zhang, C. X. Liu, X. L. Qi, X. Dai, Z. Fang and S. C. Zhang, Nat. Phys. **5** (6), 438-442 (2009).

54. D. Hsieh, D. Qian, L. Wray, Y. Xia, Y. S. Hor, R. J. Cava and M. Z. Hasan, Nature **452** (7190), 970-975 (2008).

55. P. Roushan, J. Seo, C. V. Parker, Y. S. Hor, D. Hsieh, D. Qian, A. Richardella, M. Z. Hasan, R. J. Cava and A. Yazdani, Nature **460** (7259), 1106-U1164 (2009).

56. A. A. Burkov and D. G. Hawthorn, Phys. Rev. Lett. **105** (6), 066802 (2010).

57. P. Cheng, C. Song, T. Zhang, Y. Zhang, Y. Wang, J.-F. Jia, J. Wang, Y. Wang, B.-F. Zhu, X. Chen, X. Ma, K. He, L. Wang, X. Dai, Z. Fang, X. Xie, X.-L. Qi, C.-X. Liu, S.-C. Zhang and Q.-K. Xue, Phys. Rev. Lett. **105** (7), 076801 (2010).

58. H. L. Peng, K. J. Lai, D. S. Kong, S. Meister, Y. L. Chen, X. L. Qi, S. C. Zhang, Z. X. Shen and Y. Cui, Nat. Mater. **9** (3), 225-229 (2010).

59. Y. Zhang, K. He, C. Z. Chang, C. L. Song, L. L. Wang, X. Chen, J. F. Jia, Z. Fang, X. Dai, W. Y. Shan, S. Q. Shen, Q. Niu, X. L. Qi, S. C. Zhang, X. C. Ma and Q. K. Xue, Nat. Phys. **6** (8), 584-588 (2010).

60. J. G. Checkelsky, Y. S. Hor, R. J. Cava and N. P. Ong, Phys. Rev. Lett. **106** (19), 196801 (2011).

61. L. A. Wray, S. Y. Xu, Y. Q. Xia, D. Hsieh, A. V. Fedorov, Y. S. Hor, R. J. Cava, A. Bansil, H. Lin and M. Z. Hasan, Nat. Phys. **7** (1), 32-37 (2011).

62. Y. L. Chen, J. G. Analytis, J. H. Chu, Z. K. Liu, S. K. Mo, X. L. Qi, H. J. Zhang, D. H. Lu, X. Dai, Z. Fang, S. C. Zhang, I. R. Fisher, Z. Hussain and Z. X. Shen, Science **325** (5937), 178-181 (2009).

63. D. Hsieh, Y. Xia, L. Wray, D. Qian, A. Pal, J. H. Dil, J. Osterwalder, F. Meier, G. Bihlmayer, C. L. Kane, Y. S. Hor, R. J. Cava and M. Z. Hasan, Science **323** (5916), 919-922 (2009).

64. X. H. Yao, M. Tokman and A. Belyanin, Phys. Rev. Lett. **112** (5), 055501 (2014).

65. R. Yoshimi, A. Tsukazaki, K. Kikutake, J. G. Checkelsky, K. S. Takahashi, M. Kawasaki and Y. Tokura, Nat. Mater. **13** (3), 254-258 (2014).

66. D. Hsieh, J. W. McIver, D. H. Torchinsky, D. R. Gardner, Y. S. Lee and N. Gedik, Phys. Rev. Lett. **106** (5), 057401 (2011).

67. J. Seo, P. Roushan, H. Beidenkopf, Y. S. Hor, R. J. Cava and A. Yazdani, Nature **466** (7304), 343-346 (2010).

68. J. Wang, B. F. Zhu and R. B. Liu, Phys. Rev. Lett. **104** (25), 256601 (2010).

69. A. P. Schnyder, S. Ryu, A. Furusaki and A. W. W. Ludwig, Phys. Rev. B **78** (19), 195125 (2008).

70. X. L. Qi, T. L. Hughes and S. C. Zhang, Phys. Rev. B **81** (15), 159901 (2010).

71. A. H. Castro Neto, F. Guinea, N. M. R. Peres, K. S. Novoselov and A. K. Geim, Rev. Mod. Phys. **81** (1), 109-162 (2009).

72. M. Schultz, F. Heinrichs, U. Merkt, T. Colin, T. Skauli and S. Lovold, Semicond. Sci. Tech. **11** (8), 1168-1172 (1996).

73. G. Bastard, Phys. Rev. B **25** (12), 7584-7597 (1982).

74. N. A. Cade, J Phys. C Solid State **18** (26), 5135-5141 (1985).

75. Y. S. Gui, C. R. Becker, N. Dai, J. Liu, Z. J. Qiu, E. G. Novik, M. Schafer, X. Z. Shu, J. H. Chu, H. Buhmann and L. W. Molenkamp, Phys. Rev. B **70** (11), 115328 (2004).

76. M. Schultz, U. Merkt, A. Sonntag, U. Rossler, R. Winkler, T. Colin, P. Helgesen, T. Skauli and S. Lovold, Phys. Rev. B **57** (23), 14772-14775 (1998).

77. O. E. Raichev, Phys. Rev. B **85** (4), 045310 (2012).

78. D. G. Rothe, R. W. Reinthaler, C. X. Liu, L. W. Molenkamp, S. C. Zhang and E. M. Hankiewicz, New J Phys. **12** (6), 065012 (2010).

79. B. Zhou, H. Z. Lu, R. L. Chu, S. Q. Shen and Q. Niu, Phys. Rev. Lett. **101** (24), 246807 (2008).

80. J. Linder, T. Yokoyama and A. Sudbo, Phys. Rev. B **80** (20), 205401 (2009).

81. H. Z. Lu, W. Y. Shan, W. Yao, Q. Niu and S. Q. Shen, Phys. Rev. B **81** (11), 115407 (2010).

82. T. L. Hughes, E. Prodan and B. A. Bernevig, Phys. Rev. B **83** (24), 245132 (2011).

83. F. Zhang, C. L. Kane and E. J. Mele, Phys. Rev. B **86** (8), 081303 (2012).

84. F. Zhang, C. L. Kane and E. J. Mele, Phys. Rev. Lett. **110** (4), 046404 (2013).

85. R. Yu, X. L. Qi, A. Bernevig, Z. Fang and X. Dai, Phys. Rev. B **84** (7), 075119 (2011).

86. X. L. Qi and S. C. Zhang, Phys Today **63** (1), 33-38 (2010).

87. Y. S. Gui, J. Liu, V. Daumer, C. R. Becker, H. Buhmann and L. W. Molenkamp, Physica E **12** (1-4), 416-419 (2002).

88. V. Daumer, I. Golombek, M. Gbordzoe, E. G. Novik, V. Hock, C. R. Becker, H. Buhmann and L. W. Molenkamp, Appl. Phys. Lett. **83** (7), 1376-1378 (2003).

89. C. R. Becker, K. Ortner, X. C. Zhang, A. Pfeuffer-Jeschke, V. Latussek, Y. S. Gui, V. Daumer, H. Buhmann, G. Landwehr and L. W. Molenkamp, Physica E **20** (3-4), 436-443 (2004).

90. J. Hinz, H. Buhmann, M. Schafer, V. Hock, C. R. Becker and L. W. Molenkamp, Semicond. Sci. Tech. **21** (4), 501-506 (2006).

91. M. Konig, H. Buhmann, C. R. Becker and L. W. Molenkamp, phys. stat. sol (c) **4** (9), 3374-3381 (2007).

92. C. Brune, A. Roth, E. G. Novik, M. Konig, H. Buhmann, E. M. Hankiewicz, W. Hanke, J. Sinova and L. W. Molenkamp, Nat. Phys. **6** (6), 448-454 (2010).

93. A. Roth, C. Brune, H. Buhmann, L. W. Molenkamp, J. Maciejko, X. L. Qi and S. C. Zhang, Science **325** (5938), 294-297 (2009).

94. B. Buttner, C. X. Liu, G. Tkachov, E. G. Novik, C. Brune, H. Buhmann, E. M. Hankiewicz, P. Recher, B. Trauzettel, S. C. Zhang and L. W. Molenkamp, Nat. Phys. **7** (5), 418-422 (2011).

95. L. L. Wang and D. D. Johnson, Phys. Rev. B **83** (24), 241309 (2011).

96. C. Brune, C. X. Liu, E. G. Novik, E. M. Hankiewicz, H. Buhmann, Y. L. Chen, X. L. Qi, Z. X. Shen, S. C. Zhang and L. W. Molenkamp, Phys. Rev. Lett. **106** (12), 126803 (2011).

97. H. Beidenkopf, P. Roushan, J. Seo, L. Gorman, I. Drozdov, Y. S. Hor, R. J. Cava and A. Yazdani, Nat. Phys. **7** (12), 939-943 (2011).

98. K. Saha, S. Das, K. Sengupta and D. Sen, Phys Rev B **84** (16), 165439 (2011).

99. T. Hanaguri, K. Igarashi, M. Kawamura, H. Takagi and T. Sasagawa, Phys. Rev. B **82** (8), 081305 (2010).

100. S. Kim, M. Ye, K. Kuroda, Y. Yamada, E. E. Krasovskii, E. V. Chulkov, K. Miyamoto, M. Nakatake, T. Okuda, Y. Ueda, K. Shimada, H. Namatame, M. Taniguchi and A. Kimura, Phys. Rev. Lett. **107** (5), 056803 (2011).

101. R. V. Aguilar, A. V. Stier, W. Liu, L. S. Bilbro, D. K. George, N. Bansal, L. Wu, J. Cerne, A. G. Markelz, S. Oh and N. P. Armitage, Phys. Rev. Lett. **108** (8), 087403 (2012).

102. D. Hsieh, F. Mahmood, J. W. McIver, D. R. Gardner, Y. S. Lee and N. Gedik, Phys. Rev. Lett. **107** (7), 077401 (2011).

103. J. Qi, X. Chen, W. Yu, P. Cadden-Zimansky, D. Smirnov, N. H. Tolk, I. Miotkowski, H. Cao, Y. P. Chen, Y. Wu, S. Qiao and Z. Jiang, Appl. Phys. Lett. **97** (18), 3513826 (2010).

104. A. D. LaForge, A. Frenzel, B. C. Pursley, T. Lin, X. F. Liu, J. Shi and D. N. Basov, Phys. Rev. B **81** (12), 125120 (2010).

105. G. S. Jenkins, A. B. Sushkov, D. C. Schmadel, N. P. Butch, P. Syers, J. Paglione and H. D. Drew, Phys. Rev. B **82** (12), 125120 (2010).

106. N. Kumar, B. A. Ruzicka, N. P. Butch, P. Syers, K. Kirshenbaum, J. Paglione and H. Zhao, Phys. Rev. B **83** (23), 235306 (2011).

107. M. C. Chang and M. F. Yang, Phys. Rev. B **80** (11), 113304 (2009).

108. P. Di Pietro, F. M. Vitucci, D. Nicoletti, L. Baldassarre, P. Calvani, R. Cava, Y. S. Hor, U. Schade and S. Lupi, Phys. Rev. B **86** (4), 045439 (2012).

109. A. B. Sushkov, G. S. Jenkins, D. C. Schmadel, N. P. Butch, J. Paglione and H. D. Drew, Phys. Rev. B **82** (12), 125110 (2010).

110. W. K. Tse and A. H. MacDonald, Phys. Rev. B **82** (16), 161104 (2010).

111. W. K. Tse and A. H. MacDonald, Phys. Rev. B **84** (20), 205327 (2011).

112. X. A. Zhang, J. Wang and S. C. Zhang, Phys. Rev. B **82** (24), 245107 (2010).

113. A. M. Shuvaev, G. V. Astakhov, G. Tkachov, C. Brune, H. Buhmann, L. W. Molenkamp and A. Pimenov, Phys. Rev. B **87** (12), 121104 (2013).

114. L. Wu, M. Brahlek, R. V. Aguilar, A. V. Stier, C. M. Morris, Y. Lubashevsky, L. S. Bilbro, N. Bansal, S. Oh and N. P. Armitage, Nat. Phys. **9** (7), 410-414 (2013).

115. S. S. Hong, J. J. Cha, D. S. Kong and Y. Cui, Nat. Commun. **3**, 757 (2012).

116. N. P. Butch, K. Kirshenbaum, P. Syers, A. B. Sushkov, G. S. Jenkins, H. D. Drew and J. Paglione, Phys. Rev. B **81** (24), 241301 (2010).

117. D. S. Kong and Y. Cui, Nat. Chem. **3** (11), 845-849 (2011).

118. J. E. Moore, Nature **464** (7286), 194-198 (2010).

119. Y. Q. Li, K. H. Wu, J. R. Shi and X. C. Xie, Front. Phys-Beijing **7** (2), 165-174 (2012).

120. J. Chen, H. J. Qin, F. Yang, J. Liu, T. Guan, F. M. Qu, G. H. Zhang, J. R. Shi, X. C. Xie, C. L. Yang, K. H. Wu, Y. Q. Li and L. Lu, Phys. Rev. Lett. **105** (17), 176602 (2010).

121. D. Kim, S. Cho, N. P. Butch, P. Syers, K. Kirshenbaum, S. Adam, J. Paglione and M. S. Fuhrer, Nat. Phys. **8** (6), 459-463 (2012).

122. Y. S. Hor, A. Richardella, P. Roushan, Y. Xia, J. G. Checkelsky, A. Yazdani, M. Z. Hasan, N. P. Ong and R. J. Cava, Phys. Rev. B **79** (19), 195208 (2009).

123. S. Y. Hwang, R. Lopez, M. Lee and D. Sanchez, Phys. Rev. B **90** (11), 115301 (2014).

124. Q. Z. Li, E. Rossi and S. Das Sarma, Phys. Rev. B **86** (23), 235443 (2012).

125. R. W. Reinthaler and E. M. Hankiewicz, Phys. Rev. B **85** (16), 165450 (2012).

126. Y. Tserkovnyak and D. Loss, Phys. Rev. Lett. **108** (18), 187201 (2012).

127. F. Rittweger, N. F. Hinsche, P. Zahn and I. Mertig, Phys. Rev. B **89** (3), 035439 (2014).

128. D. Culcer, E. H. Hwang, T. D. Stanescu and S. Das Sarma, Phys. Rev. B **82** (15), 155457 (2010).

129. R. Takahashi and S. Murakami, Phys. Rev. B **81** (16), 161302 (2010).

130. D. Culcer, Phys. Rev. B **84** (23), 235411 (2011).

131. A. Karch, Phys. Rev. B **83** (24), 245432 (2011).

132. J. Wang, A. M. DaSilva, C. Z. Chang, K. He, J. K. Jain, N. Samarth, X. C. Ma, Q. K. Xue and M. H. W. Chan, Phys. Rev. B **83** (24), 245438 (2011).

133. H. T. He, G. Wang, T. Zhang, I. K. Sou, G. K. L. Wong, J. N. Wang, H. Z. Lu, S. Q. Shen and F. C. Zhang, Phys. Rev. Lett. **106** (16), 166805 (2011).

134. Y. S. Kim, M. Brahlek, N. Bansal, E. Edrey, G. A. Kapilevich, K. Iida, M. Tanimura, Y. Horibe, S. W. Cheong and S. Oh, Phys. Rev. B **84** (7), 073109 (2011).

135. J. Chen, X. Y. He, K. H. Wu, Z. Q. Ji, L. Lu, J. R. Shi, J. H. Smet and Y. Q. Li, Phys. Rev. B **83** (24), 241304 (2011).

136. H. Steinberg, D. R. Gardner, Y. S. Lee and P. Jarillo-Herrero, Nano. Lett. **10** (12), 5032-5036 (2010).

137. N. Bansal, Y. S. Kim, M. Brahlek, E. Edrey and S. Oh, Phys. Rev. Lett. **109** (11), 116804 (2012).

138. H. Steinberg, J. B. Laloe, V. Fatemi, J. S. Moodera and P. Jarillo-Herrero, Phys. Rev. B **84** (23), 233101 (2011).

139. D. X. Qu, Y. S. Hor, J. Xiong, R. J. Cava and N. P. Ong, Science **329** (5993), 821-824 (2010).

140. J. Cayssol, Cr. Phys. **14** (9-10), 760-778 (2013).

141. D. Pesin and A. H. MacDonald, Nat. Mater. **11** (5), 409-416 (2012).

142. E. Rotenberg, Nat. Phys. **7** (1), 8-10 (2011).

143. J. G. Checkelsky, Y. S. Hor, M. H. Liu, D. X. Qu, R. J. Cava and N. P. Ong, Phys. Rev. Lett. **103** (24), 246601 (2009).

144. J. Linder, Y. Tanaka, T. Yokoyama, A. Sudbo and N. Nagaosa, Phys. Rev. Lett. **104** (6), 067001 (2010).

145.T. Neupert, S. Onoda and A. Furusaki, Phys. Rev. Lett. **105** (20), 206404 (2010).

146.Y. Tanaka, T. Yokoyama and N. Nagaosa, Phys. Rev. Lett. **103** (10), 107002 (2009).

147.A. R. Akhmerov, J. Nilsson and C. W. J. Beenakker, Phys. Rev. Lett. **102** (21), 216404 (2009).

148.G. D. Mahan, *Many-Particle Physics*, Third ed. (Kluwer Academic).

149.H. Bruus and K. Flensberg, *Many-body quantum theory in condensed matter physics: An Introduction*. (Oxford Unversity, 2004).

150.X. Leyronas, *Screening and the Random Phase Approximation*. (2012).

151.F. Stern, Phys. Rev. Lett. **18** (14), 3 (1967).

152.E. H. Hwang and S. D. Sarma, Phys. Rev. B **75** (20), 6 (2007).

153.T. Ando, A. B. Fowler and F. Stern, Rev. of Mod. Phys. **54** (2), 236 (1982).

154.V. M. Silkin, A. Garcia-Lekue, J. M. Pitarke, E. V. Chulkov, E. Zaremba and P. M. Echenique, Euro. Lett. **66** (2), 5 (2004).

155.T. Nagao, T. Hildebrandt, M. Henzler and S. Hasegawa, Phys. Rev. Lett. **86** (25), 4 (2001).

156.C. C. Sung and R. H. Ritchie, Phys. Rev. A **28** (2), 674-681 (1983).

157.C. Zhang, N. Tzoar and P. M. Platzman, Phys. Rev. B **37** (13), 7326-7330 (1988).

158.A. Bret and C. Deutsch, Phys. Rev. E **47** (2), 1276-1284 (1993).

159.A. Bergara, I. Nagy and P. M. Echenique, Phys. Rev. B **55** (19), 12864-12867 (1997).

160.H. Haug and S. W. Koch, *Quantum theory of the optical and electronic properties of semiconductors*, 2nd ed. (World Scientific, 1993).

161. Y. S. Ang, C. Zhang and C. Y. Kee, Appl. Phys. Lett. **99** (5), 3615795 (2011).

162. W. Feng, A. Tawfiq, J. C. Cao and C. Zhang, Appl. Phys. Lett. **102** (5), 4790847 (2013).

163. N. Tzoar and C. Zhang, Phys. Rev. B **32** (2), 1146-1151 (1985).

164. C. Zhang, Phys. Rev. B **66** (8), 081105 (2002).

165. C. Zhang and Z. S. Ma, Phys. Rev. B **71** (12), 121307 (2005).

166. S. A. Mikhailov, Epl-Europhys Lett. **79** (2), 27002 (2007).

167. X. J. Zhu, M. S. Hybertsen, P. B. Littlewood and M. C. Nuss, Phys. Rev. B **50** (16), 11915-11923 (1994).

168. Y. S. Ang, S. Sultan, A. Tawfiq, J. C. Cao and C. Zhang, J Infrared Millim. Technol. **33** (8), 816-824 (2012).

169. S. Shareef, Y. S. Ang and C. Zhang, J Opt. Soc. Am. B **29** (3), 274-279 (2012).

170. G. Cappellini and S. Trillo, J Opt. Soc. Am. B **8** (4), 824-838 (1991).

171. A. R. Wright, X. G. Xu, J. C. Cao and C. Zhang, Appl. Phys. Lett. **95** (7), 3205115 (2009).

172. C. R. Becker, S. D. Hatch, F. Goschenhofer, V. Latussek, J. M. Dell and L. Faraone, Phys. Rev. B **75** (11), 115115 (2007).

173. P. H. Siegel, IEEE Trans. Microw. Theory Tech. **50** (2002).

174. S. H. Zhang, J.-Q. Yao, R. Zhou, W.-Q. Wen, D.-G. Xu and P. Wang, Optoelectron. Lett. **7** (6), 4 (2011).

175. X. J. Zhu, M. S. Hybertsen and P. B. Littlewood, Phys. Rev. B **50** (16), 9 (1994).

176. G. Gappellini and S. Trillo, J. Opt. Soc. Am. B **8** (4), 15 (1991).

177. E. R. Brown, K. A. Mclntosh, K. B. Nichols and D. C. L., Appl. Phys. Lett. **66** (3), 3 (1994).

178. Z. L. Wang, H. J. Lin, N. Huang, S. Q. B. and J. Wen, Opt. Express **20** (8), 9 (2012).

179. S. Dvoretsky, N. Mikhailov, Y. Sidorov, V. Shvets, S. Danilov, B. Wittman and S. Ganichev, J Electron. Mater. **39** (7), 918-923 (2010).

180. J. N. Schulman and T. C. Mcgill, Appl. Phys. Lett. **34** (10), 663-665 (1979).

181. E. R. Youngdale, C. A. Hoffman, J. R. Meyer, F. J. Bartoli, M. A. Engelhardt and H. Hochst, Semicond. Sci. Tech. **5**, S253-S256 (1990).

182. J. Maciejko, X. L. Qi and S. C. Zhang, Phys. Rev. B **82** (15), 155310 (2010).

183. Z. D. Kvon, E. B. Olshanetsky, D. A. Kozlov, N. N. Mikhailov and S. A. Dvoretskii, Jetp. Lett. **87** (9), 502-505 (2008).

184. V. Ryzhii, M. Ryzhii and T. Otsuji, J Appl. Phys. **101** (8), 2717566 (2007).

185. X. G. Xu, S. Sultan, C. Zhang and J. C. Cao, Appl. Phys. Lett. **97** (1), 3462972 (2010).

186. Y. S. Ang, S. Sultan and C. Zhang, Appl. Phys. Lett. **97** (24), 243110 (2010).

187. Y. S. Ang and C. Zhang, Appl. Phys. Lett. **98** (4), 042107 (2011).

188. Y. S. Ang and C. Zhang, J Phys. D Appl. Phys. **45** (39), 395303 (2012).

189. Y. S. Ang and C. Zhang, Key Eng. Mater. **500**, 62-65 (2012).